SPATIALLY DEPENDENT INTERACTION TENSORS DETERMINED THROUGH NOVEL METHODS OF HIGH RESOLUTION SOLID STATE NMR

Thesis submitted to the

UNIVERSITY OF PUNE

For the degree of

DOCTOR OF PHILOSOPHY

in

CHEMISTRY

by

K. DAMODARAN

Division of Physical Chemistry

National Chemical Laboratory

Pune – 411008

INDIA

June 2006

CERTIFICATE

Certified that the work incorporated in the thesis **"Spatially Dependent Interaction Tensors Determined through Novel Methods of High Resolution Solid State NMR"** submitted by **K. Damodaran** was carried out under my supervision. Such material as has been obtained from other sources has been duly acknowledged in the thesis.

May 2006

National Chemical Laboratory,

Pune – 411008

Dr. S. Ganapathy

Research Supervisor

DECLARATION

I declare that the thesis entitled **"Spatially Dependent Interaction Tensors Determined through Novel Methods of High Resolution Solid State NMR"** submitted by me for the degree of Doctor of Philosophy to the University of Pune has been carried out at Physical Chemistry Division, National Chemical Laboratory, Pune under the supervision of Dr. S. Ganapathy. The work is original and has not been submitted in part or full by me for any degree or diploma to this or any other university.

May 2006

National Chemical Laboratory,
Pune – 411008

K. Damodaran

Dedicated To My Parents

CONTENTS

Acknowledgements

It is my great pleasure to express my heartfelt gratitude to my research advisor Dr. S. Ganapathy for his invaluable guidance and teaching throughout the course of my research program. I have to sincerely thank him for the long nights and weekends that he spent helping to set up experiments and fixing instruments. He introduced me to the area of NMR and taught me the necessary skills to have a wonderful career in the field of NMR. It is mainly because of him that my career has been escalated to a height where I stand today.

I am extremely grateful to Dr. Sivaram, Director NCL for permitting me to register for Ph.D. and giving an opportunity to do my research at NCL. Equally deep thanks are due to Dr. R. V. Chaudhari, Homogeneous Catalysis Division for his financial support during my initial period at NCL.

It is a great pleasure to thank Dr. Rajamohanan and Dr. Sanjayan for their invaluable moral support and help without which I really would not have completed my Ph.D. They were always there for me whether it was a celebration or a crisis and helped me to keep my morale high.

I am extremely thankful to Babu who taught and helped me a lot to understand and use quantum chemical calculations which constitutes a considerable part of my thesis. Special thanks for his well known patience and the long nights and weekends he spent helping me in my calculations.

I am also very grateful to Prof. Jean-Paul Amoureux and Prof. Mangala Sunder for their valuable lectures and classes at NCL which helped me learn NMR and theory.

I don't want to miss this opportunity to thank our collaborators Dr. C.V. Satyanarayana and Dr. K.N. Ganesh. Many thanks to my cheerful friends and colleagues Selvaraj, Sailaja, Rupali, Raina, Rashmi, Saravanan, Raghu, Kicha, Pasu, thiagu, Deshpande, Phalgune, BalayRao (and the list goes on) who have been very helpful and supportive throughout my days at NCL and till now.

Finally I am deeply and thoroughly indebted to my family for all the freedom, understanding and moral support they have given to my choice of career and life style.

K. Damodaran

ABSTRACT

In Chapter I, a brief introduction to NMR is given that will be useful in understanding the material presented in the following chapters. Nuclear magnetic resonance (NMR) is the most versatile and ubiquitous spectroscopic technique in use today. X-ray or liquid state NMR methods cannot study many molecules of significance. In powdered solids, the nuclear spins experience various anisotropic interactions that broaden the spectra and thus not much information is obtained. For spin ½ nuclei these interactions can be averaged and sensitivity can be gained by Magic Angle Spinning (MAS) and Cross- Polarization (CP) methods. But for nuclei with spin > ½ the second order Quadrupolar interaction cannot be averaged by these methods. Hence techniques like Double Rotation (DOR) and Dynamic Angle Spinning (DAS) were developed. The inherent problems with these methods are that they either require complicated spinners or special mechanical devices to change the spinning axis. But the recent method, Multiple Quantum Magic Angle Spinning Spectroscopy (MQMAS) allows us to get line narrowing of the central transition without changing the orientation of the spinning axis. This is done by replacing the motion of the axis in space by a change in coherence state of the observed spins.

Chemical shift (CS) and the electric field gradient tensors were calculated using ab initio methods. The nine elements of the CS tensor, commonly represented as a 3 x 3 matrix, describe the magnitude of the field felt at the site of the nucleus, induced by electronic currents brought about by an applied magnetic field. Chemical shift tensors are required to describe the nuclear shielding effects in solid-state NMR, but also can be used in liquid and gas NMR. The calculations done for this thesis uses, Gauge including atomic orbitals (GIAO) method, which is based on Hartree-Fock that allows theorists to calculate chemical shift tensors of larger molecules with relative speed and accuracy. Hartree-Fock also known as the self-consistent field theory is the most widely used method for solving the Schrödinger equation for molecular systems in theoretical chemistry. It is the basis for many of the theories used to calculate NMR chemical shifts.

Chapter II deals with the determination of the isotropic ^{13}C, ^{15}N and ^{2}H chemical shielding, both experimentally and theoretically, as an aid in the complete Solid State

NMR characterization of Cyanuric Acid (CA), Melamine (MA) and the self assembled supramolecular 1:1 CA:MA complex. Supramolecular hydrogen-bonded assemblies are novel systems which exhibit fascinating molecular architectures due to a self-assembly of structurally complementing molecules, having donor and acceptor groups. Due to their inability to form single crystals and due to poor solubility, SSNMR becomes a very important tool in their characterization. The ^{13}C chemical shift tensors and the ^{2}H electric field gradient tensors for deuterated CA, MA and CA:MA complex were determined by computer simulations of the experimental spectra obtained at different spinning speeds. ^{13}C chemical shift tensors were determined by *ab initio* calculations. ^{13}C signal assignments in CA, MA and CA:MA complex were made possible by comparison of the experimental results with *ab initio* calculations.

Chapter III deals with the determination of ^{27}Al isotropic chemical shielding and electric field gradient parameters, both experimentally and theoretically, as aids in the complete solid state NMR characterization of aluminum hydroxide polymorphs. Three basic aluminum hydroxide polymorphs, namely, gibbsite, bayerite and boehmite, were studied by ^{27}Al triple quantum (3Q) MAS NMR for the identification of the nonequivalent aluminum environments in each of the polymorphs and their unequivocal assignments to the structure. The ^{27}Al isotropic chemical shifts and the electric field gradient parameters, namely, the quadrupole coupling constant ($C_Q = e^2Qq/h$) and the asymmetry parameter (η), were determined from experiments by graphical analysis of 2D 3Q-MAS spectra and computer simulations of the experimental 1D MAS spectra. These were also determined theoretically by *ab initio* calculations. Assignments of the crystallographic nonequivalent aluminum sites in gibbsite and bayerite were made possible by comparison of the experimental results with *ab initio* calculations.

Chapter IV deals with the determination of the ^{27}Al and ^{31}P NMR parameters and characterization of the structural transformations occurring in aluminophosphates, $AlPO_4$-14 and $AlPO_4$-18 upon calcination and rehydration. ^{27}Al Triple Quantum MAS experiments aid in the direct detection of number of non-equivalent aluminum environments in a given coordination (tetra, penta and hexa). Isotropic signals obtained from ^{31}P MAS and ^{27}Al 3Q-MAS could be assigned based on the correlation of the isotropic shifts with mean T-O-T angle. For calcined $AlPO_4$-14, T-O-T angle based

assignments were not very useful, since the chemical shift dispersion was not too much. Hence *ab initio* quantum chemical calculation of isotropic chemical shifts and quadrupolar couplings were performed to support the assignments. In calcined samples where only tetrahedral P and Al environments exist, $AlPO_4$-18 results clearly show a constrained geometry with minimal tetrahedral distortion for the PO_4 and AlO_4 structure building units. Rehydration response in $AlPO_4$-14 and $AlPO_4$-18 are similar, both showing multiplicity of isotropic resonances in ^{31}P and ^{27}Al 3Q-MAS spectra.

Abbreviations

3QMAS	Triple Quantum Magic Angle Spinning
ALPO	Alumino Phosphate
CA	Cyanuric Acid
CAMA	Cyanuric Acid Melamine Complex
CP	Cross Polarization
CSA	Chemical Shielding Anisotropy
CT	Central Transition
DAS	Dynamic Angle Spinning
DFT	Density Functional Theory
DOR	Double Rotation
EFG	Electric Field Gradient
GIAO	Gauge Independent Atomic Orbital
GTO	Gaussian Type Orbital
HF	Hartree Fock
Hz	Hertz
MA	Melamine
MAS	Magic Angle Spinning
MQMAS	Multiple Quantum Magic Angle Spinning
NMR	Nuclear Magnetic Resonance
PAS	Principal Axis System
ppm	Parts Per Million
QCC	Quadrupole Coupling Constant
QIS	Quadrupole Induced Shift
REDOR	Rotational Echo Double Resonance
SSNMR	Solid State Nuclear Magnetic Resonance
ST	Satellite Transition
STMAS	Satellite Transition Magic Angle Spinning
STO	Slater Type Orbital
TMS	Tetra Methyl Silane

CHAPTER I

Introduction to Solid State NMR and *ab initio* Calculation of NMR Shielding Tensors.

Introduction to Solid State NMR

Nuclear Magnetic Resonance (NMR) is a versatile and ubiquitous branch of radio frequency spectroscopy and has made great strides in Physics, Chemistry, Biology and Medicine since its discovery[1] as a cw technique in the mid-1940s and as a pulse-FT technique[2] in the mid 1970s. Today, NMR has evolved into one of the most powerful tools for structural and dynamic investigation of a wide variety of complex molecular systems. NMR is more often practiced in the liquid state and is extensively used for soluble materials. However, solid state NMR, especially applicable to insoluble and reactive materials, provides deeper insights on molecular structure and dynamics. Materials such as polymers, zeolite catalysts, oxides, supramolecular complexes and membrane proteins are examples of systems for which solid state NMR is the method of choice. In such materials, nuclear spins have a static disposition and hence the anisotropy of various spin interactions is retained, totally or partially. This is contrary to liquid state NMR measurements, which yield only the isotropic average of interaction tensors. Thus, useful structural information can be obtained from NMR measurements carried out in the solid state. More importantly, solid state NMR sores over X-ray diffraction methods in the study of disordered materials. The major objective of the research work carried out and reported in this thesis is to determine spatially dependent interaction tensors through novel methods of high resolution solid state NMR. It is therefore pertinent to provide a brief introduction to solid state NMR so that necessary framework is laid out before the research work carried out by the author is presented and discussed.

1.1 Spin Interactions in Solid State NMR.

The four main interactions of interest in diamagnetic solids are: chemical shielding, dipolar coupling (homonuclear and heteronuclear), indirect spin-spin coupling and quadrupolar interactions. Of these, the chemical shielding and quadrupolar interactions and their exploitation in experimental measurements and theoretical calculations for structural elucidation are of special interest in the present work. These interactions, which are molecule fixed, are described as tensors of rank two. They act as a perturbation on the Zeeman interaction and cause line broadening in the solid state

NMR spectra of powder samples. Although single crystal rotation studies enable the determination of the interaction tensors, it is desirable to employ powder samples. In static samples, the line broadening and spectral overlap complicate the spectral analysis and the determination of anisotropic parameters. Modern solid state NMR spectroscopy is devoted towards retrieving these tensors through experimental strategies which are performed in the high-resolution regime. The spin interactions are cleverly manipulated in experimental schemes under coordinate space and spin space averaging[3] allowing the anisotropic parameters to be determined under high resolution conditions. Besides, advances in computational methods allow the interaction tensors to be determined by theoretical means with acceptable levels of numerical accuracy.

In the presence of the various spin interactions, which perturb the Zeeman interaction H_z, the total Hamiltonian is written as,

$$\mathcal{H}_{total} = \mathcal{H}_Z + \mathcal{H}_{CS} + \mathcal{H}_D + \mathcal{H}_J + \mathcal{H}_Q$$

the perturbing Hamiltonians being ascribed to the relevant spin interaction as denoted above. Each of these interactions is described by a tensor of rank two and the anisotropic manifestation of the spin interactions is therefore embedded in this description. A tensor is a generalized array that describes the relationship between vector quantities[4] and it has certain well-defined properties in relation to the rotation of the axis system used to define it. For example, when an electric field (a vector) is applied to a molecule, an electric dipole moment (a vector) is induced. These two quantities are linked by the molecular polarizability tensor.

Consider a set of linear functions *f* that take in 0, 1 and 2 vectors, respectively, in an orthonormal Cartesian basis in a three dimensional space. By virtue of the linearity of *f*, it can be written in the form,

$$f() = A, \qquad [1]$$

$$f(v) = \begin{bmatrix} A_1 & A_2 & A_3 \end{bmatrix} \begin{bmatrix} v_1 \\ v_2 \\ v_3 \end{bmatrix} \quad [2]$$

$$f(u,v) = \begin{bmatrix} u_1 & u_2 & u_3 \end{bmatrix} \begin{bmatrix} A_{11} & A_{12} & A_{13} \\ A_{21} & A_{22} & A_{23} \\ A_{31} & A_{32} & A_{33} \end{bmatrix} \begin{bmatrix} v_1 \\ v_2 \\ v_3 \end{bmatrix} \quad [3]$$

The square array A in equation [3] denotes the tensor in the matrix representation. Since tensors are normally defined in Cartesian basis, they are called Cartesian tensors[5]. Since the rank of a tensor is equal to the number of input vectors in the corresponding linear function, the Cartesian tensor, which has nine elements (3^2), has rank 2. The spin interactions are described as second rank tensors. In the molecular frame, called the Principal Axis System (PAS), the tensor is diagonal since it can not be reduced any further. It can be transformed from one coordinate system to another using Euler transformations[6]

1.1.1 Zeeman Interaction

The Zeeman interaction, by far the dominant one, describes the interaction of a nuclear spin I with an externally applied static magnetic field B_0. In terms of Cartesian basis tensors, with B_o applied along the z-axis in the laboratory frame,

$$H_z = \begin{bmatrix} I_x & I_y & I_z \end{bmatrix} \begin{bmatrix} 1 & 0 & 0 \\ 0 & 1 & 0 \\ 0 & 0 & 1 \end{bmatrix} \begin{bmatrix} 0 \\ 0 \\ -\gamma B_0 \end{bmatrix} \quad [4]$$

$$= \gamma B_0 I_z$$

$$= \omega_0 I_z$$

Here, ω_0 is the Larmor frequency in units of rad/sec ($\omega_0 = 2\pi\nu_0$). Since Zeeman interaction is normally the largest interaction, other interactions are treated as perturbations to the Zeeman interaction.

1.1.2 Chemical Shielding Interaction

Chemical Shielding interaction of a nuclear spin with the local field generated by the interplay of the external magnetic field (B_0) and the electron cloud surrounding the nucleus. The electron cloud precesses about the external magnetic field. Thus, additional magnetic fields are induced. The induced field normally opposes the external magnetic field for diamagnetic materials, so the nucleus experiences the superposition of the external magnetic field and the induced internal fields. The nuclear resonance frequency is thus shifted from the external magnetic field value. Usually the chemical shift, relative to a reference substance, is expressed in ppm (parts per million) of the Larmor frequency. Because the electronic environment is usually different for different directions in the molecule, the nucleus experiences a different shielding, and hence has a different chemical shift, in different directions. The local magnetic field can be given by B_{local},

$$B_{local} = B_0 - B_0\sigma = B_0 (1 - \sigma) \qquad [5]$$

The chemical shielding is a second rank tensor and can be expressed in terms of Cartesian basis as,

$$f(u,v) = \begin{bmatrix} I_x & I_y & I_z \end{bmatrix} \begin{bmatrix} \sigma_{xx} & \sigma_{xy} & \sigma_{xz} \\ \sigma_{yx} & \sigma_{yy} & \sigma_{yz} \\ \sigma_{zx} & \sigma_{zy} & \sigma_{zz} \end{bmatrix} \begin{bmatrix} 0 \\ 0 \\ -\gamma B_0 \end{bmatrix} \qquad [6]$$

$$= \omega_0 \sigma_{zz} I_z$$

The chemical shielding tensor in the Principal Axis System (PAS) is

$$\boldsymbol{\sigma}_{(PAS)} = \begin{bmatrix} \sigma_{11} & 0 & 0 \\ 0 & \sigma_{22} & 0 \\ 0 & 0 & \sigma_{33} \end{bmatrix} \quad [7]$$

In general, $\mathrm{Tr}[\boldsymbol{\sigma}] \neq 0$ and $\boldsymbol{\sigma}$ is not necessarily symmetric. Since antisymmetric components of $\boldsymbol{\sigma}$ cause resonance shift only to second order[7] $\boldsymbol{\sigma}$ is taken to be symmetric.

It is convenient to describe the chemical shielding tensor in terms of three different parameters, which are essentially derived from the three principal elements, namely, σ_{11}, σ_{22} and σ_{33}. These are:

(1) Isotropic Chemical shift (σ_{iso}):

This is the average value of the tensor and denotes the orientationally independent quantity and is given by

$$\sigma_{iso} = 1/3\ \mathrm{Tr}\,(\boldsymbol{\sigma}) = (\sigma_{11} + \sigma_{22} + \sigma_{33}) / 3 \quad [8]$$

(2) Chemical Shift Anisotropy ($\Delta\sigma$):

Chemical Shift Anisotropy (CSA) is the difference between σ_{33} and the average of σ_{11} and σ_{22} and essentially denotes how strong the anisotropy of the chemical shielding interaction is. $\Delta\sigma$ can be positive, negative or zero.

$$\Delta\sigma = \sigma 33 - \frac{\sigma_{11} + \sigma_{22}}{2} \quad [9]$$

$$= \frac{3}{2}(\sigma_{33} - \sigma_{iso})$$

(3) Asymmetry Parameter (η):

The asymmetry parameter is a measure of the deviation from axial or cylindrical symmetry. It is defined as,

$$\eta = \frac{\sigma_{11} - \sigma_{22}}{\sigma_{33} - \sigma_{iso}} \quad [10]$$

where $0 \leq \eta \leq 1$. If $\eta = 0$, then $\sigma_{11} = \sigma_{22}$ meaning that the chemical shift tensor is axially symmetric about σ_{33}. Often , η provides a visualization of the symmetry of the local

electronic environment due to bonding arrangement and serves as a structural aid along with σ_{iso} and $\Delta\sigma$. Finally, it may be noted that we have used the representation σ, as against δ by which chemical shifts are usually referred in liquid state NMR. The σ scale is appropriate in the solid state context, since positive values of σ, with respect to a reference compound, denote shielding and negative values denote deshielding.

1.1.3 Dipole – Dipole Interaction

This is the through-space interaction between the magnetic moments of nuclear spins with non-zero spin quantum numbers. The magnitude of the dipolar interaction depends on two factors, (1) Distance between the spins; it is proportional to the inverse cube of the distance (r) between the two coupling partners (i,j). (2) Orientation (β) of the vector connecting the two spins with respect to the magnetic field.

$$\text{Dipolar Coupling} \quad \alpha \quad (3\text{Cos}^2(\beta) - 1) / r_{ij}^3 \qquad [11]$$

The Hamiltonian for the dipolar coupling between two nuclei is given by,

$$\boldsymbol{H}_D = \begin{bmatrix} I_x & I_y & I_z \end{bmatrix} \begin{bmatrix} D_{xx} & D_{xy} & D_{xz} \\ D_{yx} & D_{yy} & D_{yz} \\ D_{zx} & D_{zy} & D_{zz} \end{bmatrix} \begin{bmatrix} S_x \\ S_y \\ S_z \end{bmatrix} \qquad [12]$$

$$= \quad 2\pi D_{zz}^{LAB} \frac{3I_z S_z - I.S}{\sqrt{6}}$$

The dipolar coupling D is an axially symmetric second rank traceless tensor. In the PAS, it can be represented as,

$$\mathbf{D}^{\text{PAS}} = d \begin{bmatrix} -\frac{1}{2} & 0 & 0 \\ 0 & -\frac{1}{2} & 0 \\ 0 & 0 & 1 \end{bmatrix} \qquad [13]$$

Where *d* is the dipolar coupling constant given by,

$$d = -\frac{\mu_0}{4\pi}\frac{\hbar\gamma_I\gamma_S}{r_{i,j}^3} \qquad [14]$$

μ_0 is the permeability constant, γ_I and γ_S are the gyromagnetic ratio of spins I and S respectively.

1.1.4 J-coupling Interaction

The interaction which couples two interacting spins via bonding electrons is the spin-spin coupling or the J coupling interaction. The Hamiltonian for the J coupling interaction is given by,

$$\boldsymbol{H}_J = \begin{bmatrix} I_x & I_y & I_z \end{bmatrix} \begin{bmatrix} J_{xx} & J_{xy} & J_{xz} \\ J_{yx} & J_{yy} & J_{yz} \\ J_{zx} & J_{zy} & J_{zz} \end{bmatrix} \begin{bmatrix} S_x \\ S_y \\ S_z \end{bmatrix} \qquad [15]$$

$$= 2\pi J_{zz}^{LAB} \frac{3I_zS_z - I.S}{\sqrt{6}}$$

In the PAS the J tensor is,

$$\mathbf{J}_{PAS} = J_{iso} + \Delta J \begin{bmatrix} -½ & 0 & 0 \\ 0 & -½ & 0 \\ 0 & 0 & 1 \end{bmatrix} \qquad [16]$$

Similar to chemical shift, the J tensor is also described by the parameters J_{iso} and ΔJ, given by,

$$J_{iso} = (J_{11} + J_{22} + J_{33}) / 3 \qquad [17]$$

$$\Delta J = \frac{3}{2}\left(J_{33} - J_{iso}\right)$$

It is recognized that both dipolar and J coupling interactions are bilinear in spin variables and have the same orientation dependence, thus making them inseparable from each other in the NMR spectra of solid samples. Usually, the dipolar interactions are strong enough that the influence of J anisotropy in the solid state NMR spectra is neglected, especially in the case of light elements.

1.1.5 Quadrupolar Interaction

Nuclei with spin quantum number greater than ½ possess electric quadrupole moment (e**Q**), where **Q** denotes the quadrupole moment tensor. This quadrupole moment interacts with the electric field gradient (EFG) from the surrounding electrons to give quadrupolar coupling. Quadrupolar interaction will be discussed in detail in section 1.3.

1.2 Manipulation of Spin Interactions

In solid state due to the lack of molecular tumbling, all the observable interactions retain their anisotropic behavior fully or partially. The latter results when restricted molecular motions are present, as often is the case in solids containing methyl groups or aromatic[7]. Due to line broadening introduced in the NMR spectrum[7, 8], the resolution is insufficient to identify distinct molecular sites. However, valuable structural and dynamic information can be discerned from the anisotropy of the interaction tensors. Particularly, the CSA and quadrupolar interactions provide insights into electronic structure and bonding, while the dipolar coupling offers provide direct access to internuclear distances. The quest is to obtain high spectral resolution by averaging the anisotropic part of the interaction tensors. The most common experimental approaches to manipulate these spin interactions to obtain line narrowing will be discussed in the following sections.

1.2.1 Magic Angle Spinning

The anisotropic line broadening in solid state NMR of polycrystalline samples arises from the orientation dependence of the interaction tensors with respect to the B_0

field. When the interaction is inhomogeneous, the broad line spectrum can be considered to be a superposition of many lines occurring at different resonance frequencies, each originating from a given nucleus in a particular crystallite. Such anisotropic broadenings with inhomogeneous character can be readily averaged in the coordinate space using the technique of Magic Angle Spinning (MAS).[9-11]

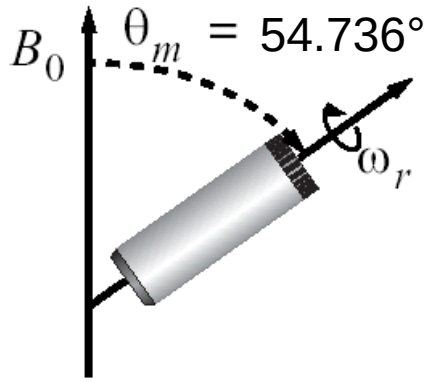

This is achieved by rapidly spinning the sample around an axis inclined at the Magic Angle, where $\theta_m = Cos^{-1}\left(1/\sqrt{3}\right)$. MAS is capable of averaging some of the anisotropic interactions to their isotropic values. A cylindrical average over one rotation of the spinner (rotor period) separates the isotropic component into the center band and the anisotropic component into the spinning side band manifold. The anisotropy ($\Delta\sigma$) and the asymmetry (η) of the relevant interaction can be retrieved from the side band intensities. In a pulsed experiment, the time domain response is to give a train of the so called 'rotational echoes', the FT of which yield the side band patterns in the frequency domain. The anisotropic part of the interaction results in the dephasing of the spins after the $\pi/2$ pulse. At the end of each rotor period all spins return to their original orientation, thus causing a refocusing to generate the rotational echoes.[12a] Herzfeld and Berger analysis[12b] of side band intensities is often used to retrieve these parameters from MAS spectra.

Since dipolar coupling is a traceless tensor and has the term ($3\cos^2\theta$ - 1), the angle dependent part in the Hamiltonian vanishes to zero with Magic Angle Spinning. Basically, only spin pairs with their dipolar vectors oriented parallel to the magic angle

will have a dipolar coupling that is zero all the time. For all other orientations the dipolar couplings change continuously due to the motion of the rotor and the dipolar interaction therefore becomes time dependent. The average value of the dipolar coupling over one rotor period is zero. However, it may be noted that in case where the dipolar interaction is homogeneous, as they tend to be in most situations, MAS at very high spinning speeds (ca. 50 – 70 kHz) is often required to accomplish line narrowing to produce acceptable spectral resolution. Alternatively, multiple-pulse line narrowing schemes[13a] or spin-locking at the 'magic angle' using FSLG/PMLG[13b] schemes can be employed independently or combined with MAS to remove homogeneous broadening. Removal of dipolar interaction by MAS, required to achieve high resolution, also leads to the loss of structural information in the form of dipolar couplings. However, ingenious methods have been developed to recouple dipolar interaction under MAS. Among these, Rotational Echo Double Resonance (REDOR)[14,15] is a robust and extensively used method which recouples hetero-nuclear dipolar coupling between spin ½ nuclei.

MAS is successful in removing first order broadening due to chemical shielding, dipolar, indirect spin-spin coupling and quadrupolar (I =1) interactions since the orientation dependence for the line broadening is governed by the P_2 (cosθ) term in the relevant spin Hamiltonian. However, in the case of half-integer quadrupolar nuclei, second-order effects become important and, as discussed in detail in section 1.3, MAS is of no avail since second-order broadening can not be removed at the 'magic angle'.

1.2.2 Heteronuclear Decoupling

Often, hetero-nuclear dipolar interaction is the major source of line broadening in many solid materials, such as organic compounds and biological solids. Removal of hetero-nuclear dipolar broadening by MAS alone is not practical since very high spinning speed is required to achieve the desired resolution and the maximum spinning speed currently achieved in many cases is 50 kHz[16]

In such cases, the dipolar broadening due to the unobserved nuclei on the observed nucleus can be removed by simply irradiating the unobserved spins at their Larmor frequency. In particular, for highly protonated solids, the protons by themselves are

strongly coupled among themselves by homo-nuclear dipolar interaction. Although, the hetero-nuclear dipolar I-S interaction (e.g., ^{13}C-^{1}H) is inhomogeneous, the strong mutual couplings among I spins (^{1}H) renders the I-S dipolar interaction to be homogeneous. In order to decouple the S spins from homo-nuclear coupled I spins, the radio frequency irradiation at the I spin Larmor frequency must be sufficiently strong that the S spins are decoupled from the proton bath. Dipolar decoupling with strong r.f fields (> 80 kHz) are often warranted in many practical applications. Efficient decoupling schemes, such as TPPM[17] and XiX[18] have been widely used. In MAS experiments, due considerations must be given to the interference between the sample rotation and the r.f irradiation since both serve to attenuate heteronuclear dipolar couplings. The effects are in fact well separated if one works on one of the two regimes, namely the very fast and the slow sample spinning. The removal of hetero-nuclear dipolar coupling is mainly due to sample spinning or due to r.f decoupling, as the case may be. However, in the intermediate regime unwanted interference effects occur under MAS if the decoupling precession frequency γB_1 is equal to the rotation frequency ω_r. But normally, decoupling field strengths of $\gamma B_1/2\pi \approx 100$ kHz are used, which is well above typical spinning speeds. Thus hetero-nuclear dipolar broadening is removed by dipolar decoupling and MAS serves to average the broadening due to anisotropic chemical shielding.

1.2.3 Spin Lock and Cross Polarization

In addition to the resolution enhancement achieved by dipolar decoupling and magic angle spinning, there is a quest to improve the detection sensitivity, especially when one deals with nuclei having low natural abundance, such as ^{13}C and ^{15}N, or low magnetogyric ratio, or both. The sensitivity enhancement is provided by the technique of Cross Polarization (CP)[19]. CP serves to enhance the signal of rare spins (^{13}C, ^{15}N) by a polarization transfer from the abundant spins (^{1}H). The polarization transfer is accomplished by a Hartmann – Hahn matching[20] of the energy levels in the rotating frame. The standard CP pulse sequence is shown in Fig. 2. First, the proton magnetization is brought into the xy plane by a $\pi/2$ pulse. R.F fields are then applied to the ^{1}H and ^{13}C spins for a period τ_{CP}, causing the magnetization to be exchanged

between the ^{1}H spins and the ^{13}C spins under the Hartmann-Hahn match. Finally, the ^{13}C spins are detected while the ^{1}H spins are decoupled. In the rotating frame, the precession rate of each spin about the spin-lock field is determined by the respective strengths of the B_1 fields and their gyromagnetic ratios. When the Hartmann-Hahn condition is satisfied, the precession frequency of both types of spins will be equal, which is expressed mathematically by the match condition,

$$\gamma_I B_{1I} = \gamma_S B_{1S} \qquad [18]$$

where γ_I and γ_S are the gyromagnetic ratios of ^{1}H and ^{13}C respectively and B_{1I} and B_{1S} are the r.f magnetic field strengths of ^{1}H and ^{13}C, respectively.

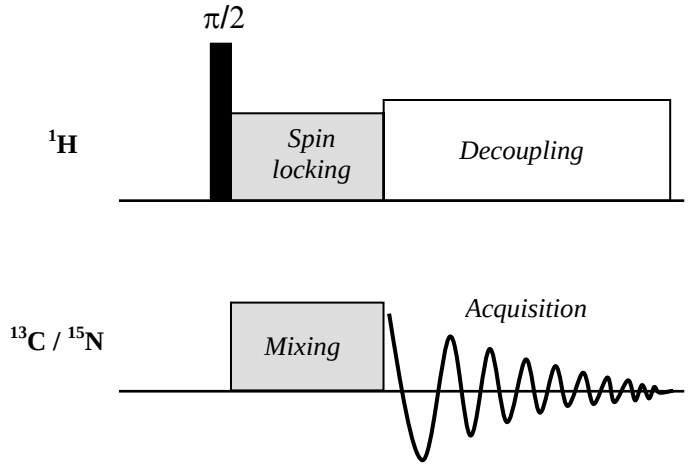

Figure – 1: Pulse sequence for hetero-nuclear cross-polarization between abundant (I) (^{1}H) and rare (S) (^{13}C , ^{15}N) spins. CP is established by the Hartmann-Hahn match during the mixing period shown and obeys the condition $\gamma_I B_{1I} = \gamma_S B_{1S}$.

The increase in the ^{13}C spin magnetization during the CP mixing period τ_{CP} depends on the strength of the ^{1}H – ^{13}C dipolar coupling, which is stronger for protonated carbons (CH, CH2, CH3) compared to non-protonated (COO) carbons. Typical mixing times range from 100 μs to a few ms. Usually, the polarization buildup must compete with the leakage effects due to rotating frame spin-lattice relaxation. The sensitivity enhancement actually achieved is dependent on the cross-polarization rate (T_{CP}^{-1}) and the relaxation rate ($T_{1\rho}^{-1}$). Quantitative estimates of signal enhancement usually require

the cross-polarization dynamics to be studied, where the time evolution of the ^{13}C signal intensity is monitored as a function of the mixing time

The sensitivity enhancement by CP is combined with resolution enhancement by dipolar decoupling and MAS to record NMR spectra of rare spins in the solid state. Indeed, CP-MAS has become one of the most powerful and routinely used techniques in solid state NMR practice. While the CP enhancement is due to the ratio of gyromagnetic ratios of 1H and 13C, the rewards in sensitivity enhancement are further brought about by the faster repetition of signal accumulation in the CP-MAS experiment compared to the Bloch decay experiment. Since the magnetization transfer in a CP experiment is from ^{1}H to ^{13}C or ^{15}N, the repetition time for the experiment is governed by the shorter ^{1}H spin-lattice relaxation time and not by the much longer rare-spin relaxation times.

1.3 NMR of Quadrupolar nuclei.

Quadrupolar interaction arises in the case of nuclei having spin number greater than ½ . The quadrupolar nuclei can themselves be classified into two different families, namely, integer spins (e.g., ^{2}H, ^{6}Li, ^{14}N) and half-integer spins (^{7}Li, ^{17}O, ^{23}Na, ^{27}Al etc) and this classification entails treating the effects of quadrupolar interaction on the Zeeman interaction in elegant and tractable ways. An inspection of the NMR periodic table shows that about two-thirds of the quadrupolar nuclei belong to the half-integer spin family. Since much of the work reported in this thesis deal with half-integer nuclei it is succinct to dwell upon the quadrupolar interaction in some detail.

1.3.1 Origin of Quadrupolar Broadening

For nuclei with spin number > ½, one formally associates a quadrupole moment (e**Q** due to the non-spherical nuclear charge distribution. The quadrupole moment is a tensor and when integrated over the volume it becomes a scalar quantity. The interaction of the quadrupole moment with the electric field gradient tensor, leads to a perturbation of the Zeeman levels and the NMR transition frequencies are altered due to this effect.. The strength of the interaction depends on the size of the nuclear quadrupole moment and the extent of departure of the field gradients from cubic symmetry.

The quadrupolar interaction is described using the Hamiltonian H_Q,

$$\boldsymbol{H_Q} = \frac{eQ}{2I(2I-1)} I \bullet V \bullet I \qquad [19]$$

$$= \frac{eQ}{2I(2I-1)} \begin{bmatrix} I_x & I_y & I_z \end{bmatrix} \begin{bmatrix} V_{xx} & V_{xy} & V_{xz} \\ V_{yx} & V_{yy} & V_{yz} \\ V_{zx} & V_{zy} & V_{zz} \end{bmatrix} \begin{bmatrix} I_x \\ I_y \\ I_z \end{bmatrix} \qquad [20]$$

where, e is the elementary charge, Q is the quadrupole moment and **V** is the electric field gradient tensor.

In the principal axis system (PAS), EFG is given by the diagonal traceless tensor,

$$\mathbf{V}_{(PAS)} = \begin{bmatrix} V_{xx} & 0 & 0 \\ 0 & V_{yy} & 0 \\ 0 & 0 & V_{zz} \end{bmatrix} \qquad [21]$$

Where $V_{xx} + V_{yy} + V_{zz} = 0$. The magnitude of the EFG tensor is defined by '*eq*' that is the largest component of the EFG tensor V_{zz}. Similar to the asymmetry parameter for chemical shielding, for EFG the asymmetry parameter (η) can be defined as,

$$\eta = \frac{V_{xx} - V_{yy}}{V_{zz}} \qquad [22]$$

η lying in the range 0 to 1, the extreme values corresponding to axially symmetric field gradient tensors.. The magnitude of the quadrupole interaction can also be given in terms of frequency units (Hertz) by the quadrupole coupling constant, C_Q, where

$$C_Q = \frac{e^2 qQ}{h} \qquad [23]$$

eQ is the nuclear quadrupole moment, $eq = V_{zz}$ and *h* is the Planck 's constant.

Figure - 2 shows the energy levels for a spin 3/2 nucleus a) without any quadrupolar interaction, b) with quadrupolar interaction to first and c) second order. To first order, the energy levels corresponding to m_I = -½ and the m_I = ½ shift by the same amount in the same direction. Thus, the resonance frequency of the $-½ \rightarrow +½$ transition, known as the central transition (CT), is unchanged by the first-order quadrupolar Hamiltonian. These change only to second-order in perturbation. In contrast, the resonance frequencies of the $-3/2 \rightarrow -½$ and $+½ \rightarrow +3/2$ transitions, known as the satellite transitions (ST), are each shifted by an amount proportional to $\omega_Q^{(1)}$, the first-order quadrupolar interaction parameter. The net result of $H_Q^{(1)}$ on a half-integer quadrupolar nucleus is to shift and broaden (in a powdered solid) the resonances that result from the satellite transitions to a large extent. Therefore, in a standard solid-state NMR experiment performed to detect the central transition, the satellite transitions are seldom observed.[21] Since the central transition is still broadened by the second order quadrupole coupling, the resulting line width can be quite large.

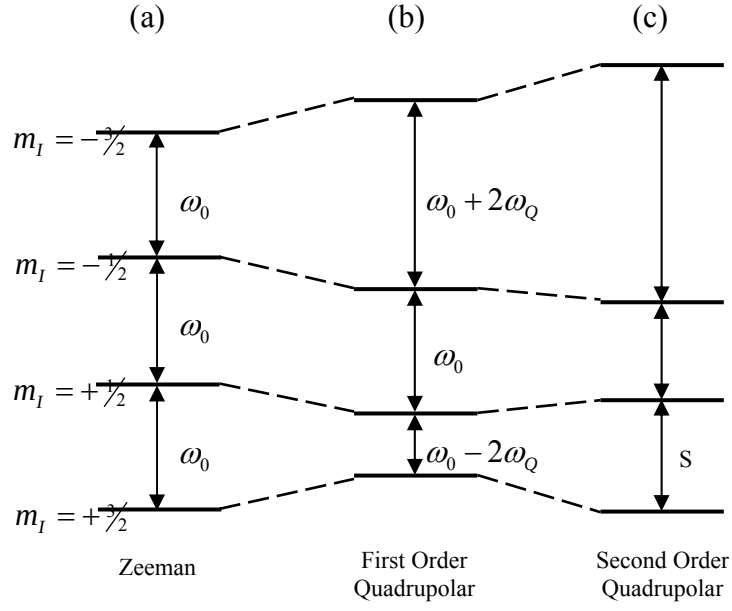

Figure – 2: Schematic energy level diagram showing the effect of (a) Zeeman (b) first- order and (c) second-order quadrupolar interactions for a spin 3/2 system.

1.3.2 Effect of MAS on n/2 quadrupolar nuclei

An important feature of the second-order quadrupole Hamiltonian $H_Q^{(2)}$ is its orientation dependence. Apart from the $P_2(\cos\theta)$ term, the second order quadrupole Hamiltonian has $P_4(\cos\theta)$ dependence. These are,

$$P_2(\cos\theta) = -\tfrac{1}{2}\left(3\cos^2\theta - 1\right)$$
$$P_4(\cos\theta) = \tfrac{1}{8}\left(3 - 30\cos^2\theta + 35\cos^4\theta\right) \qquad [24]$$

The $P_2(\cos\theta)$ goes as $\left(3\cos^2\theta - 1\right)$ and hence can be removed by MAS. The quadrupolar broadening results due to the $P_4(\cos\theta)$ term which does not vanish at the 'magic angle' but at a different angle. Figure – 3 shows the angular dependence of $P_2(\cos\theta)$ and $P_4(\cos\theta)$ functions on the spinning angle. $P_2(\cos\theta) = 0$ at the 'magic angle' of 54.736^0 and $P_4(\cos\theta) = 0$ at angles of 30.56^0 and 70.12^0.

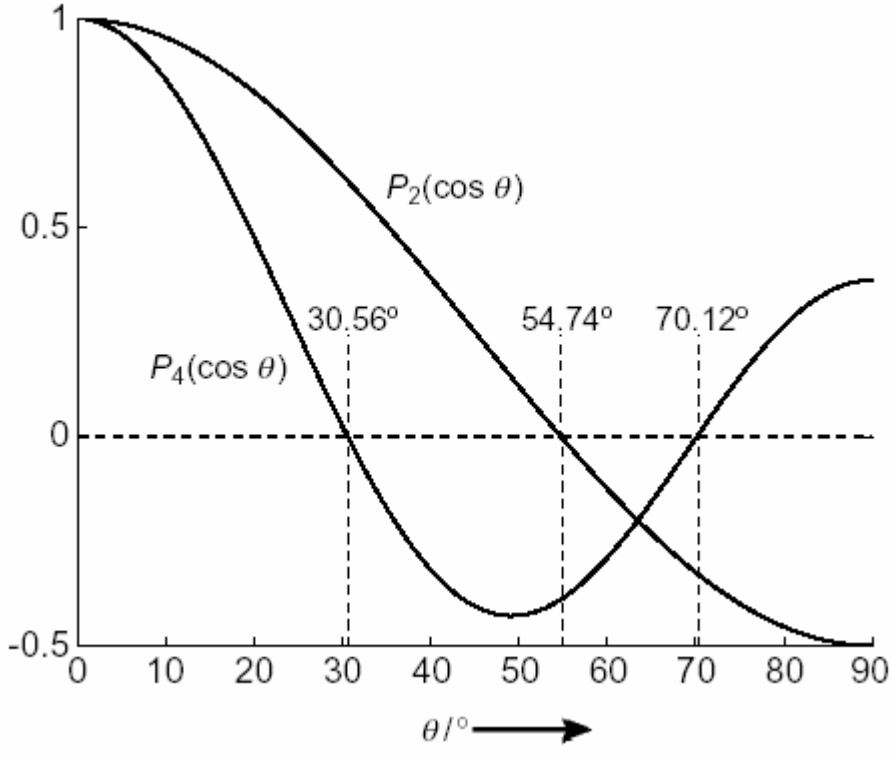

Figure – 3 : Angular dependence of $P_2(\cos\theta)$ and $P_4(\cos\theta)$.functions present in the orientation dependent terms of the second-order quadrupolar Hamiltonian H_Q^2. The nulls of the two functions correspond to the angles indicated.

The effect of MAS due to second-order effects is shown in Figure – 4 for three different values of the asymmetry parameter. The simulations were performed using the DMFIT program[22]. Although some line narrowing is achieved by MAS, the effect is not as dramatic as it is observed in the case of spin ½ nuclei. The failure of MAS to completely average the second-order quadrupolar broadening is due to the presence of the $P_4(\cos\theta)$ term. Techniques developed for addressing the second-order effects and to get high resolution spectra in half-integer nuclei are discussed in the following sections.

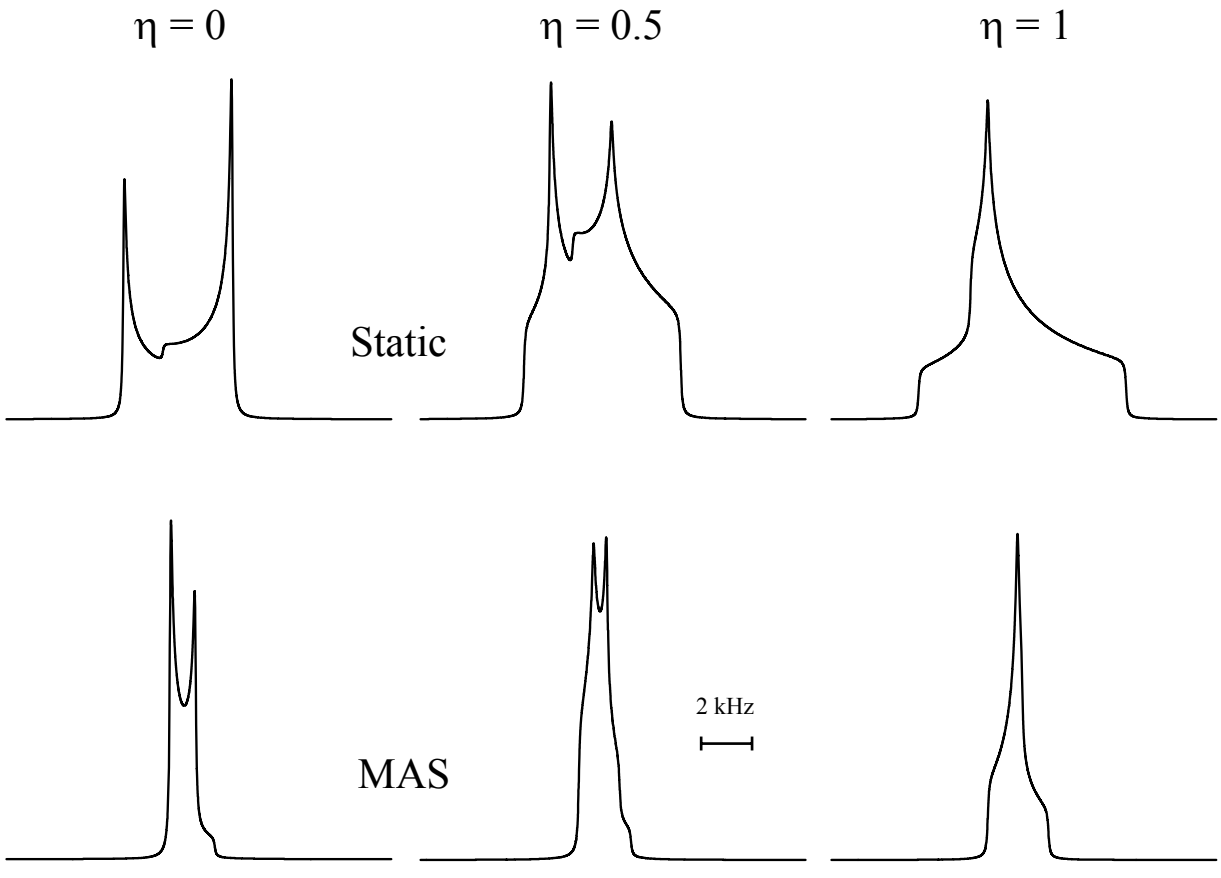

Figure – 4: Effect of MAS on the central transition line shape in the case of a spin 3/2 nucleus, simulated using DIMFIT for the indicated values of η. and using C_Q = 2 MHz.

1.3.3 Techniques to remove Second Order Quadrupolar Broadening

The line broadening in half-integer quadrupolar nuclei due to second-order quadrupole effects can not be removed at the 'magic angle'. However, the residual second-order broadening can be reduced to a great degree using the technique of Variable Angle Sample Spinning (VASS)[23] , the extent of line narrowing being dependent on the asymmetry parameter of the field gradient tensor. From VASS, it was realized that there are complementary spinning angles for which the second-order powder patterns are 'frequency reversed'. This aspect was exploited to develop the method of Dynamic Angle Spinning (DAS) by spinning the sample at these two different complementary angles.[24, 25] This 2D technique correlates the anisotropic frequencies during the evolution (t_1) and the detection (t_2) periods, corresponding to the sample rotation at the DAS angles θ_1 and θ_2, and enables a high resolution spectrum devoid of second-order quadrupolar broadening to be obtained by a skew projection or a shearing of the 2D data set. For DAS, a dedicated probehead equipped to change the axis of spinning within the pulse sequence is required. Although there are many sets of so-called DAS angle pairs, [24, 26] the angles 37.38^0 and 79.19^0 are chosen for practical reasons. DAS resulted in many applications, although it's wide spread use was limited by the technically demanding probe hardware and the unfavorable spin-lattice relaxation times in the case of quadrupolar nuclei.

As an alternative to DAS, the technique of Double Rotation or DOR[27,28] was developed. DOR, unlike DAS, which requires a sequential manipulation of the spinning angles, eliminates the second-order quadrupolar broadening by spinning the sample at the angles of 54.74^0 and 30.56^0 simultaneously to remove the $P_2(\cos\theta)$ and $P_4(\cos\theta)$ spatial terms of $H_Q^{(2)}$. This is accomplished by having a rotor inside a rotor that allows the sample to be rotated at two different axes simultaneously. Under DOR conditions, both the first order broadening (chemical shielding, dipolar) and the second-order quadrupole broadening are removed and high resolution spectra from half-integer quadrupolar nuclei are readily observed [29]. Although DOR is a simple 1D technique, special stator-rotor system is required and the spinning of the outer rotor is not fast

enough that side band interference can be removed. DOR has found numerous applications in various materials applications.

1.4 Multiple Quantum Magic Angle Spinning

MQMAS or Multiple Quantum Magic Angle Spinning[30,31] is an elegant method which removes second-order quadrupolar broadening to yield high-resolution NMR spectra by performing the experiment at the familiar 'magic angle'. The method relies on the fact that any symmetric transition between m and –m levels shown in Fig. 2, as we had discussed in the case of the central transition between m = +1/2 and m = -1/2 levels, is broadened only to second-order. Further, and more importantly, it turns out that there is a definite correlation between the orientation dependent frequencies associated with the multiple quantum transition with the corresponding frequencies of the observed central transition. Thus, by manipulating the multiple quantum and single quantum CT frequencies during the evolution and detection periods, respectively, in a 2D experiment, this frequency correlation can be established and the isotropic spectra devoid of second-order quadrupolar broadening can be obtained after a shearing operation on the 2D spectra. Pulse sequences used in MQMAS experiments are briefly discussed below.

1.4.1 Two Pulse sequence

The first MQMAS experiment proposed by Frydman consists of a two pulse sequence as shown in Figure - 5. As in any 2D experiment, the MQMAS experiment consists of the following four steps:

(i) R.F excitation to create multiple quantum coherences.

(ii) Evolution under this coherence for a sequentially incremented evolution period t_1

(iii) Reconversion of the multiple quantum coherence by an r.f pulse into the observable single quantum coherence for the central transition

(iv) Detection of the central transition signal during the acquisition period t_2.

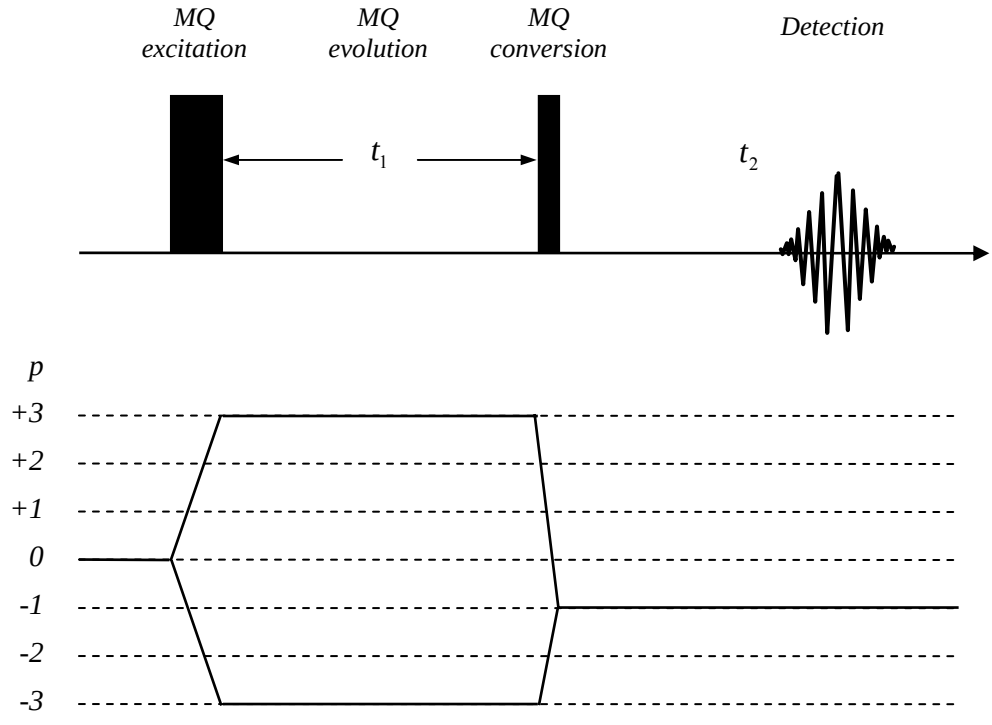

Figure – 5: The first two pulse sequence proposed by Frydman in MQMAS is shown along with the coherence transfer pathway. The phase cycling selects the 0 – (+3) – (-1) and 0 – (-3) – (-1) pathways.

This method is analogous to the cancellation of $H_Q^{(2)}$ by the evolution of the magnetization at two different angles in the DAS technique, except that in MQMAS the rotor angle remains fixed and the magnetization evolves under two different coherences. The draw back of the two-pulse sequence is the presence of dispersive signals in the 2D spectra which are obtained after 2D Fourier transformation, and this can be traced to the fact that unequal jumps are involved while selecting the echo and anti-echo pathways and the two mirror pathways do not contribute with the same efficiency. This problem is overcome in the z-filter method.

1.4.2 Z-filter Method

The aim of this method[32] is to make the two mirror-pathways symmetrical after the multiple-quantum evolution. The first pulse is a non-selective hard pulse to populate

the different coherence levels. The second pulse transfers the signal from coherence levels $\pm p$ to the level $p = 0$ so that the jump is equal to $|\Delta p| = 3$. This is essentially a

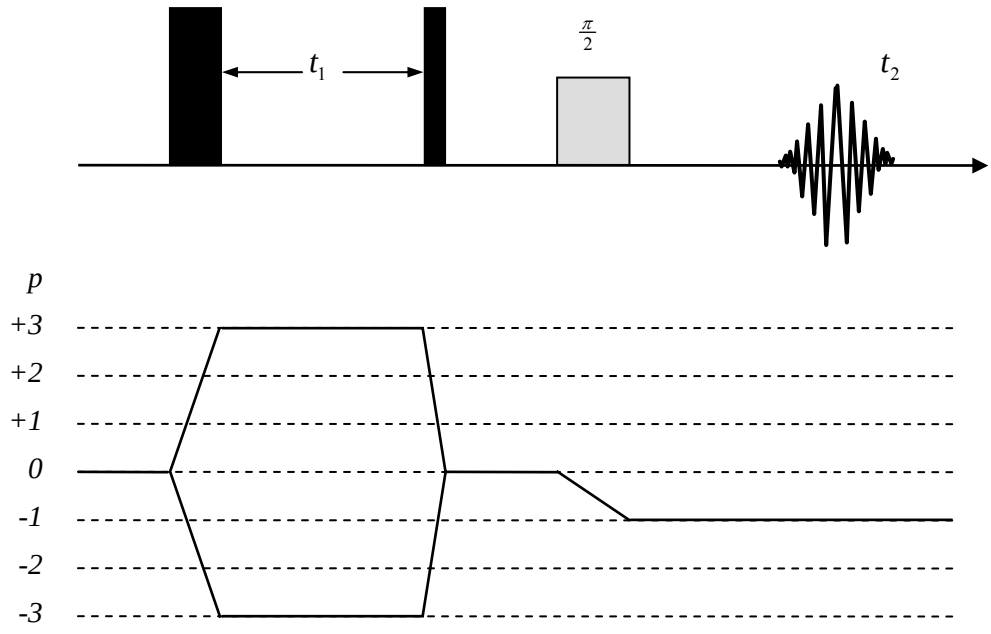

Figure – 6: Pulse Sequence used in the z-filter MQMAS experiment. The phase cycling for the r.f pulses and the receiver is constructed to select only the desired coherence transfer pathway, as shown, while rejecting other coherence pathways.

modification of the two pulse sequence to introduce a short z-filter delay which helps to symmetrize the echo and anti-echo pathways after the conversion step. The last central transition selective 90^0 pulse generates single quantum coherence and is readily observed. The main advantage of the z-filter method is that the equal contribution of the echo and antiecho pathways $(0 \rightarrow \pm p \rightarrow 0 \rightarrow -1)$ is achieved regardless of the spin number and the order of the selected coherences. The spectra presented in this thesis have been exclusively recorded using the z-filter sequence. Amoureux *et al* gives a detailed study of the conditions necessary to optimize the multiple-quantum excitation and reconversion[33]. A variety of extensions and enhancements of the basic sequence of Figure – 5 and 6 have been proposed, some of which achieve higher sensitivity, a more convenient quantitative characterization, or a higher resolution of the signals. A complete description of the advances in MQMAS NMR can be found in the recent review [34].

1.4.3 Shearing Transformation and Interpretation of MQMAS spectra

In MQMAS experiments the refocusing occurs along a slope given by the relation $R = A_4(I, p)/A_4(I,-1)$, where A_4 is the coefficient due to second-order terms and I and p denote the spin number and the order of MQ coherence, respectively. Since the echo signal moves along the slope R, the 2D spectra obtained after FT operations would also yield isotropic resonances when a skew projection is taken along a line of slope R. However, it is often convenient to perform a shearing operation during or after the FT operations so that the isotropic spectra are aligned parallel to the ω_1 direction. This would allow a projection of the sheared 2D data set parallel to ω_1 axis to get the isotropic spectrum, while a projection parallel to ω_2 would yield the MAS spectrum. Thus, shearing enables a tilting of the 2D data in such a way that the anisotropic and the isotropic part of the spectrum falls along the ω_2 and the ω_1 axis, respectively. If $S_e(t_1,t_2)$ and $S_a(t_1,t_2)$ are the echo and anti-echo signals respectively, after Fourier transformation along the t_2 dimension, we get $S_e(t_1,\nu_2)$ and $S_a(t_1,\nu_2)$. The shearing transformation is performed by multiplying $S_e(t_1,\nu_2)$ and $S_a(t_1,\nu_2)$ by $e^{-i\phi(t_1,\nu_2)}$ and $e^{i\phi(t_1,\nu_2)}$ respectively, where $\phi(t_1,\nu_2)$ is defined as $k\nu_2 t_1$ (with $k = 7/9$ for $I = 3/2$ case[35]. This shearing transformation is the equivalent of first order phase correction for a 1D spectrum. For all the MQMAS experiments presented in this thesis, the shearing was carried out using a macro program available in the Bruker data processing software XWIN-NMR.

The extraction of the chemical shift (δiso) and quadrupolar interaction ($P_Q = C_Q(1 + \eta^2/3)^{1/2}$ parameters from the experimental spectrum is illustrated in Figure – 7. This ^{27}Al 3QMAS spectrum of an aluminophosphate $AlPO_4$-18 is shown here in this plot, obtained after shearing transformation, the F_1 and F_2 axes are denoted as δ_{iso} and δ_2 respectively. After the shearing, the MQ dimension is scaled by an effective Larmor frequency so that the chemical shift (CS) Quadrupole Induced Shift (QIS) axes can be defined as follows. Denoting δ_{QIS} and δ_{QIS}^{iso} as the Quadrupolar Induced Shifts on the δ_2 and δ_{iso} axes respectively, following equation relates these as

$$\delta_{QIS}^{iso}\left(I,C_Q,\eta\right)=-\frac{10}{17}\delta_{QIS}\left(I,C_Q,\eta\right) \quad [25]$$

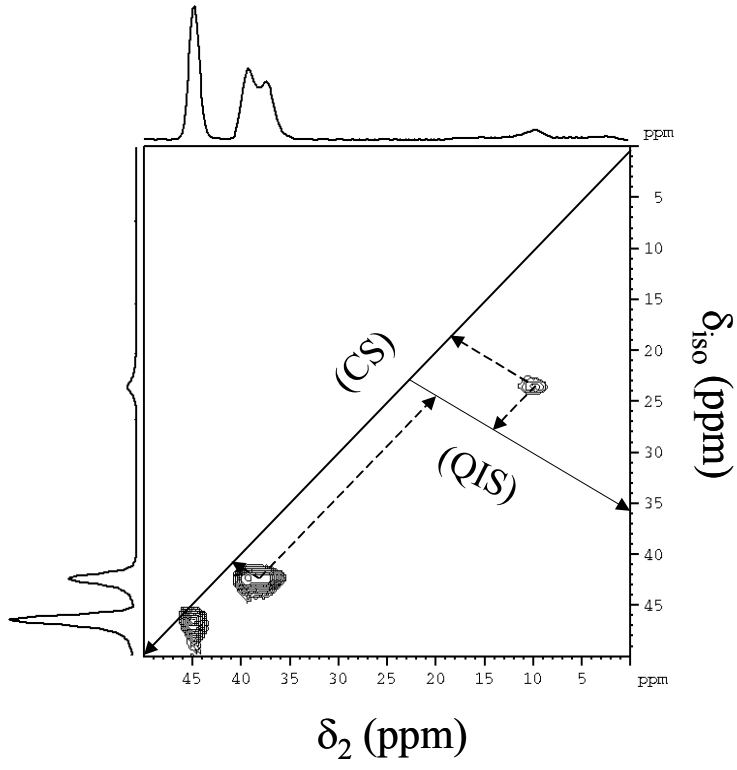

Figure – 7: ^{27}Al 3QMAS spectrum of $ALPO_4$ – 18 obtained after shearing. The axis along the diagonal represents the chemical shift axis (CS). QIS denotes the Quadrupole Induced Shift axis and has a slope of –10/17.

Therefore, the QIS axis can be drawn with a slope of $-10/17$ which correlates the Quadrupolar Induced Shift in both the dimensions. The scaling of the data by an effective Larmor frequency leads to a slope of $-10/17$ for the QIS axis and this is independent of the spin number *I* as well as the coherence order *p*. This allows us to use a single definition of the QIS axis for different MQMAS experiments[36]. Thus, by a projection of the center of gravity of the contour onto the sheared MQMAS and MAS axes, we can obtain δ_{CS} and δ_{QIS}. δ_2 and δ_{iso} from

$$\delta_2 = \delta_{CS} + \delta_{QIS} \quad [26]$$

$$\delta_{iso} = \delta_{CS} - \tfrac{10}{17}\delta_{QIS} \quad [27]$$

Making use of the definitions of δ_2 and δ_{iso}, one can obtain the mathematical expression for δ_{CS} and δ_{QIS} as,

$$\delta_{CS} = \frac{17\delta_{iso} + 10\delta_2}{27} \quad [28]$$

$$\delta_{QIS} = \tfrac{17}{27}\left(\delta_2 - \delta_{iso}\right) \quad [29]$$

Since δ_{QIS} is a function of the spin number *I*, as well as the Quadrupolar parameters C_Q and η_Q, it is not possible to extract both C_Q and η_Q from a single determination of δ_{QIS}. Hence a quadrupolar interaction parameter is introduced denoted by P_Q, which is

$$P_Q = C_Q\sqrt{1+\frac{\eta^2}{3}} \quad [30]$$

The Quadrupolar Induced Shift can be written as,

$$\delta_{QIS} = -\frac{3}{10}\cdot\frac{P_Q^2}{\omega_0^2}\cdot\frac{1}{K}\cdot 10^6 \quad [31]$$

where,

$$K = \frac{\left[4I\left(2I-1\right)\right]^2}{4I\left(I+1\right)-3} \quad [32]$$

Thus the quadrupolar interaction parameter P_Q can be determined from the experimental sheared 2D MQMAS spectrum.

The advent of MQMAS has led to various other developments in the area of solid state NMR of half-integer quadrupolar nuclei. These developments have led to many new applications and the practice of MQMAS itself is becoming routine. These developments include: hetero-[37,38] and homonuclear[39] correlation experiments based on cross-polarization[40], dipolar recoupling schemes incorporated into MQMAS (MQ-REDOR)[41] and sensitivity-enhancement techniques[42,43] and satellite-transition correlation experiments[44]. On the whole, MQMAS and the various other developments

hold great promise in the structural characterization of diverse materials. The potential use of MQMAS in the structural characterization of aluminum hydroxide polymorphs and in the study of structural transformations occurring in $ALPO_4$ materials are fully dealt with in Chapters 3 and 4.

1.5 Ab initio Calculation of NMR Parameters

The ab initio calculation of NMR parameters has been a well established method in quantum chemistry. Recent advances in the computational speed has made it possible to calculate NMR parameters theoretically even for large molecules. The usefulness of these calculations is mainly for assignment purposes. The assignment of NMR resonances has always been a significant complication when relating NMR spectra to molecular structure. The unique chemical shifts of different functional groups help in the assignment of chemically inequivalent nuclei, whereas assignment of crystallographically inequivalent nuclei is not possible with simple chemical shifts. The high accuracy achievable by modern chemical shielding calculations allows its use in questionable or ambiguous assignments. In the case of quadrupole nuclei, comparison of experimental and calculated values of both chemical shift and quadrupole coupling gives a better scrutiny in assignments. Calculations of chemical shielding and electric field gradient tensors were performed using the gaussian98 program[45].

1.5.1 Hartree – Fock Approximation and Basis Sets

In the Hartree – Fock approximation, the wave function is represented by a single electronic configuration, variationally optimized to provide the best possible approximation to the exact wave function. The Hartree – Fock approximation is particularly well suited to describe closed-shell ground-state wave functions at the molecular equilibrium geometry. This is the exact situation encountered in NMR experiments. Therefore the Hartree – Fock approximation is a useful method applicable to most systems of interest in NMR experiments providing results of reasonable quality.

Basis set is a group of numerical constants used in wavefunctions and are specific to an atom. It is a complete set of basis functions that is used to represent the molecular orbitals. A general expression for a basis function is given as:

$$\text{Basis function} = N * e^{(-\zeta r)}$$

Where, N is the normalization constant, ζ controls width of the orbital and r is the radius in Angstrom. Basis sets were first developed by Slater and a Slater Type Orbital (STO) is given by the function,

$$STO = Ne^{-\zeta r}$$

Although the STO equation is a wonderful approximation for the molecular orbitals, the problem lies in the time taken for computing the integrals using them. Calculating the STO of a molecule requires enormous computational power. Hence, a method of using a combination of Gaussian Type Orbitals in order to express the STO equation was developed by Boys. The following is the Gaussian Type Orbital (GTO) equation.

$$GTO = Ne^{-\zeta r^2}$$

The main difference in the 'r', STO uses 'r' and GTO uses 'r^2'. GTOs are easier and faster to calculate, but the downside is that they are not as accurate as STOs. To circumvent this problem a combination of many Gaussians are used. Most of the present day calculations are done using Gaussian Type Orbitals (GTOs).

Three important terms have to be mentioned here to describe the basis sets used commonly in current quantum chemical calculations.

(i) Split-valence basis set.

Since inner-electron shells are not as vital as the valence-electron shells for calculations, they are described by a single basis function, whereas a larger basis is used for valence atomic orbitals. This method is called Split-valence basis set.

(ii) Polarization functions

Till now each orbital was treated as a sole entity like 's', 'p', 'd', 'f', etc. Even though it is a good representation for an isolated atom, the picture changes with atoms come together, that is when there is bonding. When atoms comes close the charge distribution causes polarization effect which distorts the shape of the

atomic orbitals. For example, ‘s’ orbital can have a tinge of ‘p’ and ‘p’ can have a tinge of ‘d’ and so on. Hence this polarization should be taken into account by a good basis set.

(iii) Diffuse functions

When an electron is held far away from the nucleus like for an anion or in an excited state or for loosely bond electrons, it needs to be described more accurately by the basis set.

Now that we know the anatomy of a basis set, it is appropriate to explain how a basis set is commonly represented. The current representation of a basis set was developed by Pople. An example of a split valence Pople’s basis set is shown below,

6-31G

This means the core or the inner-shell GTO is represented by 6 Gaussians and the valence is described by two GTOs, one made of 3 Gaussians and the other with 1 Gaussian.

6-31G** or 6-31G(d,p)

This is same as a 6-31G basis set with the addition of polarization functions. The first ‘*’ means that a ‘d’ polarization function is added for non-hydrogen atoms and the second ‘*’ means that a ‘p’ polarization function is added for hydrogen atoms.

6-31++G** or 6-31++G(d,p)

This is same as 6-31G** with the addition of diffuse functions. First ‘+’ represents an addition of diffuse function for non-hydrogen atoms and the second ‘+’ for hydrogen atoms.

1.5.2 NMR Chemical Shielding Calculation

Calculation of magnetic properties necessitates consideration of the gauge-invariance problem[46,47]. This problem results from the fact that the magnetic field appears in the Hamiltonian in the form of a vector potential, the origin of which (gauge

origin) is not fixed. A common gauge origin (CGO) may be chosen, such as the origin of the molecular coordinate system, but computations short of an infinite basis set yield magnetic properties dependent on the choice of the gauge origin. Thus, the truncated basis sets, commonly used in ab initio calculations, result in significant error due to gauge variance. A trivial solution to the gauge-invariance problem would be the use of very large basis sets in order to minimize the gauge error, but this approach, due to large computational costs, is limited to small molecules. More advanced solutions to this problem are the distributed origin approaches that introduce local gauge origins to define the vector potential. In these methods, the gauge factors are either explicitly contained in the atomic orbitals or in some manner incorporated into the molecular or localized molecular orbitals. Methods that introduce local gauge-origins to define the vector potential are,

(i) IGLO (Individual Gauge for Localized Orbitals) method[48],
(ii) LORG (Localized Origins) method[49] and
(iii) GIAO (Gauge Independent Atomic Orbital)[50] method.

Among other methods, the GIAO or the Gauge Including Atomic Orbitals method is the most commonly used method for chemical shielding calculations due to its accuracy and its simplicity of implementation in NMR calculation programs. In this thesis all chemical shielding calculations were performed using this method.

Computational NMR methods provide absolute chemical shielding tensor values (σ) that need to be correlated to conventional δ values for comparison with results from typical NMR experiments. For example in a ^{1}H or ^{13}C experiment, δ (TMS) values would be assigned by reference to an in situ signal for TMS or predetermined standard. In principle, one could use a similar approach computationally, by computing the absolute chemical shift for TMS (σ_{TMS}) and taking the difference between that value and the absolute shift computed for the nucleus in question (σ_{cal}).

$$\delta_{cal} = \sigma_{TMS} - \sigma_{cal}$$

1.5.3 Electric Field Gradient Calculation

In this thesis, the electric field gradient tensors were calculated for ^{27}Al at the Hartree – Fock level with different basis set using gaussian98. As in most of the quantum chemical programs, gaussian98 also gives the values of EFG tensors in atomic units (a.u). The largest value of the EFG component, which is V_{ZZ} is multiplied by the Quadrupole moment to obtain the Quadrupolar coupling values.

$$C_Q = \frac{e^2 Qq}{h}$$

To calculate Quadrupole coupling constant in Hertz,

$$C_Q(\text{MHz}) = 234.968\, Q\, V_{zz}$$

where,

e = electron charge = 1.6022×10^{-19} C
h = Planck's constant = 6.626069×10^{-34} J S = 6.626069×10^{-34} C V S
eq = V_{ZZ} = Electric field gradient in a.u (1 a.u. = 9.71736×10^{21} V m^{-2})
Q = Quadrupole moment in Barn (1 Barn = 10^{-28} m^2)

1.5.4 Cluster Model and Locally Dense Basis set

Since the computational time requirement for a calculation increases exponentially with the number of atoms or electrons involved, it is not a smart idea to do a quantum chemical calculation for a very large crystal structure or a zeolite. It is better to break them into small clusters. A cluster is a careful selection of atoms within a crystal structure aiming at an accurate determination of local properties of an atom. All calculations presented in this thesis involve clusters. Description of specific clusters used is given in the appropriate sections in corresponding chapters of the thesis. This way of breaking large structures into smaller clusters for calculations significantly decrease the computational time without compromise in the accuracy of the properties calculated.

We saw that computational time requirement increases with increase in the number of atoms. Similarly, use of larger basis set also increases computational time. A smaller basis could be computationally less demanding but there is a compromise in the accuracy of the results. Hence adoption of a "locally dense" basis approach[51] for the quantum chemical calculations would enable to reduce the length of calculations while maintaining good accuracy of the results. The locally dense basis set approach to the calculation of nuclear magnetic resonance shielding is one in which a sufficiently large or dense set of basis functions is used for an atom or molecular fragment containing the resonant nucleus or nuclei of interest and fewer or attenuated sets of basis functions employed elsewhere. Provided the dense set is of sufficient size, this approach is capable of determining chemical shielding nearly as well as a calculation with a balanced basis set of quality equal to the locally dense set, but with considerable savings of CPU time.

1.6 References:

1. Bloch, F.; Hansen, W. W.; Packard, M., Phys. Rev. **69**, 127 (1946).
2. Ernst R. and Anderson W. Rev. Sci. Instrum., **37,** 93 (1966)
3. Haberlen U. High Resolution of NMR in Solids: Selective Averaging, Advances in Magnetic Resonance, Academic Press, (1976)
4. Harris, R. K., Nuclear Magnetic Resonance Spectroscopy, second edition, John Wiley & Sons, New York (1986), corrected reprint, 1994.
5. Akivis, M. A.; Goldberg, V. V., Introduction to Linear Algebra and Tensors, Prentice-Hall, Englewood Cliffs, NJ (1972), Dover Publications (New York) reprint 1977.
6. M.E. Rose, "Elementary Theory of Angular Momentum, John Wiley, New York, 1961, p.50.
7. M. Mehring, 'Principles of High Resolution NMR in Solids', Springer, Berlin, 1983, p221.
8. K. Schmidt-Rohr and H. W. Spiess, 'Multidimensional Solid-State NMR and Polymers', Academic Press, New York, 1994.
9. E. R. Andrew, A. Bradbury, and R. G: Eades, Nature (London) **182**, 1659 (1958).

10. E. R. Andrew, A. Bradbury, and R. G. Rades, Nature (London) **183**, 1802 (1959).
11. I. J. Lowe, Phys. Rev. Lett. **2**, 285 (1959).
12. (a) Kolbert A.C., Raleigh D.P., and Griffin R.G., J. Magn. Reson., **82**, 483, (1989)
    a. Herzfeld J., Berger A.E., J. Chem. Phys., **73**, 6021, (1980).
13. (a) F Waugh J. S., Huber L. M. and Haeberlen U. Phys. Rev. Lett. (1968), 20, 180-2
    (b) G Vinogradow E., Madhu P.K., and Vega S. Chem. Phys. Lett. 314, 443-450 (1999)
14. T. Gullion and J. Schaefer, J. Magn. Reson., **1989**, 81, 196.
15. T. Gullion Concepts in Magnetic Resonance (1998), 10(5), 277
16. (a) Samoson, A. In *Encyclopedia of Nuclear Magnetic Resonance*; Grant, D. M., Harris, R. K., Eds.; John Wiley & Sons: Chichester, U.K., 2002; Vol.9, pp 59-64. (b) A. Samoson, T. Tuherm, and J. Past., J. Magn. Reson., **149**, 264-267, 200
17. Bennet A. E.; Rienstra C. M.; Auger M.; Lakshmi K. V.; Griffin R. G. *J. Chem. Phys.* **1995**, *103*, 6951.
18. A. Detken, E. H. Hardy, M. Ernst, and B. H. Meier, Chem. Phys. Lett. **356**, 298 (2002)
19. A. Pines, M. G. Gibby, J. S. Waugh, J. Chem. Phys. 1973, 59, 569.
20. S. R. Hartmann, E. L. Hahn, Phys. Rev. 1962, 128, 2042.
21. A. Abraham, Principles of Nuclear Magnetism, Clarendon, Oxford, 1961
22. D D. Massiot, F. Fayon, M. Capron, I. King, S. Le Calvé, B. Alonso, J-O. Durand, B. Bujoli, Z. Gan, G. Hoatson. Magnetic Resonance in Chemistry 40 *70-76* (2002)
23. (a) S. Ganapathy, S. Schram and E. Oldfield, JCP (1982), 77(9), 4360.
    (b) S. Ganapathy, Jay Shore and Eric Oldfield, CPL (1990), 169(4), 301.
24. K. T. Mueller, B. Q. Sun, G. C. Chingas, J. W. Zwanziger, T. Terao, A. Pines, J. Magn. Reson. 1990, 86, 470.
25. J. H. Baltisberger, S. L. Gann, E. W. Wooten, T. H. Chang, K. T. Mueller, A. Pines, J. Am. Chem. Soc. 1992, 114, 7489.

26. K. T. Mueller, Y. Wu, B. F. Chmelka, J. Stebbins, A. Pines, J. Am. Chem. Soc. 1991, 113, 32.
27. (a) A. Samoson, E. Lippmaa, A. Pines, Mol. Phys. 1988, 65, 1013,
(b) A. Samoson, A. Pines, Rev. Sci. Instrum. 1989, 60, 3239.
28. A. Llor, J. Virlet, Chem. Phys. Lett. 1988, 152, 248.
29. Y. Wu, B. Q. Sun, A. Pines, A. Samoson, E. Lipmaa, J. Magn. Reson. 1990, 89, 297.
30. A. Medek, J. S. Harwood, L. Frydman, J. Am. Chem. Soc. 1995, 117, 12779.
31. L. Frydman, J. S. Harwood, J. Am. Chem. Soc. 1995, 117, 5367.
32. J.-P. Amoureux, C. Fernandez, S. Steuernagel, J. Magn. Reson., A, **123**, 116 (1996)
33. J. P. Amoureux, C. Fernandez, and L. Frydman, *Chem. Phys. Lett.* **259**, 347 (1996).
34. J.P. Amoureux,; M. Pruski,, Encyclopedia of Nuclear Magnetic Resonance (2002), 9 226-251
35. A. Goldbourt, P. K. Madhu; Monatshefte fur Chemie 133, 1497–1534 (2002)
36. J.-P. Amoureux, C. Fernandez, *Solid State NMR*, 1998, **10**, 211
37. J. C. C. Chan, J. Magn. Reson. 1999, 140, 487.
38. S. H.Wang, S. M. de Paul, L. M. Bull, J. Magn. Reson. 1997, 125, 364.
39. Ajithkumar, T. G.; van Eck, E. R. H.; Kentgens, A. P. M Solid State Nuclear Magnetic Resonance (2004), 26(3-4), 180-186.
40. Pruski, M.; Lang, D. P.; Fernandez, C.; Amoureux, J. P. Solid State Nuclear Magnetic Resonance (1997), 7(4), 327-331.
41. Fernandez, C.; Lang, D. P.; Amoureux, J. P.; Pruski, M. Journal of the American Chemical Society (1998), 120(11), 2672-2673.
42. F. H. Larsen, J. Skibsted, H. J. Jakobsen, N. C. Nielsen, J. Am. Chem. Soc. 2000, 122, 7080.
43. F. H. Larsen, A. S. Lipton, H. J. Jakobsen, N. C. Nielsen, P. D. Ellis, J. Am. Chem. Soc. 1999, 121, 3783.
44. Z. H. Gan, J. Am. Chem. Soc. 2000, 122, 3242.
45. Gaussian 98, Revision A.9, M. J. Frisch, G. W. Trucks, H. B. Schlegel, G. E. Scuseria, M. A. Robb, J. R. Cheeseman, V. G. Zakrzewski, J. A.

Montgomery, Jr., R. E. Stratmann, J. C. Burant, S. Dapprich, J. M. Millam, A. D. Daniels, K. N. Kudin, M. C. Strain, O. Farkas, J. Tomasi, V. Barone, M. Cossi, R. Cammi, B. Mennucci, C. Pomelli, C. Adamo, S. Clifford, J. Ochterski, G. A. Petersson, P. Y. Ayala, Q. Cui, K. Morokuma, D. K. Malick, A. D. Rabuck, K. Raghavachari, J. B. Foresman, J. Cioslowski, J. V. Ortiz, A. G. Baboul, B. B. Stefanov, G. Liu, A. Liashenko, P. Piskorz, I. Komaromi, R. Gomperts, R. L. Martin, D. J. Fox, T. Keith, M. A. Al-Laham, C. Y. Peng, A. Nanayakkara, M. Challacombe, P. M. W. Gill, B. Johnson, W. Chen, M. W. Wong, J. L. Andres, C. Gonzalez, M. Head-Gordon, E. S. Replogle, and J. A. Pople, Gaussian, Inc., Pittsburgh PA, 1998.

46. Chesnut, D. B. *Ab Initio Calculations of NMR Chemical Shielding*; Webb, G. A., Ed.; Academic Press: San Diego, 1994; Vol. 29.
47. Chesnut, D. B. *Some Recent Ab Initio Calculations of the NMR Chemical Shift*; Webb, G. A., Ed.; Academic Press: San Diego, 1989; Vol.21.
48. Schindler, M.; Kutzelnigg, W. *J. Chem. Phys.* 1982, *76*, 1919.
49. Hansen, A. E.; Bouman, T. D. *J. Chem. Phys.* 1985, *82*, 5035.
50. Ditchfield, R. *J. Chem. Phys.* 1972, *56*, 5688.
51. D. B. Chesnut, B. E. Rusiloski, K. D. Moore, D. A. Egolf. *J. Comput. Chem.*, 14:1364, 1993.

CHAPTER II

^{13}C, ^{15}N and ^{2}H Chemical Shieldings and Study of Molecular Self-Assembly in Cyanuric Acid – Melamine Complex

Part of this chapter has been published in,
Solid State NMR of a Molecular Self-Assembly: Multinuclear Approach to the Cyanuric Acid-Melamine System.
Organic Letters (2001), 3(12), 1921-1924

2.1. Introduction

This chapter deals with the determination of the isotropic ^{13}C, ^{15}N and ^{2}H chemical shieldings, both experimentally and theoretically, as an aid in the complete solid state NMR characterization of Cyanuric Acid (CA), Melamine (MA) and the 1:1 CA:MA complex. This also represents the first such attempt to study the supramolecular self-assembly through such a tri-nuclear solid state NMR approach. The ^{13}C chemical shift tensors and the ^{2}H electric field gradient tensors were determined by computer simulations of the experimental spectra obtained at different spinning speeds. ^{13}C chemical shift tensors were determined by *ab initio* calculations. ^{13}C signal assignments in CA, MA and CA:MA complex were made possible by comparison of the experimental results with *ab initio* calculations.

Supramolecular hydrogen-bonded assemblies are novel systems which exhibit fascinating molecular architectures due to a self-assembly of structurally complementing molecules, having donor and acceptor groups, and hold considerable potential for development of molecular devices.[1,2] Structural characterization of supramolecular structures is the key to understand the molecular details of the self-assembly and how they govern the end properties of these materials. X-ray crystallographic analysis has provided considerable insights into the structural organization of self-assembled systems.[3,4] However, this technique becomes restrictive when the self assembled species fail to form single crystals or can not be crystallized due to poor solubility. In view of this, exploration of alternative experimental approaches for characterization and derivation of structural information on molecular self assembly is in order. Though the capability of solid-state NMR for such analysis is well recognized,[5] the application of solid state NMR in studying molecular self assembly have remained far and in between.

Cyanuric acid and Melamine have been chosen as excellent models systems for the solid state NMR studying molecular self assembly. Cyanuric acid and its analogues[6] are also used as DNA nucleobase mimics, which also defy crystallization and hence solid state NMR becomes a very important tool for characterizing them. In this chapter, it is demonstrated through the choice of cyanuric acid (**CA):** melamine (**MA**)

assembly,[4] that a tri-nuclear solid state NMR approach using magic angle spinning (MAS) NMR , involving naturally abundant (^{13}C, ^{15}N) and easily deuterated (^{2}H) nuclei, gives structural information which is in reliable agreement with that derived from X-ray technique and hence may offer newer opportunities to study other molecular assemblies which are difficult to obtain in their crystalline form.

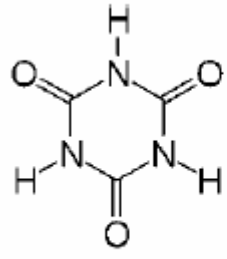

CA

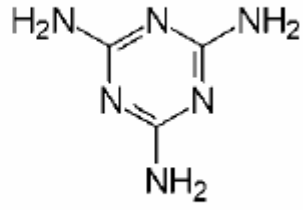

MA

Cyanuric acid (**CA**), a six-membered cyclic imide with alternate arrangement of hydrogen bond donors and acceptors, forms a network of well-defined robust hydrogen bonded systems arranged on a molecular tape[7] (Figure 1a). The successive tapes are held together by single hydrogen bonds from C(1)O of one chain with N(1)H of the other chain. **CA** is symmetric in monomeric form, but in the hydrogen-bonded supramolecular form, the C(1) and N(1) atoms located on the 2-fold symmetric axis have a hydrogen bonded environment that is different from other C(2) and N(2). Melamine (**MA**), the supramolecular hydrogen-bonded complement of **CA,** is likewise symmetrical in monomeric form. In the supramolecular crystal[8] structure, the three exocyclic amino groups are hydrogen-bonded differently (Figure 1b), leading to nonequivalence in the system. In the 1:1 **CA:MA** complex, the full complementation of hydrogen bond donor and acceptor sites leads to a hexagonally symmetrical rosette structure[4] (Figure 1c), and the asymmetry imposed by the supramolecular environment in the monomers disappears.

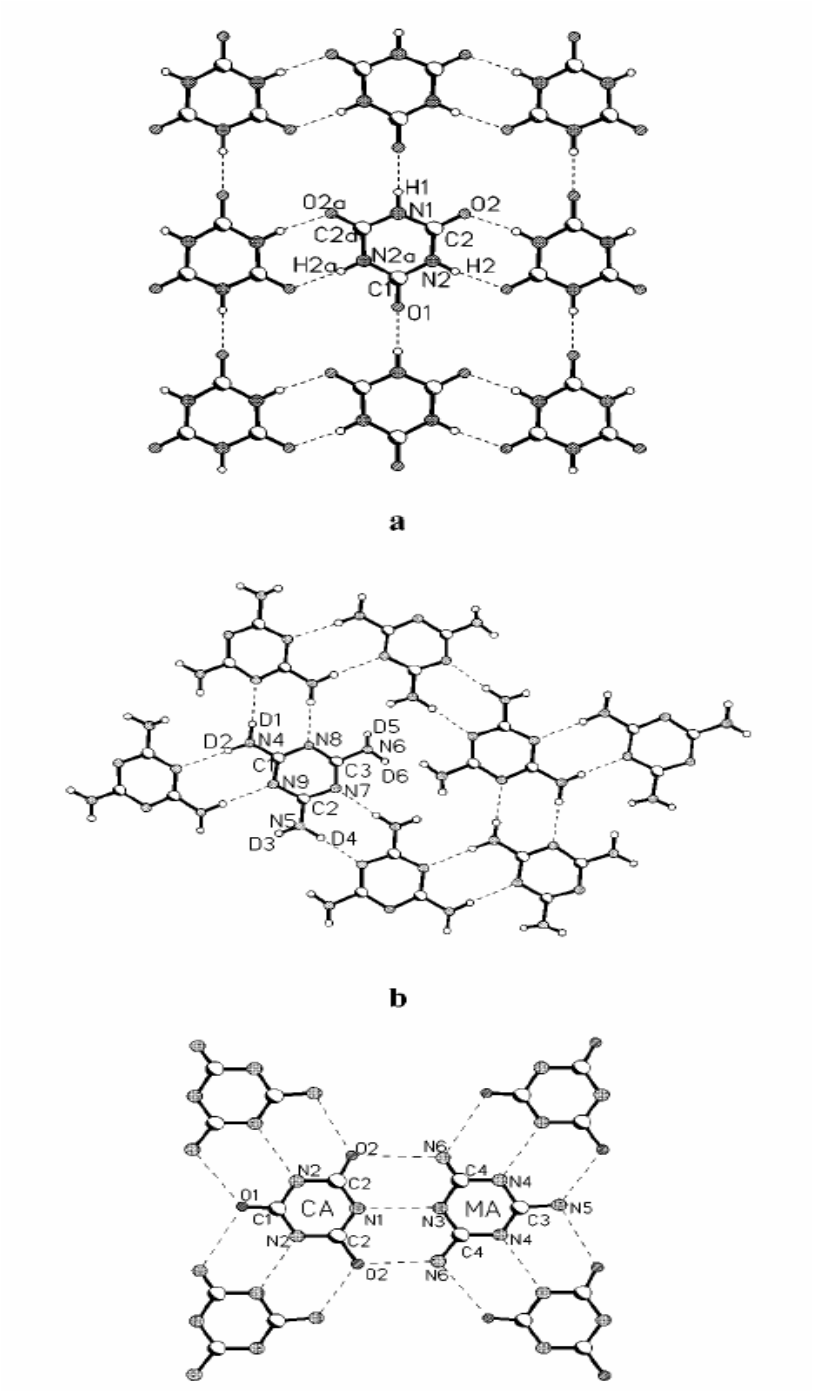

Figure 1. Hydrogen bonding patterns in (a) Cyanuric Acid (**CA**), (b) Melamine (**MA**), (c) **CA:MA** 1:1 complex derived from their crystal structures.[7,8] In (c), D1 is linked to N1, D2 is linked to N2, D3 linked to N5, D4, D5 linked to N6.

The main endeavor of this work is the application of ^{2}H, ^{13}C and ^{15}N solid state MAS NMR techniques to lyophilized samples of **CA**, **MA**, and 1:1 **CA:MA** complex and to examine whether the NMR data reliably reflect the structural features seen in

crystal structures, by a comparison of the experimental NMR parameters with theoretical calculations. The results have implications for extending the solid state NMR as a potential technique to study molecular self-assembly in other complexes which are difficult to obtain in their crystalline form.

2.2 Solid State NMR Results

All high-resolution solid state MAS NMR experiments were performed on an 11.7 T Bruker Avance 500 NMR spectrometer at ambient room temperature (295 K). The NMR experiments were performed using a Bruker double resonance CPMAS probe at ^{1}H, ^{13}C, ^{2}H and ^{15}N frequencies of 500.13, 125.78, 76.77 and 50.68 MHz respectively. To reduce the prohibitively long proton T_1 (> 500 s), paramagnetic Cu^{2+} doping was done by lyophilizing the non-deuterated samples with 0.01% $CuCl_2$. Cu^{2+} doping aids in reducing the T_1 of the abundant spins (protons) by one or two orders of magnitude and has negligible effects on the rare spins (^{13}C, $^{!5}N$) in causing line shift or broadening[8a]. Thus, Cu^{2+} doping of the samples afforded an efficient data collection in our ^{1}H-^{13}C and ^{1}H-^{15}N CP-MAS experiments. Typically, we used a recycle time of 5 sec in the ^{1}H-^{13}C and ^{15}N CP-MAS experiments. Spinning speed was maintained at 8 kHz for most of the experiments and slow spinning of 2 and 4 KHz was additionally used in ^{13}C experiments to retrieve the chemical shielding parameters more reliably from the side band intensities. Typically 400, 4000, and 600 transients were accumulated for ^{13}C, ^{15}N, and ^{2}H experiments, respectively. Resolution enhancement with a sine-squared window function was used prior to Fourier transformation. Deuterated samples of **CA**, **MA**, and **CA:MA** (1:1) were prepared by lyophilizing twice from D_2O, followed by methanol, and were subsequently used for ^{2}H NMR experiments.

2.2.1 Cyanuric Acid and Melamine

Figure 2 shows the cross polarization-magic angle spinning (CP-MAS)[12] ^{1}H- ^{13}C (panel A), ^{1}H-^{15}N NMR spectra (panel B), and MAS[13] ^{2}H NMR (panel C) of (i) **CA**, (ii) **MA**, and (iii) 1:1 **CA: MA** complex, lyophilized from methanol. The ^{13}C, ^{15}N, and ^{2}H resonance assignments and chemical shifts derived for the donor and acceptor groups in cyanuric acid, melamine and cyanuric acid-melamine complex are given in Table 1.

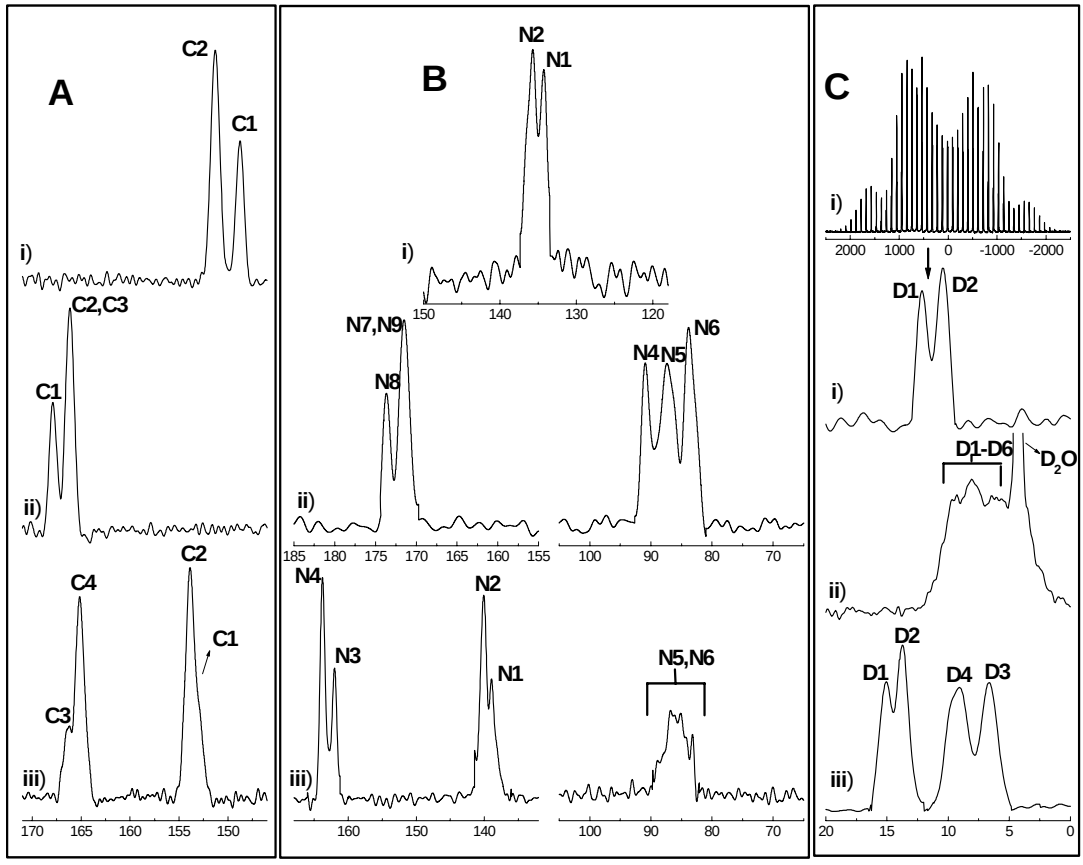

Figure – 2. ^{1}H - ^{13}C CPMAS (**A**), ^{1}H - ^{15}N CPMAS (**B**), and ^{2}H MAS (**C**) NMR spectra of cyanuric acid (**CA**) (i), melamine (**MA**) (ii), and 1:1 cyanuric acid:melamine (**CA:MA**) complex (iii). The labeling of atoms for i, ii, and iii follow that shown in Figure 1a-c, respectively.

Despite the chemical equivalence of carbon atoms in the monomer, the ^{13}C NMR spectra [Figure 2A (i) and (ii)] reveal two signals in a 2:1 intensity ratio. This is in complete agreement with their crystal structures,[7,8] which show nonequivalence arising from a differently hydrogen-bonded environment in the supramolecular assembly. The 2-fold axis through the central C, N atoms of **CA** and **MA** rings facilitates the assignments to unique (C1, N1, D1) and symmetry-related (C2, N2, D2) atoms.[7,8] The sideband intensities at 8 kHz spinning were found to be negligible in ^{15}N spectra. The relative intensities of the different ^{15}N resonances in the ^{15}N spectra could thus be directly estimated from the 8 kHz spinning spectra. In the case of ^{13}C CPMAS spectra, the relative peak intensities were also estimated from the 8 kHz spinning spectra. This was validated by independent ^{1}H-^{13}C CP dynamics experiments in which the developments of the various carbon resonances were monitored. CP dynamics

experiments in the 1:1 CA:MA complex show similar ^{13}C CP behavior for the ring carbons, irrespective of Cu^{2+} doping (T_{IS} = 5.1, 5.8 ms, $T_{1\rho}{}^{H}$ = 16.4, 16.7 ms), at 50 kHz rf field (shown in Figure – 3), also validating ^{13}C relative intensity measurements at a single mixing time (1 ms) for the spectra shown in Fig. 2 (**A**).

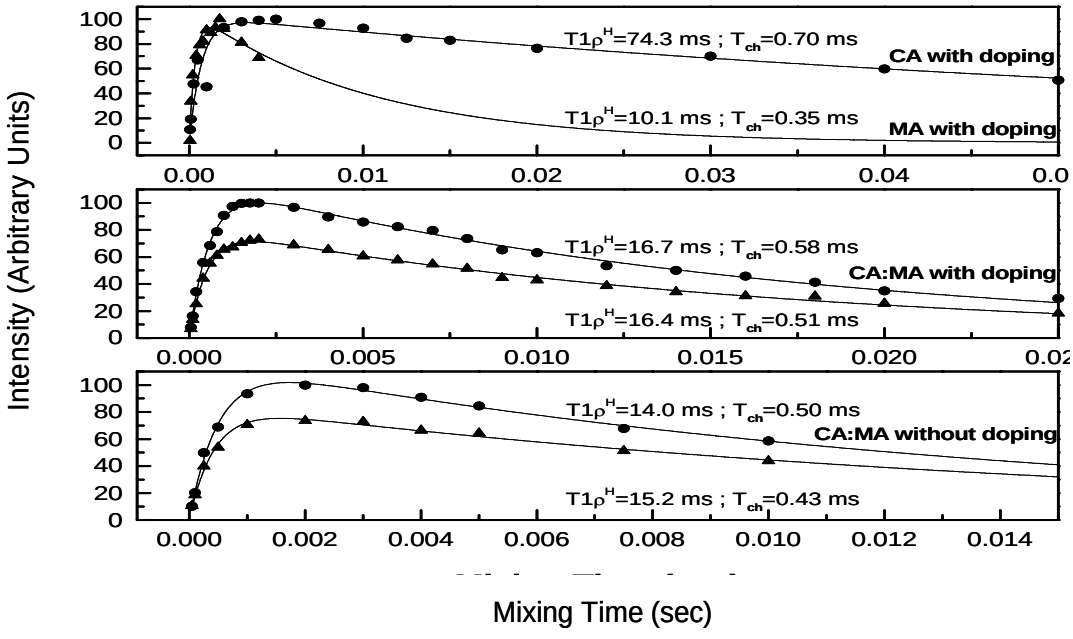

Figure – 3. ^{1}H-^{13}C cross-polarization dynamics for the different ring carbons in Cyanuric Acid, Melamine and the 1:1 Cyanuric Acid:Melamine complex. Experimental data are fit to the equation $I = I(0) / (1- T_{IS} / T_{1\rho}) * (\exp (- \tau/ T_{1\rho}) – \exp (- \tau/ T_{IS}))$ and the "best fit" curves are shown. The CP dynamics for undoped and Cu^{2+} doped samples are shown and the cross-polarization time (T_{IS}) and proton rotating frame spin-lattice relaxation time ($T_{1\rho}{}^{H}$), determined from the fit, are also indicated.

In ^{15}N NMR, two signals in a 2:1 ratio are seen for the ring nitrogens of **CA** [Figure 2B (i)] and **MA** [Figure 2B (ii), δ 170-175], while the three exocyclic NH_2 groups of **MA** result in separate signals in the region δ = 80-95. The observed 3-fold multiplicity for the $^{15}NH_2$ resonances in **MA** (N4-N6, Figure 2B) arises from a magnetic nonequivalence imposed on them by the supramolecular environment in which the three chemically identical amino groups individually form two, one, and no hydrogen bonds in the supramolecular network. This inequivalence is not reflected in the ^{15}N or ^{13}C resonances of ring atoms of **MA**, perhaps because of smaller chemical shift dispersion. Despite the complex arrangement of **MA** in the crystal, the ^{13}C and ^{15}N signals can be tentatively assigned on the basis of the hydrogen bond environments as well as

strengths.[8] Intermolecular hydrogen bonding involving deuterons is evident from the correlation of observed ^{2}H chemical shifts with the hydrogen bonding distances ($r_{D1\text{-}O1}$) 1.758, $r_{D2\text{-}O2)}$ 1.774 Å) seen from Table – 2.

Table-1

Experimentally Determined Solid State ^{13}C, ^{15}N and ^{2}H Chemical Shifts[a,b]

Compound	Chemical Shifts (ppm)		
	^{13}C	^{15}N	^{2}H
Cyanuric Acid (CA)	151.3 **(C2)** 149.0 **(C1)**	135.7 **(N2)** 134.3 **(N1)**	12.0 **(H1)** 10.5 **(H2)**
Melamine (MA)	167.8 **(C1)** 166.2 **(C2,C3)**	90.9 **(N4)**, 87.4 **(N5)**, 83.9 **(N6)** 173.7 **(N8)**, 171.6 **(N7,N9)**	9.7-5.6 **(H1 – H6)**
Complex (CA:MA)	165.2 **(MA)**, 153.6 **(CA)**	163.8, 162.0, 85.1 **(MA)** 140.1, 139.1 **(CA)**	8.5, 6.5 **(MA)** 14.9, 13.8 **(CA)**

[a]Chemical shifts are externally referenced with respect to TMS for ^{13}C and ^{2}H and liquid ammonia for ^{15}N. [b]The assignments and labeling of ^{13}C, ^{15}N and ^{2}H correspond to those marked in Figure 2.

Table – 2

Structural Data for CA, MA and CA:MA

System	Crystal symmetry	No. of inequivalent sites			Hydrogen bond distances (Å)
		^{13}C	^{15}N	^{2}H	
CA (*ND*) (Ref. 7)	C2/n a = 7.90 Å α= 90.0^0 b= 6.73 Å β= 130.67^0 c=11.95 Å γ= 90.0^0	2	2	2	H_1—O_1=1.758 H_2—O_2=1.774
MA *(ND)* (Ref. 8)	$P2_1/a$ a=10.61 Å α = 90.0^0 b= 7.49 Å β = 112.26^0 c= 7.29 Å γ= 90.0^0	3	6	6	H_1—N_9=2.052 H_2—N_8=2.110 H_4—N_7=2.001 H_6—N_8=2.080
CA:MA *(XD)* (Ref. 4)	C2/m a=14.85 Å α= 90.0^0 b= 9.64 Å β = 92.26^0 c= 3.58 Å γ= 90.0^0	2	4	Not determined	------

ND: Neutron Diffraction **XD:** X-ray Diffraction

2.2.2 CA:MA (1:1) Complex

^{15}N chemical shielding effects have long been used as an effective tool for investigating H-bonding interactions.[14,15] In nucleosides, the significant shielding effects (lower frequency shift) observed for H-bonded pyridine-type N atoms and decreased shielding (high frequency shift) of N-H moieties are considered to be characteristic of proton acceptor and donor sites, respectively.[16] In comparison with the asymmetric spectra of individual components [(Figure 2 (i) and (ii)], the solid state NMR of the 1:1 complex [(Figure 2 (iii)] exhibited a more symmetric pattern, expected of a molecular self assembly (Figure 1c). In the 1:1 **CA:MA** complex, the ring nitrogens of **MA** (N3, N4) experience a large low-frequency shift ($\Delta\delta$ ~ -10 ppm) compared to that in neat **MA** (N7- N9), whereas that of **CA** (N1 and N2) showed a reverse trend ($\Delta\delta$ ~ +5 ppm). This is in agreement with their respective role as stronger H-bonding acceptor and donor. The ^{15}N chemical shift dispersion for amino nitrogen of **MA** in the complex is not large enough to resolve all the expected resonances, and hence a direct comparison of chemical shift differences upon complexation was rendered difficult.

Further evidence for hydrogen bonding in the **CA:MA** assembly is provided by the ^{13}C data, which displays a lower frequency shift ($\Delta\delta$ = -2.5 ppm) for the aromatic carbons of **MA** and a higher frequency shift ($\Delta\delta$ = + 2.5 ppm) for the ring carbons of **CA**. The small magnitude of $\Delta\delta$ in ^{13}C is attributable to the disposition of carbons that are two bonds away from the hydrogen-bonding site. The hydrogen-bonding effects are also seen from the anisotropic ^{13}C chemical shielding parameters, namely the anisotropy of chemical shielding ($\Delta\delta$) and the asymmetry parameter (η), that were obtained from numerical simulation of the experimental data. The results obtained from computer simulations of ^{13}C slow MAS spectra are tabulated in Table – 3. The experimental and simulated ^{13}C CPMAS spectra are shown in Figure 4, 5 and 6, respectively.

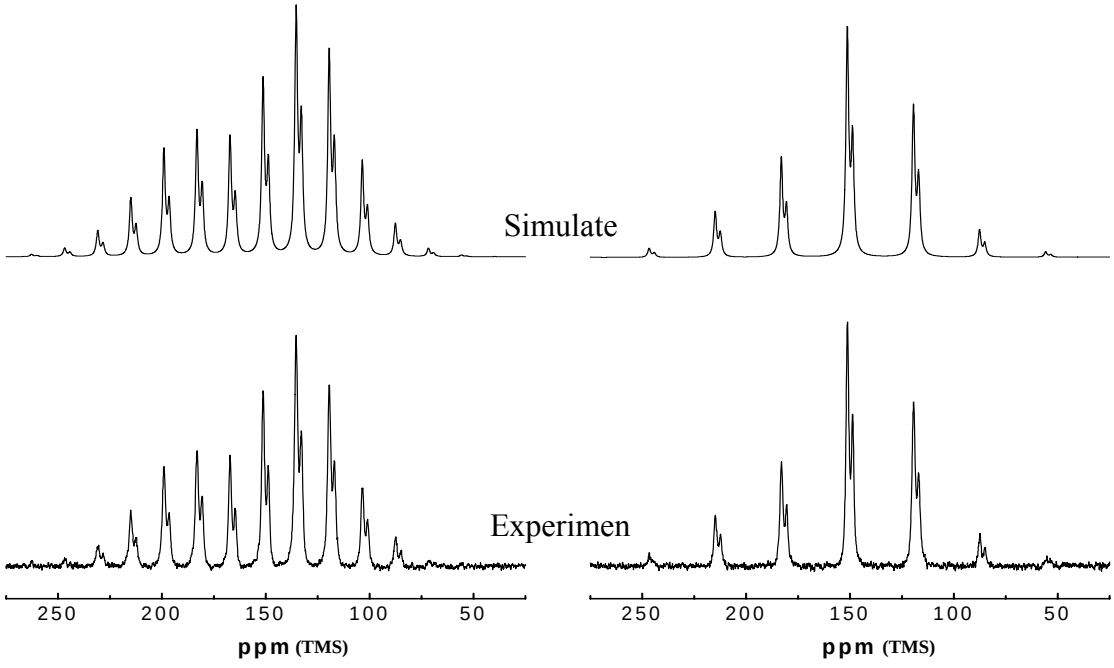

Figure – 4. Experimental and theoretically simulated ^{13}C slow MAS spectra of Cyanuric Acid at the spinning speed 2 kHz (left) and 4 kHz (right).

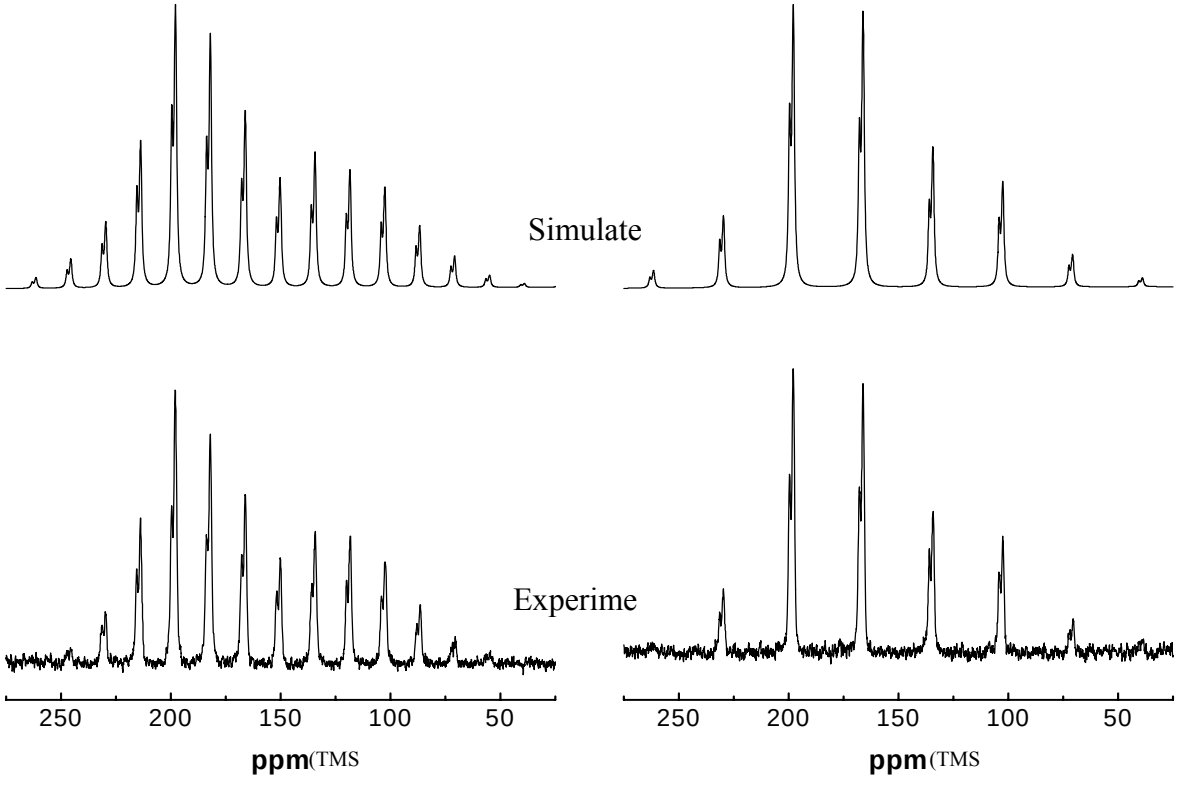

Figure – 5. Experimental and theoretically simulated ^{13}C slow MAS spectra of Melamine at 2 kHz (left) and 4 kHz (right).

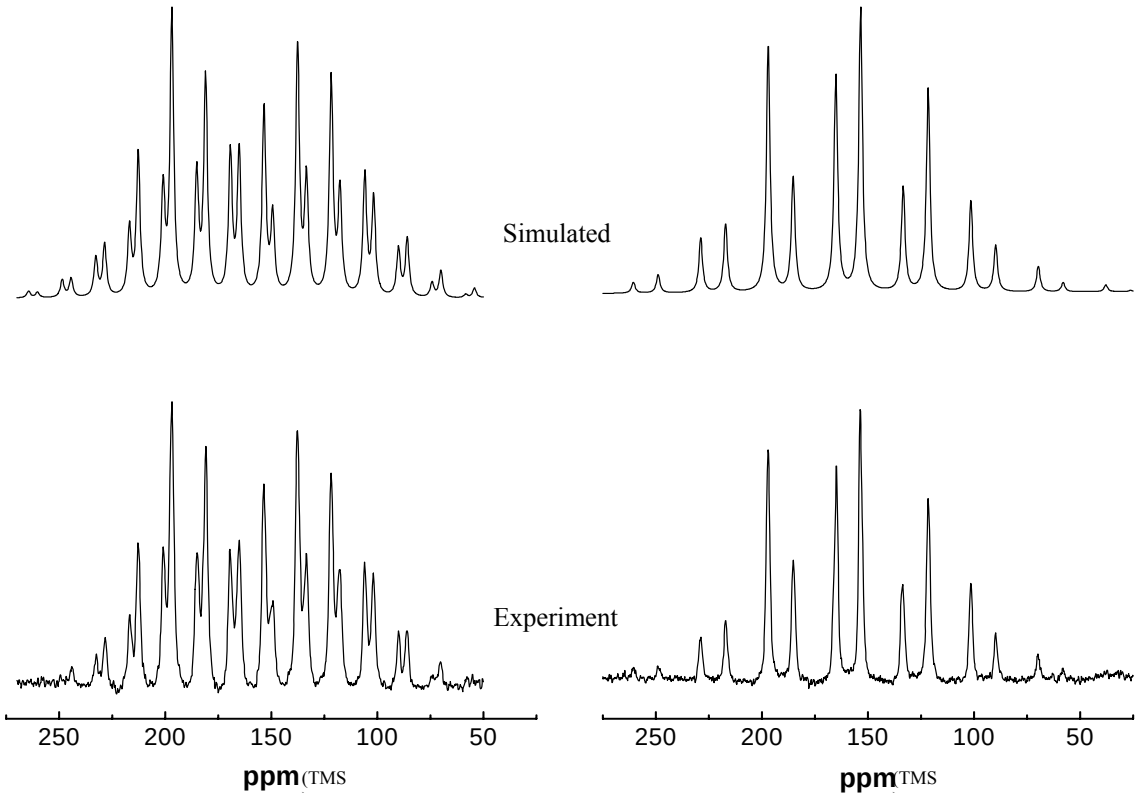

Figure – 6. Experimental and theoretically simulated ^{13}C slow MAS spectra of the Cyanuric Acid – Melamine (CA:MA) complex at 2 kHz (left) and 4 kHz (right).

Table – 3

Results of computer simulation of ^{13}C slow MAS spectra

System	^{13}C Simulation results		
	$\delta\Delta$ *(ppm)*	δ_{iso} (ppm)	η
CYANURIC ACID	134.3 135.8	149.0 151.3	0.56 0.61
MELAMINE	146.2 151.3 153.0	167.8 166.2 166.2	2.56 2.38 2.37
1:1 CYANURIC ACID:MELAMINE	144.6 152.7	153.6 165.2	0.53 2.32

^{13}C isotropic shifts (δ_{iso}) are with reference to tetra methyl silane

All the deuterium in the donor and acceptor groups of the **CA:MA** complex are detected with a 1:2 multiplicity for ^2H in chemically similar environments (Figure 2C), affirming the 2-fold symmetry in the **CA:MA** complex. The ^2H experimental data was also numerically simulated to get the quadrupole coupling constant and asymmetry parameter. The full ^2H NMR spectra of CA and MA are shown in Figure – 7 and that of CAMA is shown in Figure – 8. The results are tabulated in Table – 4. A significant high-frequency shift ($\Delta\delta$ = 3 ppm), decrease in quadrupole coupling constant (e^2Qq/h), and increase in asymmetry parameter (η) for the electric field gradient tensor observed for the N-D of **CA** unit are in accord with strong hydrogen bonds[17] in the supramolecular structure. The ^2H chemical shift dispersion for the amino deuterons is not large enough to resolve all the expected six resonances, whereas a good dispersion is seen for them in the **CA:MA** complex, with the observance of expected three resonances. The ^2H quadrupole coupling constant and asymmetry parameter for ^2H of ND showed very little change after complexation with **CA**, suggesting that the strength of hydrogen bonding for the amide group in the neat as well as the complexed structure is similar.

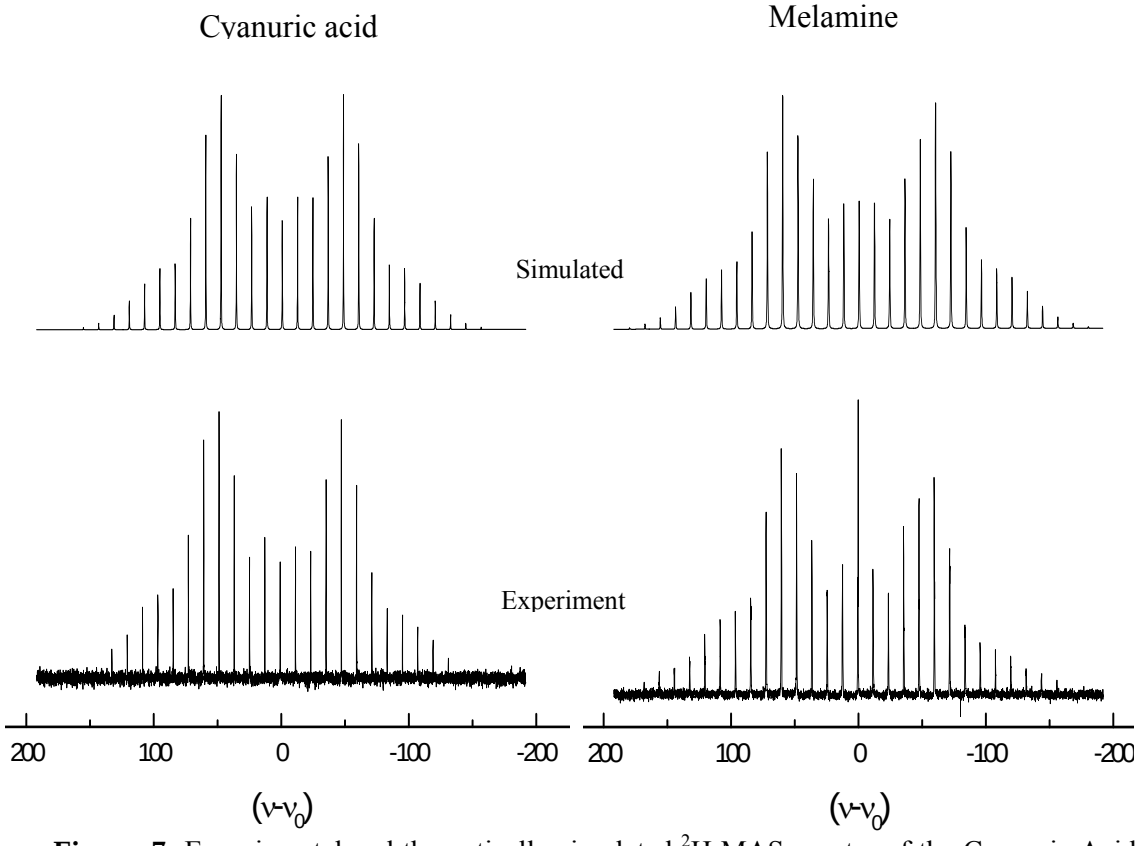

Figure–7: Experimental and theoretically simulated ^2H MAS spectra of the Cyanuric Acid and Melamine at 8 kHz.

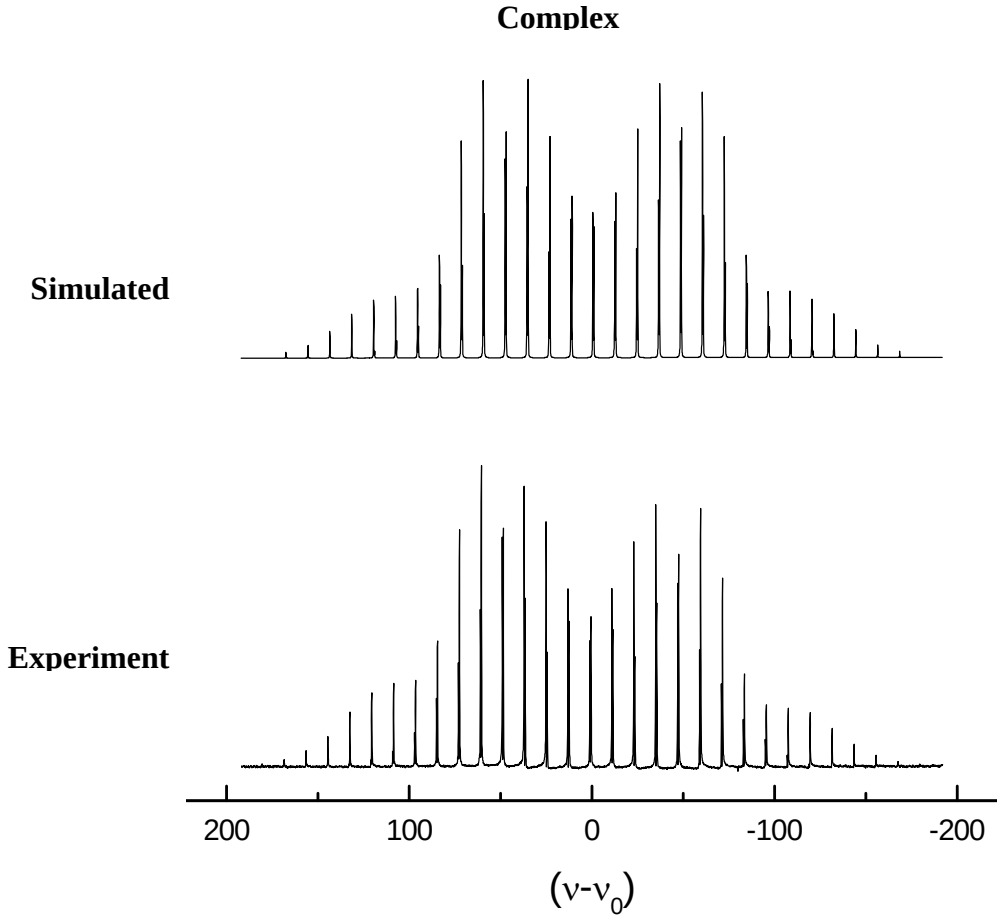

Figure – 8. Experimental and theoretically simulated ^{2}H MAS spectra of the Cyanuric Acid – Melamine (CA:MA) Complex at 8 kHz.

Table – 4

Results of the computer simulation of ^{2}H slow MAS spectra

System	^{2}H Simulation results	
	$e^{2}Qq/h$ ***(kHz)***	**η**
CYANURIC ACID	180.5	0.19
MELAMINE	200.1 200.1 213.5	0.23 0.14 0.21
1:1 CYANURIC ACID:MELAMINE	140.0 207.0	0.26 0.16

$e^{2}Qq/h$ and η denote the quadruple coupling constant and asymmetry parameter of the ^{2}H electric field gradient tensor, respectively.

2.3 *ab initio* Calculations of NMR Chemical Shifts

ab initio calculations of ^{13}C, ^{15}N and ^{2}H NMR chemical shielding tensors were carried out for Cyanuric Acid (CA), Melamine (MA) and the Cyanuric Acid – Melamine Complex (CA:MA). The *ab initio* calculation results were compared with the experimentally observed results and assignments of the NMR resonance positions were also made to the corresponding crystallographically nonequivalent sites. All the *ab initio* chemical shielding calculations were carried out using the Gaussian 98 program[18]. The chemical shielding tensors were calculated in the σ scale, using the convention $\sigma_{11} \leq \sigma_{22} \leq \sigma_{33}$. But the isotropic chemical shift values are given in the δ scale for the sake of comparison with the experimental values. The absolute shielding (σ) values obtained from all calculations were converted to chemical shifts (δ) relative to the absolute shielding of liquid TMS at room temperature of 184.1 ppm[19,20] such that,

$$\delta_{cal} = 184.1 - \sigma_{absolute}$$

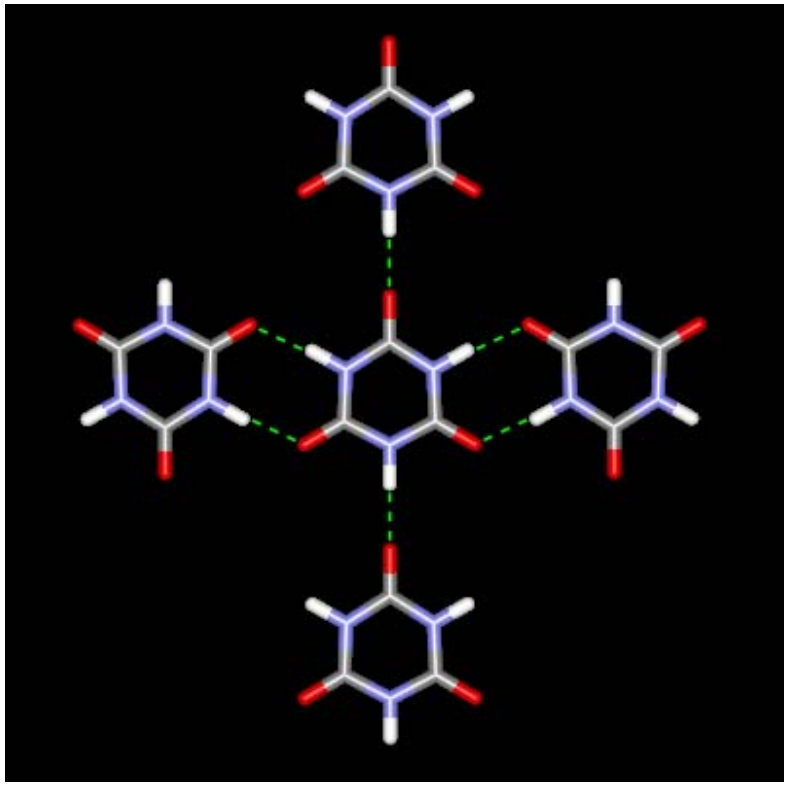

Figure – 9: Pentamer cluster of Cyanuric Acid used for chemical shielding calculations, generated from the crystal structure.

A cyanuric acid pentamer cluster was built from the crystal structure[7] as shown in Figure – 9. For this cluster, geometry optimization is not warranted since the local geometry of the cluster, including hydrogens, is already well determined by neutron diffraction. Hence, any attempt to do geometry optimize such a cluster built from neutron diffraction determined structure will result in alterations of the local geometry and would in turn adversely affect the chemical shielding determinations. The chemical shielding tensors were therefore calculated for the cyanuric acid pentamer without any geometry optimization. The calculations were done at the Hartree – Fock level with a considerably large (6-311++g(2d,2p) basis set. This basis set was chosen based on accuracy or quality of the basis set and the computational time requirement. The results are tabulated in Table – 5. Even though the experimental and the calculated chemical shifts do not match exactly, there is a very good correlation between the experimental and the calculated chemical shifts especially for ^{15}N and ^{2}H. The trend matches up well as can be seen from Table – 5.

Table – 5

Comparison of Experimental and Calculated isotropic chemical shifts of Cyanuric Acid and Melamine.

Cyanuric Acid			**Melamine**		
Atom	δ expt	δ cal	Atom	δ expt	δ cal
C1	149.0	156.7	C1	166.2	179.8
C2	151.3	161.0	C2	167.8	183.8
C3	151.3	161.1	C3	166.2	179.7
N4	134.3	137.7	N4	83.9	68.0
N5	135.7	139.4	N5	87.4	68.5
N6	135.7	139.4	N6	90.9	80.5
H10	10.5	11.3	N7	173.7	178.1
H11	12.0	12.6	N8	171.6	179.6
H12	12.0	12.6	N9	171.6	179.3
			H10	9.7	-1.1
			H11	to	2.2
			H12	5.6	1.0
			H13	Broad	2.8
			H14	Peak	2.5

A similar approach was used also for the Melamine molecule based on its crystal structure[8]. The pentamer model of Melamine built for the calculations is shown figure-10. Again, no geometry optimization is warranted since we have used the neutron diffraction data for building the cluster. The NMR chemical shielding tensors were calculated at the Hartree – Fock level using the (6-311++g(2d,2p) basis set. The results of the chemical shielding calculations are tabulated in Table – 5. Even though the same basis set and same approximations were used, the calculated chemical shielding values were not very close to the experimental values as noticed for Cyanuric acid. But there is an overall agreement between the experimental results and calculations when we consider the total chemical dispersion over the various ^{13}C, ^{15}N and ^{2}H resonances occur and their relative disposition in the observed chemical shift range. The ^{15}N chemical shift values of the NH_2 groups deviate the most. The reason could due to a possible disorder of NH_2 groups at room temperature[21]. Also the crystal structure and hydrogen-bonding network is complicated and gets perturbed with small changes in the method of crystallization. The calculated ^{1}H chemical shifts are in a range from –1.1 to 6.4 ppm, which cannot be assigned to the experimental spectra since we observe a broad resonance from 5.6 to 9.7 ppm.

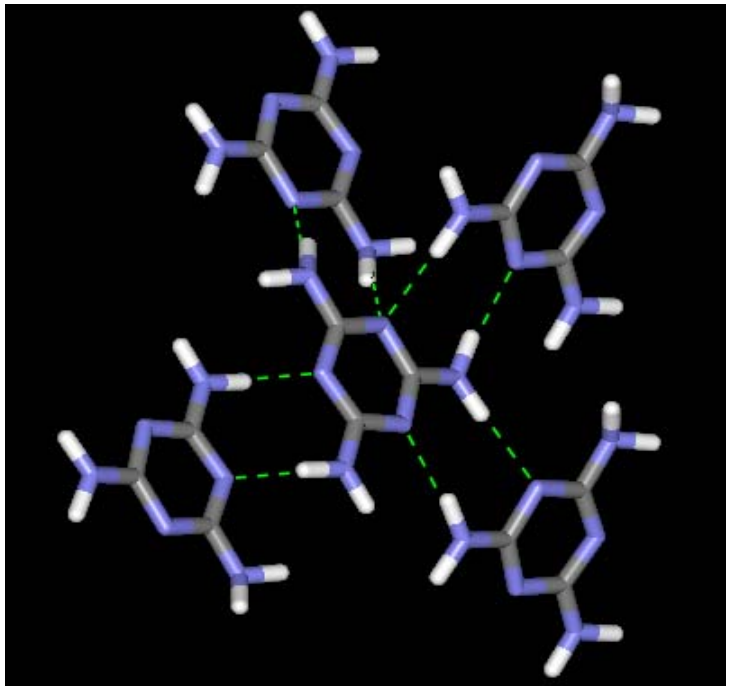

Figure – 10: Pentamer cluster of Melamine used for chemical shielding calculations, generated from the crystal structure.

To calculate the NMR parameters more reliably for Cyanuric acid and melamine in the CAMA complex, two tetramer models were generated form the crystal structure data[4] as shown in Figure – 11 and 12. (1) One Cyanuric acid at the center surrounded by three Melamine molecules, ($CAMA_3$). (2) One Melamine at the center surrounded by three Cyanuric Acid molecules, (CA_3MA).

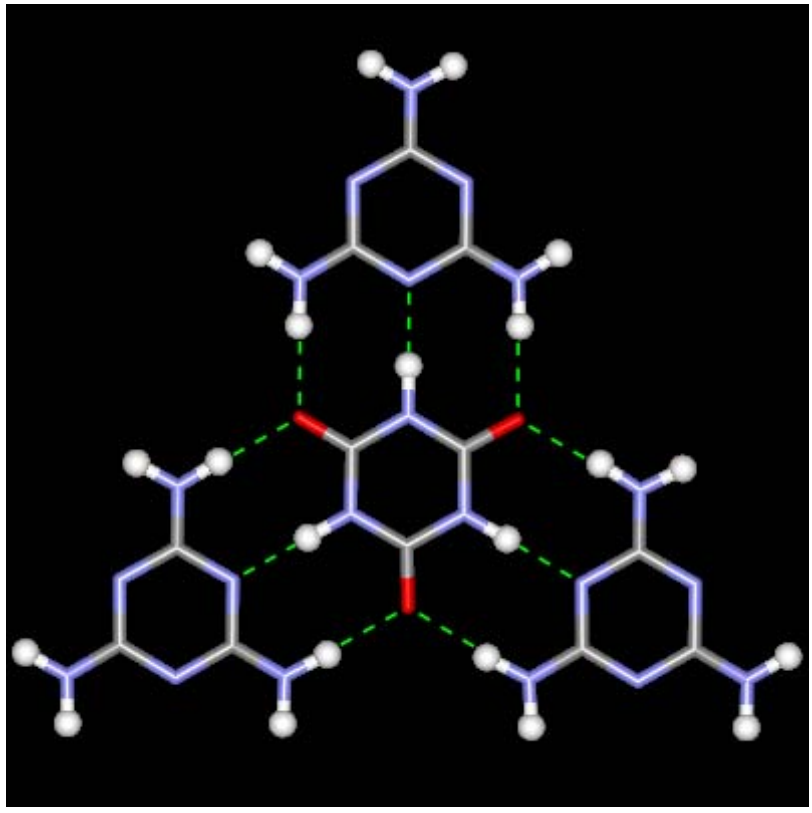

Figure – 11: Tetramer cluster of the Cyanuric acid Melamine Complex with CA at the center. ($CAMA_3$). The proton positions are showed as balls that were used for optimization.

These kinds of two tetramer models represent the CAMA complex better. Further, they ensure that the hydrogen bonding environment, implicated in the molecular self assembly of the self complementing CA and MA units, is well depicted and characterized before subjecting to *ab initio* calculations. Also it facilitates in reducing the computational time requirement tremendously compared to a single structure capable of representing both Cyanuric acid and Melamine of the complex with a similar approximation. The NMR parameter calculation is no longer straight forward as it was for Cyanuric Acid and Melamine alone, since the crystal structure data of CAMA

complex does not have the hydrogen coordinates. Hydrogen atoms were added manually to the ring nitrogen atoms of CA and to the amide nitrogen atoms of MA. Since hydrogen atoms were added manually, their coordinates will not be accurate and it will not be the most energetically favorable position. Hence a "hydrogen only" optimization was done. This is done by optimizing the hydrogen positions keeping all other atoms in the tetramer frozen as shown in Figure – 11 and 12. This optimization was done for both $CAMA_3$ and CA_3MA at the Hartree – Fock level with 6-311++g(d,p) basis set.

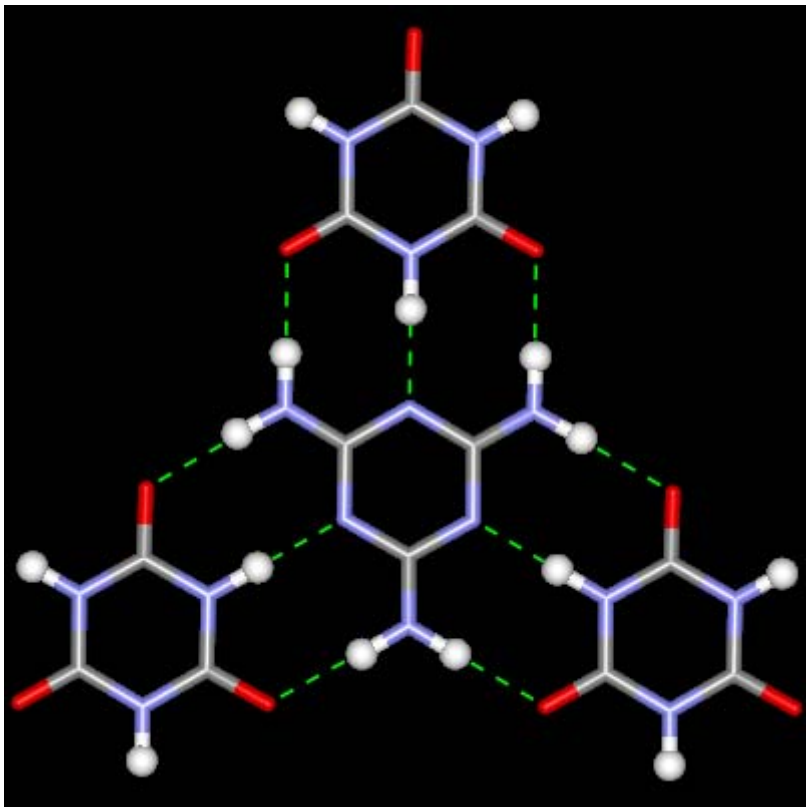

Figure – 12 Tetramer cluster of the Cyanuric acid Melamine Complex with MA at the center. (CA_3MA). The proton positions are showed as balls that were used for optimization.

^{13}C, ^{15}N and ^{2}H NMR chemical shielding tensors were calculated for the optimized $CAMA_3$ and CA_3MA clusters. The results are tabulated in Table – 6. For the $CAMA_3$ cluster, even though the calculated chemical shifts do not match very well with the experimental values in terms of absolute values, we do find an overall agreement between the experimental results and calculations when we consider the total chemical

dispersion over the various ^{13}C, ^{15}N and ^{2}H resonances of CA and MA occur and their relative disposition in the observed chemical shift range. It is interesting to note that the ^{15}N calculated chemical shift values for the amide nitrogen atoms of CA_3MA are very close to the experimental values. It is important to note that the x-ray data could not distinguish between the Cyanuric acid and Melamine rings since both have almost the same dimensions, which are arranged alternatively in the three dimensional structure. This resulted in not being able to differentiate the oxygen atoms of CA and the amide nitrogen atoms of MA. Hence it was not possible to identify the correct number of non equivalent atoms in the crystal structure. Therefore the X-ray data provides us with a total of two Carbon atoms, two ring Nitrogen atoms and two amide Nitrogen atoms for the CAMA complex. Whereas in the Solid state NMR data we observe four ring Carbon and four ring Nitrogen resonances, two corresponding to CA and two for MA. When the crystal structure data is modified in such a way that we can distinguish between the CA and MA rings, the *ab inito* calculation of NMR shieldings indeed gives a similar result to that of the experiment.

Table – 6

Comparison of Experimental and Calculated isotropic chemical shifts of Cyanuric Acid and Melamine from the $CAMA_3$ and CA_3MA tetramer clusters

CA of $CAMA_3$			**MA of CA_3MA**		
Atom	δ expt	δ cal	Atom	δ expt	δ cal
C1	154.0	180.8	C1	165.0	174.8
C2	154.0	180.8	C2	165.0	174.8
C3	153.0	174.3	C3	166.3	174.6
N4	140.1	152.8	N1	162.0	164.8
N5	139.1	148.6	N2	163.9	165.3
N6	139.1	148.6	N3	163.9	165.3
H10	13.8	16.9	N4	85.1	86.3
H11	14.9	17.0	N5	85.1	85.5
H12	14.9	17.0	N6	85.1	85.5
			H1	8.5	7.7
			H2		7.7
			H3	6.5	7.6
			H4		7.6
			H5		7.6
			H6		7.6

In Figure – 13, the calculated shielding values are graphically compared with the experimental values. As can be seen, the calculations show a good correlation with the experimental results for CA, MA and CA:MA. A hallmark of the *ab initio* calculation of NMR chemical shifts is that they lead to the unambiguous assignment of the ^{13}C, ^{15}N and ^{2}H resonances in the solid state NMR spectra to the crystallographic non equivalent atoms in the crystal structure.

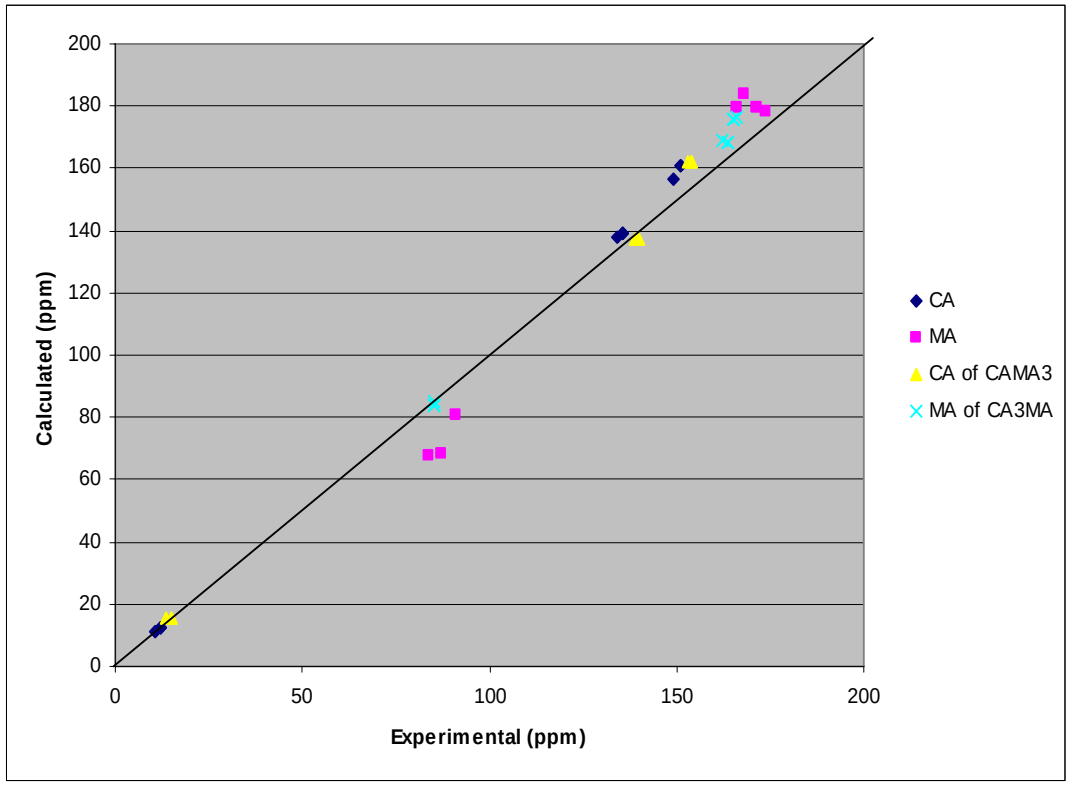

Figure – 13 Comparison of the Experimental and Calculated ^{2}H, ^{13}C and ^{15}N chemical shift values of CA, MA, CA_3MA and $CAMA_3$.

2.4 Conclusions

In conclusion, we have shown in this chapter that the determination of the isotropic ^{13}C, ^{15}N and ^{2}H chemical shieldings, both experimentally and theoretically, aids structural characterization in solid state NMR. A trinuclear solid state MAS/CP-MASNMR study, using naturally abundant (^{13}C, ^{15}N) and easily deuterated (^{2}H) nuclei, along with *ab initio* calculations of the chemical shielding tensors has been shown to provide the first opportunity to study hydrogen-bond-mediated assembly in

supramolecular systems that are not easily crystallizable. This has been demonstrated in the cyanuric acid-melamine (CA:MA) molecular system. The NMR approach establishes asymmetry imposed by the self-association in the monomers **CA** and **MA**, and the hydrogen bonding in the 1:1 **CA:MA** complex conforms to the supramolecular architecture[4] held by complementary hydrogen bonding. In the complex, the X-ray data does not unequivocally distinguish the two stacked rings because of their same size and shape, and this is alleviated by the solid-state NMR approach and confirmed both experimental and by *ab initio* calculations. Further, we have shown that theoretical calculations of the NMR shieldings and their comparison with experimental determinations aid in an unambiguous assignment of the resonances in the solid state NMR spectra to the various crystallographic nonequivalent atoms in the structure.

2.5 References:

1. (a) Lehn, J.-M. *Supramolecular Chemistry*; VCH: Weinheim, 1995. Jefferey, G. A.; Saenger, W. *Hydrogen Bonding in Biological Structures*; Springer: Berlin, 1991. (b) Simanet, E. E.; Xinhua, Li; Choi, I. S.; Whitesides, G. M. *Supramolecular Chemistry*; Alwood, J. L., Davie, J. E. D., Macnicol, D. D., Vogtle, F., Eds.; Pergamon Press: London, 1996; pp 595-621.
2. Terfort, A.; Bowden, N.; Whitesides G. M. *Nature* 1997, *386*, 162 and references therein.
3. Desiraju, G. R.; Steiner, T. Weak Hydrogen Bond. In *Structural Chemistry and Biology*; Oxford University Press: New York, 1999.
4. Ranganathan, A.; Pedireddi, V. R.; Rao, C. N. R. *J. Am. Chem. Soc*. 1999, *121*, 1752.
5. Brunner, E.; Stemberg, U. *Prog. Nucl. Magn. Res*. 1998, *32*, 21.
6. (a) Sanjayan, G. J.; Pedireddi; Ganesh, K. N. *Org. Lett.* 2000, *2*, 2825. (b) Pedireddi, V. R.; Ranganathan, A.; Ganesh, K. N. *Org. Lett*. 2001, *3*, 99.
7. Coppens, P.; Vos. A. *Acta Crystallogr*. 1971, *B27*, 146.
8. Vargheese, J.N.; O'Connell,M.; Maslen, E.N. *Acta. Crystallogr.* 1977, *B33*, 2102.

8a. Ganapathy.S.; Naito, A.; McDowell, C.A. *J. Am. Chem. Soc*. 1981, *103*, 6011.

9. Cromer, D. T., Larson, A. C. & Stewart, R. F. J. Chem. Phys. 1976, *65*, 336
10. Larsan, A. C.; Cramer, D. J. *J. Chem. Phys*. 1974, *60*, 185
11. Cousson, A.; Nicolai, B.; Fillaux, F. Acta Crystallographica, Section E: Structure Reports Online 2005, *E61*, o222.
12. Schaefer, J.; Stejskal, E. O. *J. Am. Chem. Soc*. 1976, *98*, 1031
13. Andrew, E. R.; Bradbury, A. R.; Eades, G. *Nature* 1958, *182*, 1659.
14. Webb, G. A. *Annual Reports on NMR Spectroscopy*; Academic Press: New York, 1986, p 149.
15. Benedict, H.; Limbach, H. H, Wehlan, M.; Fehlhammer, W.-P.; Golubev, N. S.; Janoschek, R. *J. Am. Chem. Soc*. 1998, *120*, 2939.
16. Mayumi, W.; Hiromu, S.; Hideo, I.; Yoshimasa, K.; Masatune, K. *Eur. J. Biochem.* 1981, *117*, 553.
17. Yu Kio, H.; Keiler, E. A.; Brown, T. L. *J. Magn. Res*. 1986, *67*, 202.
18. Gaussian 98, M. J. Frisch, G. W. Trucks, H. B. Schlegel, G. E. Scuseria, M. A. Robb, J. R. Cheeseman, V. G. Zakrzewski, J. A. Montgomery, Jr., R. E. Stratmann, J. C. Burant, S. Dapprich, J. M. Millam, A. D. Daniels, K. N. Kudin, M. C. Strain, O. Farkas, J. Tomasi, V. Barone, M. Cossi, R. Cammi, B. Mennucci, C. Pomelli, C. Adamo, S. Clifford, J. Ochterski, G. A. Petersson, P. Y. Ayala, Q. Cui, K. Morokuma, D. K. Malick, A. D. Rabuck, K. Raghavachari, J. B. Foresman, J. Cioslowski, J. V. Ortiz, A. G. Baboul, B. B. Stefanov, G. Liu, A. Liashenko, P. Piskorz, I. Komaromi, R. Gomperts, R. L. Martin, D. J. Fox, T. Keith, M. A. Al-Laham, C. Y. Peng, A. Nanayakkara, C. Gonzalez, M. Challacombe, P. M. W. Gill, B. Johnson, W. Chen, M. W. Wong, J. L. Andres, C. Gonzalez, M. Head-Gordon, E. S. Replogle, and J. A. Pople, Gaussian, Inc., Pittsburgh PA, 1998.
19. Jameson, A. K; Jameson, C. J; Chem. Phys. Lett. 1987, **134**, 461.
20. Birn, J.; Poon A.; Ramamoorthy A.; J. Am. Chem. Soc. 2004, *126*, 8529
21. Meier, R. J; Coussens, B.; J Mol Struct Theochem 1990, **209**, 303

Chapter III

^{27}Al Electric Field Gradients and Chemical Shieldings and Structural Characterization of Aluminum Hydroxide Polymorphs

Part of this chapter has been published in,
Triple-quantum magic angle spinning ^{27}Al NMR of aluminum hydroxides.
Journal of the American Chemical Society (2002), 124(13), 3200-3201.

3.1 Introduction

This chapter deals with the determination of the ^{27}Al isotropic chemical shielding and the electric field gradient parameters, both experimentally and theoretically, as aids in the complete solid state NMR characterization of aluminum hydroxide polymorphs. This also represents the first such attempt to study three basic aluminum hydroxide polymorphs, namely, gibbsite, bayerite and boehmite, by ^{27}Al triple quantum (3Q) MAS NMR for the identification of the nonequivalent aluminum environments in each of the polymorphs and their unequivocal assignments to the structure. The ^{27}Al isotropic chemical shifts and the electric field gradient parameters, namely, the quadrupole coupling constant ($C_Q = e^2Qq/h$) and the asymmetry parameter (η), were determined from experiments by graphical analysis of 2D 3Q-MAS spectra and computer simulations of the experimental 1D MAS spectra. These were also determined theoretically by *ab initio* calculations. Assignments of the crystallographic nonequivalent aluminum sites in gibbsite and bayerite were made possible by comparison of the experimental results with *ab initio* calculations.

The third most common element in earth's crust is aluminum and in nature there exist four of the five known crystalline forms of hydroxides, namely, the two trihydroxides gibbsite and nordstrandite and the two oxyhydroxides boehmite and diaspore[1]. Although the other aluminum hydroxide, bayerite (β–$Al(OH)_3$) does not occur freely in nature, it can be prepared synthetically, as are the two other most widely used members of the family, gibbsite (α– $Al(OH)_3$) and boehmite (α–AlOOH). For the other two members, namely nordstrandite and diaspore, no commercial use or large-scale synthesis has been reported. Irreversible dehydration of aluminum hydroxides polymorphs produces a series of so-called 'transition' aluminas in a well-defined dehydration sequence[2a], resulting in α–Al_2O_3 as the end member. This is shown in Figure – 1. Their thermal decomposition under controlled synthetic condition produce alumina derived materials of desired morphology and texture. Thus, at the heart of industrial aluminas and ceramics lie these three starting materials of great fundamental importance.

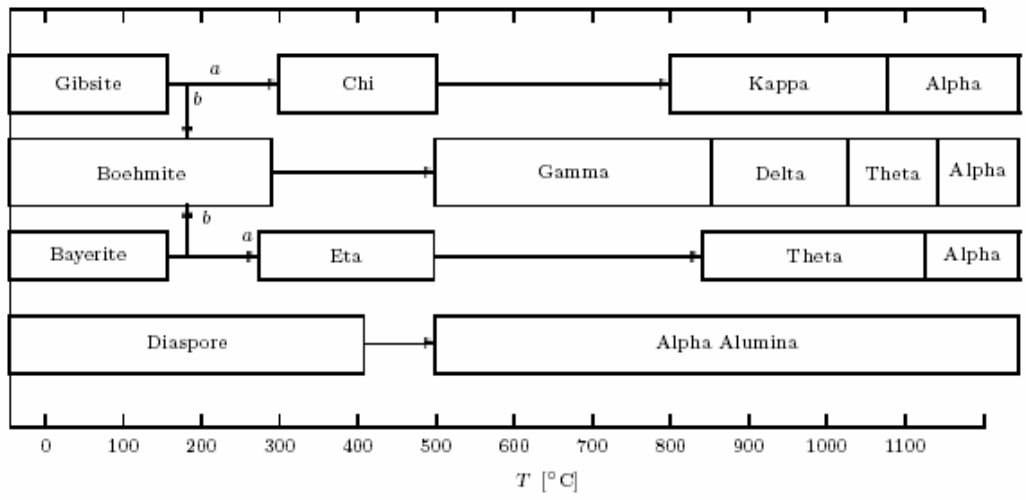

Figure 1: Dehydration sequences of aluminum hydroxide polymorphs in air, showing their transformation to different phases of 'transition' alumina, with the end material being 'alpha alumina' (α–Al_2O_3). Enclosed areas indicate the range of stability. Open area indicates range of transition. Path **b** is favored by moisture alkalinity, and coarse particle size (100 μm); path **a** by fine crystal size (below 10 μm). From reference 2b.

Aluminum hydroxides are different configurations of the same structure, the building block of which is the "Pauling Octahedra", where the octahedra are formed by Al-O and Al-H bonds that impart stability to the compact structure. For the three important members, namely, Gibbsite, Bayerite and Boehmite, the structural arrangement of the aluminum octahedral are shown in Figure 2. The corresponding crystal structure data are compiled in Table. 1.

As an adjunct to X-ray diffraction, high-resolution solid state NMR is sought to differentiate between various crystalline configurations. ^{27}Al MAS-NMR is often used to distinguish Al in different coordinations (tetra, penta, octahedral). ^{27}Al MAS is of no avail in the structural characterization of aluminum hydroxides since these basic materials have all the Al environments in only the six-fold coordination (Al^{VI}) and the crystallographic nonequivalence among the chemically similar, yet structurally different, Al^{VI} sites within the given coordination (octahedral) remain undetected. This is due to the insufficient spectral resolution, emanating from residual second order quadrupolar broadening not altogether eliminated by MAS in the 'central transition' (-½,½) dominated ^{27}Al spectra[3]. Consequently, it is not possible to distinguish the nonequivalent sites and study minor structural modifications involving small variations

in the coordination geometry, as would occur in basic aluminum hydroxides and the thermally decomposed alumina forms.

The recent advent of Multiple Quantum Magic Angle Spinning (MQ-MAS) NMR[4,5] alleviates this problem. As explained in detail in chapter – 1, this experiment exploits the definite correlation of the orientation dependent frequencies, evolving during the multiple quantum (3Q, 5Q for ^{27}Al) evolution period (t_1), with the corresponding single quantum (-½,½) frequencies in the acquisition period (t_2). ^{27}Al isotropic spectra, devoid of second order quadrupolar broadenings are obtained after a shearing[5] operation of MQ-MAS data and they now facilitate inspection of nonequivalent Al environments within a given Al coordination. Further benefits of a high detection sensitivity ensue due to high ^{27}Al natural abundance (100%). In this chapter it is shown that MQ-MAS offers new opportunities in the identification of Al environments in basic synthetic aluminum hydroxides, as a prelude to phase identification and quantification in various structurally transformed materials.

Table – 1

Crystal Structure Data for Aluminum Hydroxides

System	Molecular Symmetry	Crystal Symmetry	Number of inequivalent Aluminium Sites
Gibbsite	Monoclinic	$C2_1/c$	2
Bayerite	Monoclinic	$C2_1/n$	2
Boehmite	Orthorhombic	Cmcm	1

(a)

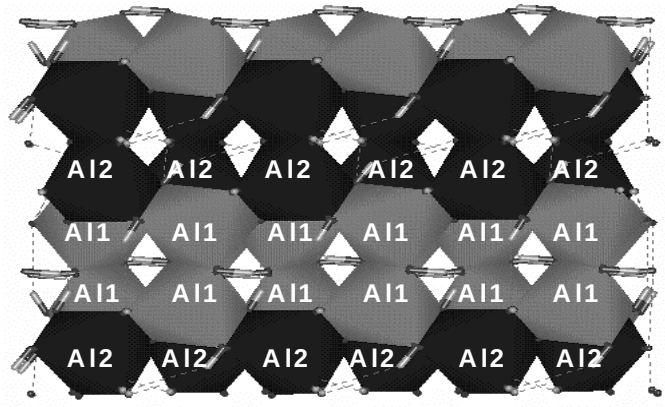

(b)

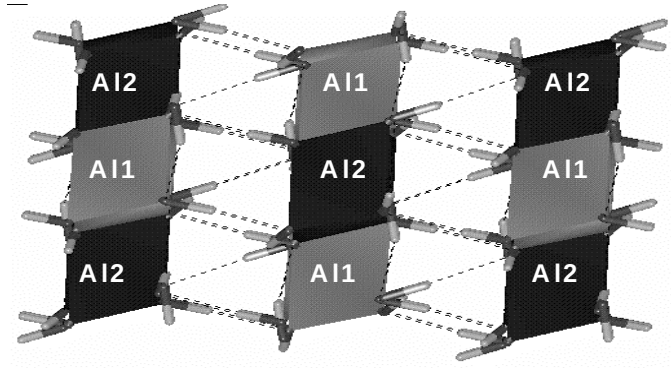

(c)

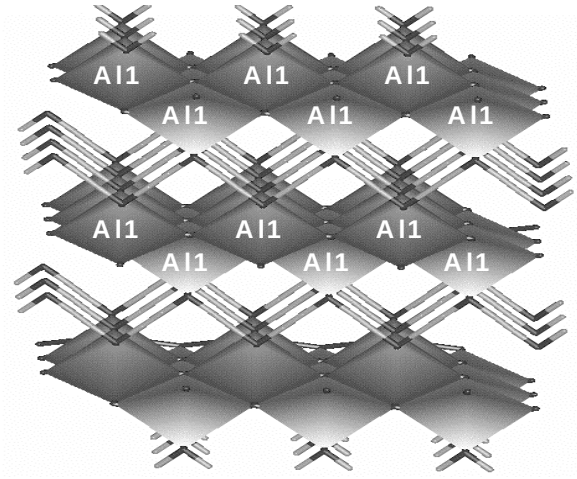

Figure–1: Crystal Structure of the three aluminum hydroxide polymorphs.(a) Gibbsite, (b) Bayerite and (c) Boehmite. In each case, the aluminum environment is octahedral and the two crystallographic nonequivalent Al^{VI} sites in Gibbsite and Bayerite are denoted as Al1 and Al2 and the lone Al^{VI} site in Bohmite is denoted as Al1. The $Al(OH)_6$ octahedra form an edge-shared layered arragement as shown and the difference in the stacking arragement causes the crystallographic nonequivalence for the Al^{VI} sites.

3.2 Solid State NMR

3.2.1 Experimental Conditions:

All the Solid State NMR experiments were performed on a 11.7 T Bruker Avance 500 NMR spectrometer at ambient probe temperature (297-299 K). The NMR experiments were performed using a Bruker double resonance CPMAS probe at ^{1}H and ^{27}Al frequency of 500.13 and 130.31 MHz, respectively. For ^{27}Al MAS experiments, the ^{27}Al r.f. pulse length was chosen to be very short, namely, 0.6 μ s, taking into account the nutation behavior[6] of the quadrupolar spins. The ^{27}Al MAS and 3QMAS spectra were collected at a spinning speed of 13 kHz. The 3QMAS spectra were obtained using the three-pulse MQMAS sequence incorporating the z-filter[7] with rotor synchronization during the evolution period (t_1) and ^{1}H decoupling during the evolution and acquisition (t_2) periods using TPPM[8], as shown in Fig. 2. The t_1 rotor synchronization ensured the absence of spinning side bands along the isotropic dimension and eased signal identification and quantification, besides improving the S/N. For the 2D experiment, 64 t_1 increments were used and 480 transients were accumulated with a 1 sec recycle delay.

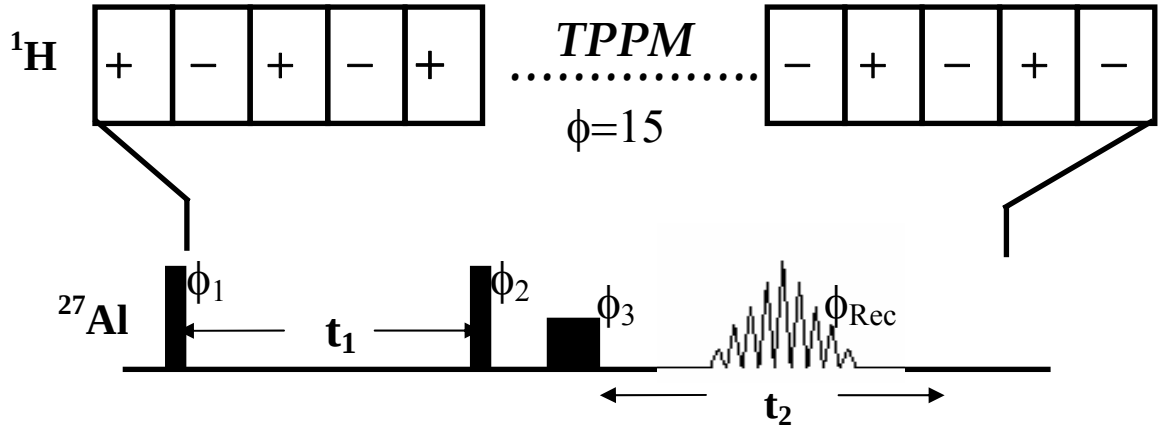

Figure – 2: Three-pulse z-filter sequence used for ^{27}Al 3QMAS experiments on gibbsite, bayerite and boehmite. An experimentally optimized TPPM decoupling on the ^{1}H channel was used to enhance the ^{27}Al signal resolution on the isotropic dimension. The following phase cycling was employed: $\phi_1 = 0$; : $\phi_2 = 0, 60, 120, 180, 240, 300$; : $\phi_3 = 0, 90, 180, 270$; : $\phi_{Rec} = 0, 240, 120, 0, 240, 120, 90, 330, 210, 90, 330, 210, 180, 60, 300, 180, 60, 300, 270, 150, 30, 270, 150, 30$. For the hypercomplex 2D experiment, the first pulse was shifted by 30^0 between successive experiments.

For the r.f. field used (υ_{rf} = 60 kHz), the first and second pulses were individually optimized to give maximum efficiencies for the 0Q → ±3Q coherence creation and the ±3Q → 0Q conversion steps, respectively. The last conversion step (0Q → -1Q) to the observed (-1/2 ↔ +1/2) central transition was achieved using a soft 'central transition selective' 90° pulse of duration 9 μs. The phase-sensitive 2D experiments were conducted using the hypercomplex States[9] procedure, for which the phase of the first r.f. pulse was shifted by 30° between successive experiments. The advantage and description of the MQMAS sequences are explained in detail in chapter – 1. The 1024x1024 2D data matrix was apodized using an exponential (LB=10 Hz) (gibbsite and boehmite) or sine squared bell (SSB=8) (bayerite) window functions along t_1 prior to Fourier transformation and shearing. This gave pure absorption mode spectra in which the isotropic spectra were obtained by a sum projection of the 2D data onto the δ_{iso} axis. The ^{27}Al chemical shift values are referenced with respect to $[Al(OH)_6]^{3+}$.

3.2.2 ^{27}Al MAS/3Q-MAS of Aluminum Hydroxide Polymorphs

Figure 3 shows the Bloch decay ^{27}Al MAS spectra of Gibbsite, Bayerite and Boehmite taken under ^{1}H decoupling. Under optimized experimental conditions, the 'central' (+1/2 ↔ -1/2) (CT) and the 'satellite' (±5/2 ↔ ±3/2, ±3/2 ↔ ±1/2) (ST) transitions are fully recouped over a MHz spectral range, with profound spinning side bands appearing in the spectra due to the first order averaging of the orientation dependent broadening of the ST. The ST side bands show that the aluminum environments are held in the crystal rigidly and there is no motional averaging of the aluminum electric field gradient tensors. The ^{27}Al MAS spectra, displaying the CT and ST, can thus be simulated and analyzed for the extraction of the chemical shifts and electric field gradient parameters and directly compared with the theoretical results obtained from *ab initio* calculations, also carried out on a rigid molecular cluster using the X-ray determined structure.

The first inspection of the ^{27}Al MAS spectra presented in Fig. 3 precludes any identification about the crystallographic multiplicity of the octahedral aluminum environments to be made. As discussed later, ^{27}Al MAS spectra were mainly used as additional aid in computer simulations and parameter estimation.

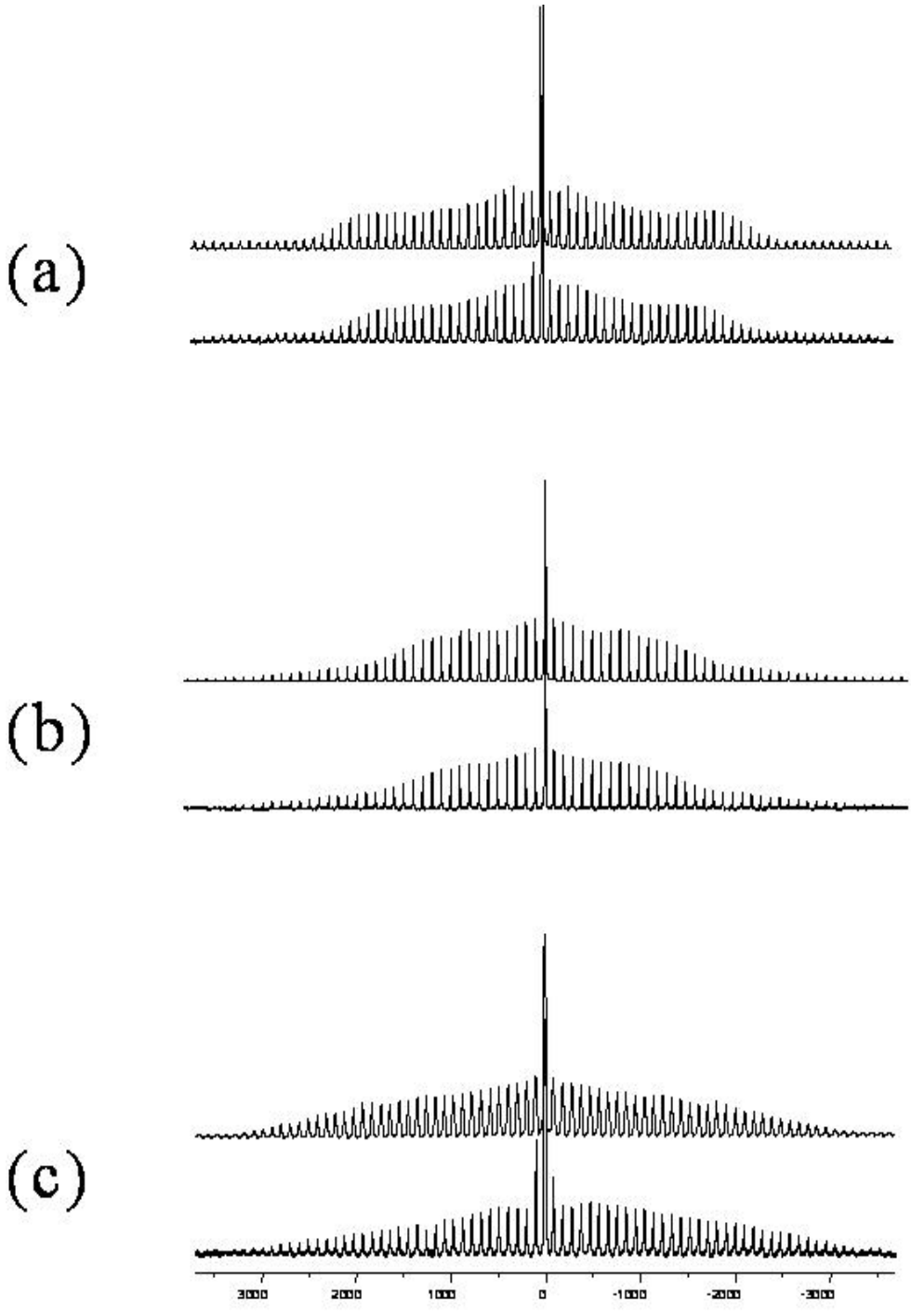

Figure – 3: ^{27}Al MAS spectra of (a) Gibbsite, (b) Bayerite and (c) Boehmite showing intense middle signal due to 'central' transition and the spinning side band manifold due to 'satellite' transition. In each pair of spectra, the bottom spectrum corresponds to the experimentally obtained data and the top spectrum is the corresponding simulation.

Figure 4 shows the ^{27}Al 3Q-MAS NMR spectra of gibbsite taken without and with ^{1}H decoupling. As seen, efficient ^{1}H decoupling is warranted in the 3QMAS experiment for the clear identification of nonequivalent aluminum sites in gibbsite. An inspection of the isotropic spectra (**d**, **f**), obtained after a shearing of the 2D 3QMAS data, shows that ^{1}H decoupling places stringent demands on the isotropic dimension (ω_1) than in the MAS dimension (ω_2), making it impossible to detect any multiplicity of the aluminum environments in the absence of ^{1}H decoupling. ^{1}H decoupled ^{27}Al 3QMAS spectra of the other two aluminum hydroxide polymorphs, namely, bayerite and boehmite, are compared with gibbsite as shown in Fig. 5 (**a**, **b**, **c**).

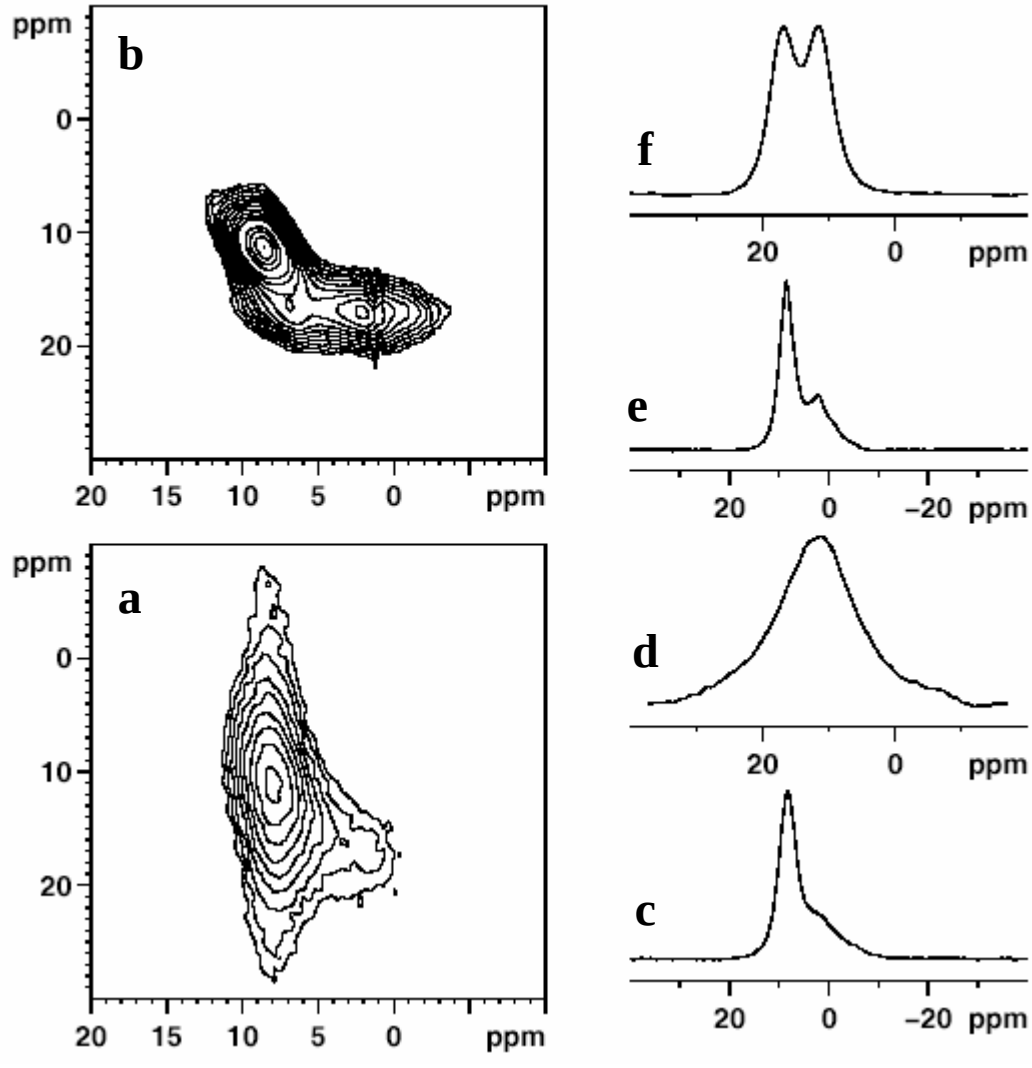

Figure – 4: ^{27}Al 3QMAS spectra (left) of gibbsite taken without (**a**) and with (**b**) ^{1}H decoupling and the corresponding isotropic (ω_2) (**c**, **e**) and MAS (ω_1) (**d**, **f**) projections.

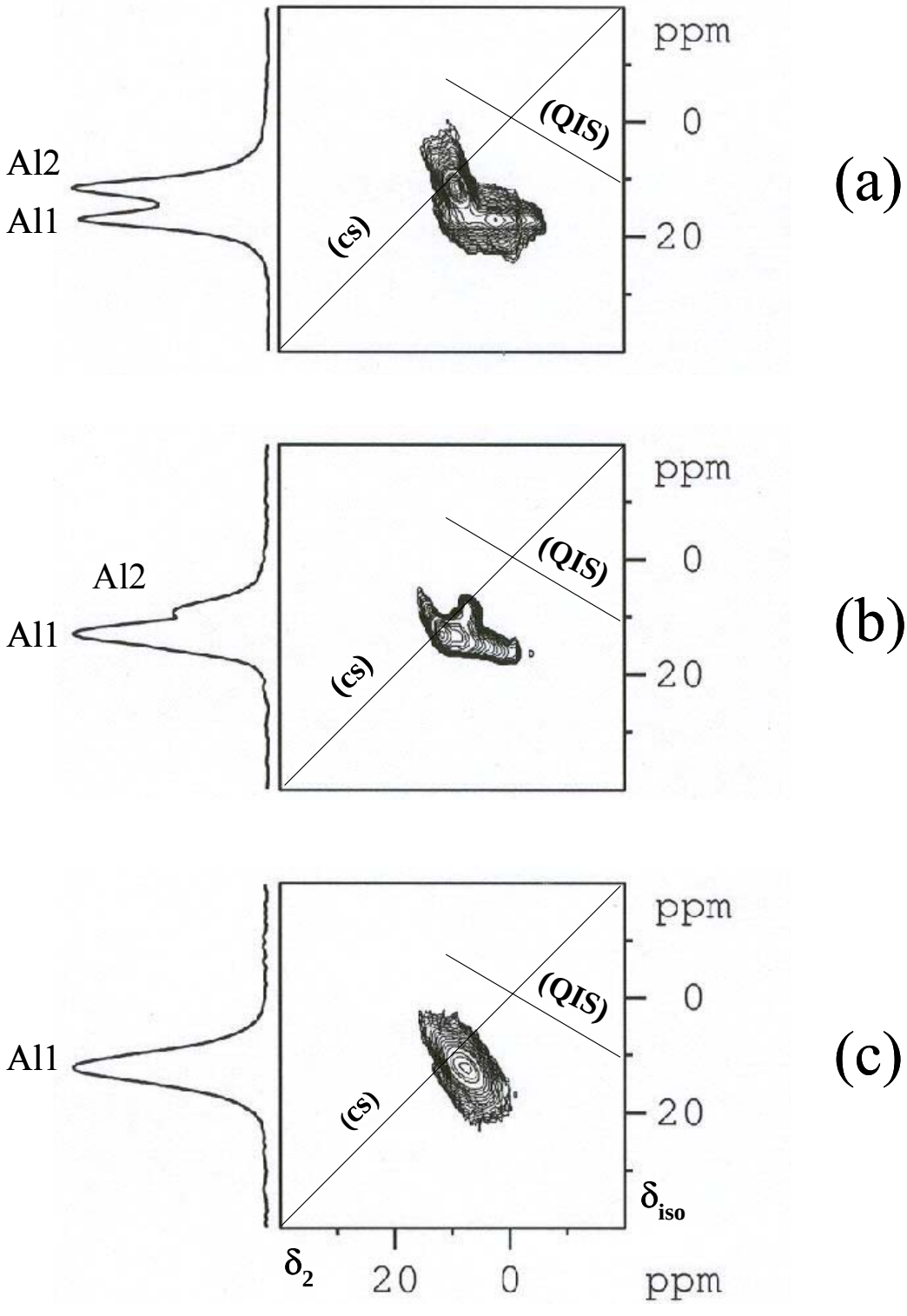

Figure – 5: 2D contour plots of ^{27}Al triple quantum MAS NMR experiments (^{1}H decoupled) of (**a**) Gibbsite, (**b**) Bayerite and (**c**) Boehmite. The assignments of ^{27}Al isotropic peaks appearing along ω_{iso} axis are shown. The δ_{cs} (slope 1) and δ_{QIS} (slope –10/17) directions are marked in the 2D contour plot and these aid in the graphical analysis of the 3Q-MAS data.

The results presented in Figs. 4 and 5 clearly depict the presence of nonequivalent octahedral aluminum in the structure, with an enhanced resolution of the isotropic signals in gibbsite than in bayerite. Further to the distinction of the nonequivalent octahedral aluminum sites revealed by 3Q-MAS, the spectra provide valuable data on the chemical shielding and electric field gradient parameters to further aid in the structural distinction and characterization. In gibbsite[10,11] and bayerite, consistent with their structures (Fig. 1), we detect two ^{27}Al isotropic resonances with a 1:1 intensity from triple quantum experiments. The intensity ratio of 1:1 for the two nonequivalent octahedral Al environments was verified in the 2D data processed without resolution enhancement, followed by spectral deconvolution. The 3QMAS results lead to the deduction of chemical shift (δ_{CS}) and quadrupole (P_Q) parameters for gibbsite and bayerite. In order to determine the electric field gradient parameters, namely, the quadrupole coupling constant $C_Q = e^2qQ/h$) and the asymmetry parameter (η), one has to either do computer simulations of the 2D contour plots or use a judicious combination of MQ-MAS graphical analysis and 1D MAS simulation.

The 2D spectra shown have been plotted with "normalized" δ_2 and δ_{ISO} ppm scales[12] so that the chemical shift (CS) axis (δ_{CS}) lies along a slope of unity, whereas the quadrupole induced shift (QIS) direction has a slope of -10/17. For each aluminum species, the projection of the center of gravity of the corresponding contour onto these axes yields the values for the chemical (δ_{CS}) and quadrupole induced (δ_{QIS}) shifts. From the latter, the second-order quadrupole parameter is calculated as,

$$P_Q = C_Q(1-\eta^2/3)^{1/2} = (\upsilon_0/300)\,(15\,\delta_{QIS})^{1/2}$$

where υ_0 is the Larmor frequency. Thus, with the knowledge about the number of sites, the graphical analysis[13] of 3QMAS spectra yields the values for δ_{CS} and P_Q for each of the resolved aluminum sites. Since the parameter P_Q determined by graphical analysis contains both C_Q and η, 1D simulations of the MAS spectra were carried out to determine η. The computer simulations of the 1D MAS spectra are shown in Fig. 3. In the case of gibbsite, the increased site resolution for the aluminum environments, allows

the corresponding ω_2 CT MAS spectra to be extracted from the sheared 2D date set at the isotropic peak maxima. These, as well as the corresponding computer simulations of the CT MAS spectra are shown in Figure 6 and this led to an accurate estimate of η_Q in the case of gibbsite. Besides yielding the values of η_Q, the MAS simulations further confirm the 1:1 intensity ratio for the two nonequivalent aluminum sites in gibbsite and bayerite, in good agreement with their structure. It may be noted that one of the aluminum sites is characterized by a large C_Q value. Despite the relatively large quadrupole interaction, this site is equally well excited as the other Al site so that (0Q $\rightarrow \pm$ 3Q) creation and ($\pm$3Q $\rightarrow$ 0Q) conversion efficiencies are nearly equal. These are supported by density matrix calculations[16,17] using δ_{cs} and P_Q values determined by graphical analysis and ν_{rf} (60 kHz) used in the experiment. The results of the density matrix calculations and their experimental comparison are shown in Figure 7. Values of all the experimentally determined parameters are included in Table- 2.

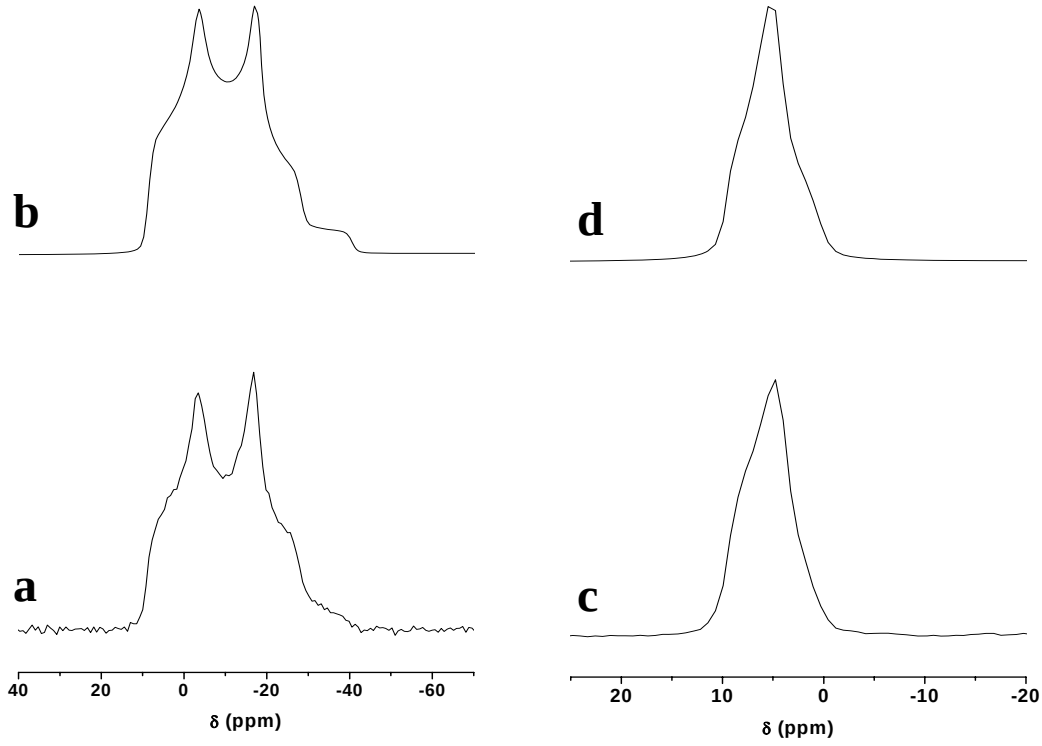

Figure – 6: CT MAS spectra extracted from the sheared 3QMAS data set of gibbsite for the two resolved aluminum sites Al1 (**a**) and Al2 (**c**). The corresponding computer simulated spectra, using best fit parameters (Table 2) are shown in (**b**) and (**d**), respectively.

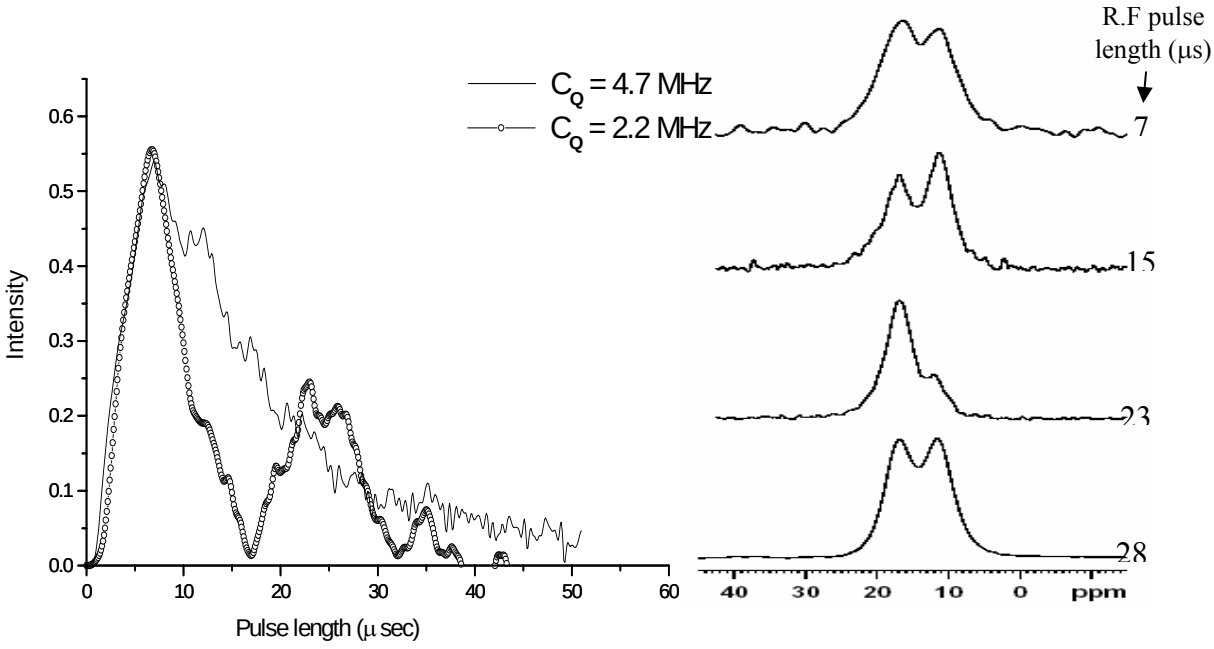

Figure – 7: Density Matrix calculation for the triple quantum excitation in Gibbsite. 3Q excitation curves were calculated, as a function of the length of the preparation pulse P1, using ν_{RF} = 60 kHz, for the two nonequivalent aluminum sites in gibbsite with e^2Qq/h = 4.7 MHz (Al 1) and 2.2 MHz (Al 2). Spectra on the right denote the isotropic projections obtained from sheared 2D 3QMAS data collected using the R.F pulse length as indicated against each spectrum.

Table 2

^{27}Al Chemical Shift and Quadrupole Interaction Parameters of Aluminum Hydroxides

Aluminum Hydroxide	δ_{iso} (ppm)	δ_{cs}	$(e^2qQ/h)^1$ MHz	$\eta_Q{}^1$	Assign-ment
Gibbsite[2]	11.6	10.5 ± 0.2 [10.47 ± 0.05]	2.2 ± 0.2 (2.2, 2.6) [1.93 ± 0.01]	0.75 ± 0.05 [0.74 ± 0.01]	Al (2)
	17.2	11.5 ± 0.2 [12.01 ± 0.05]	4.7 ± 0.2 (3.2, 3.9) [4.53 ± 0.01]	1.00 ± 0.05 [0.43 ± 0.01]	Al (1)
Bayerite	9.1	8.3 ± 0.2	1.9 ± 0.1 (2.5, 3.0)	0.25 ± 0.05	Al (2)
	13.1	12.4 ± 0.2	1.4 ± 0.1 (1.4, 1.6)	0.80 ± 0.05	Al (1)
Boehmite	12.6	11.0 ± 0.5	1.8-2.8	0.5-1.0	Al (1)

[1]$(e^2qQ/h) = P_Q(1+\eta^2_Q/3)^{-1/2}$ (P_Q from graphical analysis). η_Q determined by simulation of 1D MAS spectra. For boehmite, 1D MAS simulation required a distribution of e^2qQ/h and η_Q values in the range indicated. Values in parenthesis are the e^2qQ/h determined from *ab initio* calculations using small (HF/6-31g(d.p)) and large (HF/6-311++g(2d.2p)) basis sets. Errors in the experimentally determined values of δ_{iso} e^2qQ/h and η_Q were estimated from analysis of 1D MAS spectra. [2]Values in the square brackets denote the 'best fit' data obtained from simulation of CT MAS spectra of gibbsite

3.3 *ab initio* Calculations of ^{27}Al Quadrupole Interaction Parameters

3Q-MAS experiments reveal the presence of two nonequivalent aluminum sites in gibbsite and bayerite, consistent with the presence of two crystallographic nonequivalent octahedral aluminums in their structures. The formidable exercise is to make unique assignment of the two isotropic signals in the 3QMAS spectra to the two X-ray determined[14,15] nonequivalent octahedral aluminum sites which build the stacked layers in the respective aluminum hydroxide polymorphs, gibbsite and bayerite. The two crystallographic inequivalent aluminums, present in gibbsite and bayerite, build layers of edge sharing $Al(OH)_6$ octahedra (called A and B), to produce the stacked layer sequence AB BA AB . . . (gibbsite)[14] and AB AB AB . . . (bayerite)[15] (Figure – 1). In bayerite, hydroxyl groups of one layer lie in the depressions between the hydroxyls in the second, while in gibbsite, the hydroxyls of the adjacent layers are situated directly opposite each other, causing the layers to be displaced along *a*-axis.

Indeed, the difference in the stacking sequence show striking dissimilarity in the way chemical shielding and quadrupole interaction parameters are affected for the two octahedral aluminum sites in gibbsite and bayerite. This is evident from the experimentally determined values for the chemical shift and quadrupole interaction parameters (Table 2). In gibbsite, the two Al sites show a larger difference in P_Q than in δ_{cs}. In bayerite, this is reversed. In fact, the enhanced peak resolution for the isotropic resonances in gibbsite is due to a large positive quadrupole induced shift for one of the sites (Al2) along the sheared isotropic dimension.

While trying to assign the isotropic resonances obtained from o the inequivalent octahedra in the structure, we find that correlations[18,19] based on (T-O-T)/(O-T-O) with δ_{cs}/ P_Q do not lead to unambiguous assignments for the isotropic resonances since the large difference in e^2qQ/h (2.5 MHz) (gibbsite) or δcs (~4 ppm) (bayerite) is not accounted for by the smaller differences in octahedral distortion derived from an analysis of O-T-O or T-O-T angles. For signal assignments, independent *ab initio* calculations of electric field gradient tensors, were carried out for gibbsite and bayerite using different basis sets and clusters (tetramer, decamer) built from crystal structure data.[14,15] The tetramer cluster for both the Al sites in Bayerite and Gibbsite are shown in

Figures 8 and 9, respectively. The T-O-T bond angles and Aluminum sites are labeled. In this model, the central AlO_6 octahedra, for which the EFG and shielding tensors are calculated, is surrounded by three other AlO_6 octahedra as in the crystal structure. This kind of a tetrameric cluster is commonly used in literature as a good approximation for *ab initio* calculations involving zeolites.

All calculations were performed at the Hartree – Fock level with different basis sets. Among the three common ab initio methods (Hartree-Fock, MP2 and DFT), HF, with the choice of a large basis set as used in this chapter, is a well accepted level, in terms of numerical accuracy and computational speed for the calculations of chemical shielding and electric field gradient tensors. The chemical shielding tensors were calculated with two basis sets; 6-31g(d,p) and 6-311++g(d,p) using the Gaussian98 program[20]. Higher basis sets than these were not used for chemical shielding calculations due to limitations in computational power. Whereas, EFG tensor calculations were done with a higher basis set and also with a larger cluster using the GAMESS program[21]. The reason being, Chemical shielding calculation takes lot more computational time than required for EFG calculations. The chemical shielding tensors were calculated in the σ scale with $\sigma_{11} \leq \sigma_{22} \leq \sigma_{33}$. But the isotropic chemical shift values are given in the δ scale for the sake of comparison with the experimental values. The absolute shielding (σ) values obtained from all calculations were converted to chemical shifts (δ) relative to the absolute shielding of $Al^{3+}.(H_2O)_6$ such that,

$$\delta_{iso} = \sigma_{iso}^{REF} - (1/3)\mathrm{Tr}\,(\boldsymbol{\sigma})$$

Isotropic chemical shielding value of σ_{iso}^{REF} = 633 ppm and 612 ppm are used for calculations with basis sets 6-31G(d,p) and 6-311++G(d,p) respectively. Tr ($\boldsymbol{\sigma}$) is the trace of the chemical shielding tensor obtained for the aluminum hydroxide clusters.

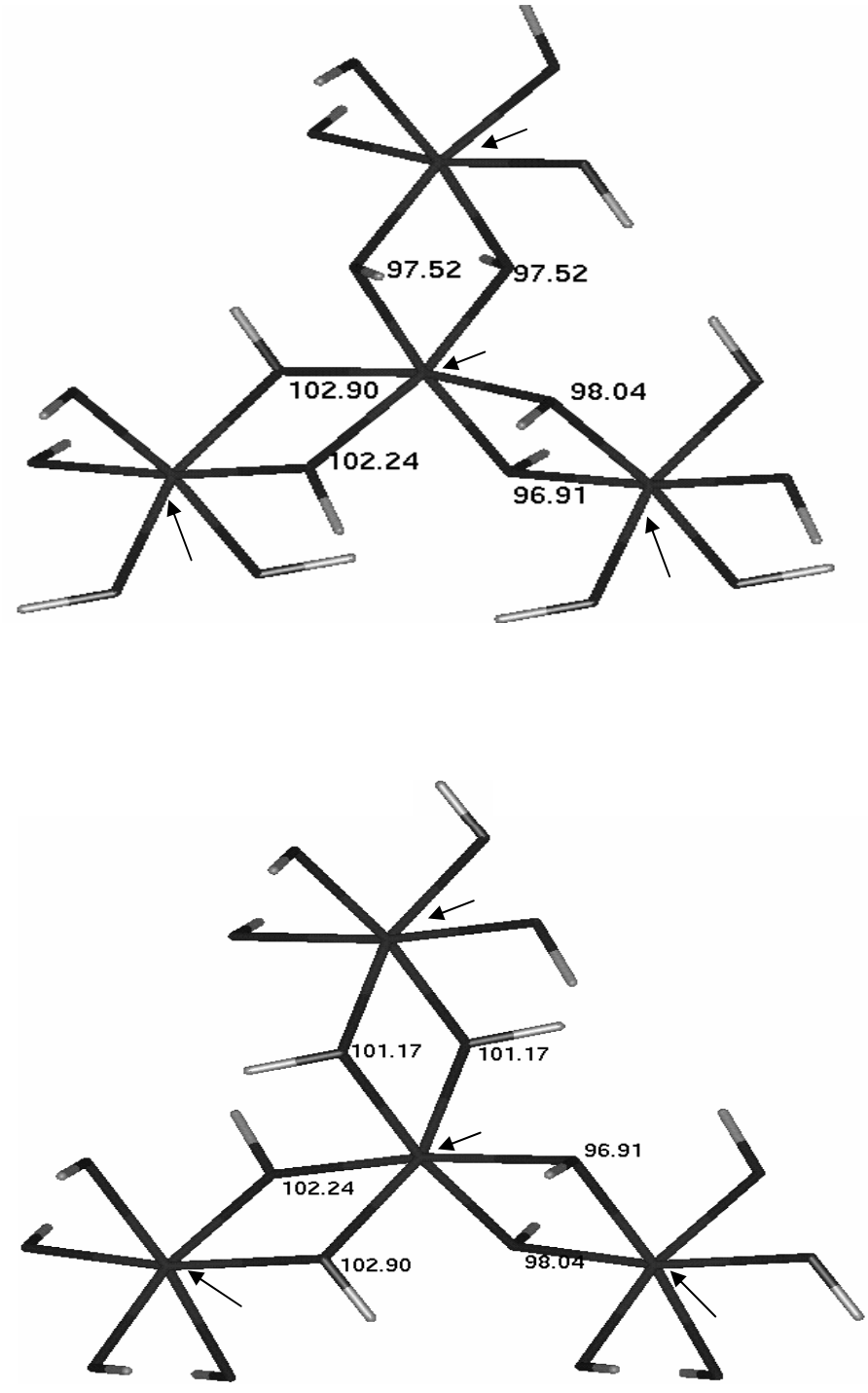

Figure – 8: Tetrameric Clusters of Bayerite used for ab initio EFG and chemical Shielding Tensor calculations. ^{27}Al Site – 1 (Top) and Site – 2 (bottom)

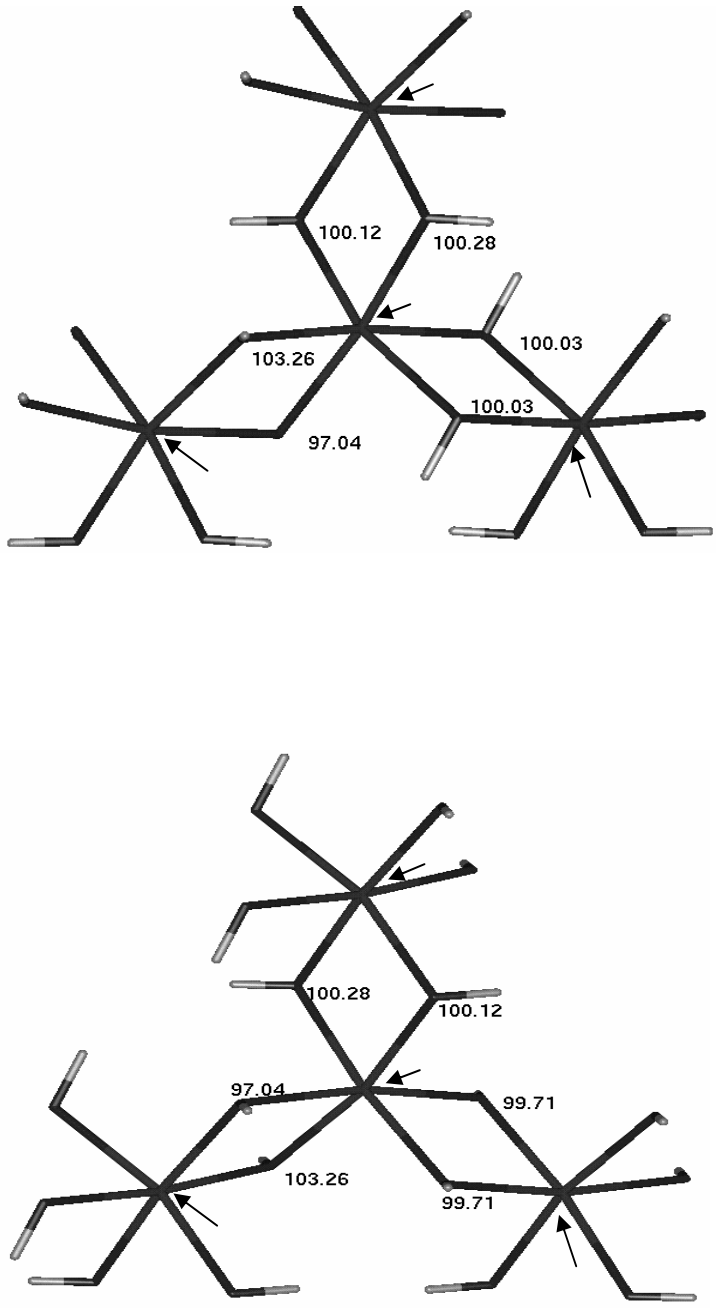

Figure – 9: Tetrameric Clusters of Gibbsite used for ab initio EFG and chemical Shielding Tensor calculations. ^{27}Al Site – 1 (Top) and Site – 2 (bottom)

The Chemical Shielding Tensor (σ ppm) in Principal Axis System calculated at the Hartree- Fock level with a 6-311++G(d, p) basis set for a tetrameric cluster of Bayerite and Gibbsite are as follows:

Bayerite (Tetrameric Cluster) — Isotropic Chemical Shift

Al 1

$$\begin{pmatrix} 581.886 & 0.000 & 0.000 \\ 0.000 & 595.558 & 0.000 \\ 0.000 & 0.000 & 598.107 \end{pmatrix}$$

20.1 ppm

Al 2

$$\begin{pmatrix} 583.860 & 0.000 & 0.000 \\ 0.000 & 594.605 & 0.000 \\ 0.000 & 0.000 & 599.538 \end{pmatrix}$$

19.3 ppm

Gibbsite (Tetrameric Cluster)

Al 1

$$\begin{pmatrix} 585.425 & 0.000 & 0.000 \\ 0.000 & 595.971 & 0.000 \\ 0.000 & 0.000 & 601.848 \end{pmatrix}$$

17.6 ppm

Al 2

$$\begin{pmatrix} 586.372 & 0.000 & 0.000 \\ 0.000 & 600.190 & 0.000 \\ 0.000 & 0.000 & 606.835 \end{pmatrix}$$

14.2 ppm

The results of the chemical shielding tensors are tabulated in Table – 3. For Gibbsite and Bayerite, the chemical shift values do not change much with 6-31G(d,p) and 6-311++G(d,p) basis sets. However, it is observed that the calculations show a good trend which is consistent with the basis sets.

Table – 3

Isotropic Chemical Shift values of Aluminum Hydroxides from *ab initio* Calculation of Tetrameric Clusters.

Basis Set	Bayerite (ppm)		Gibbsite (ppm)	
	Al 1	Al 2	Al 1	Al 2
6-31g(d,p)	19.8	18.6	16.8	14.0
6-311++g(d,p)	20.1	19.3	17.6	14.2

The same tetrameric aluminum hydroxide clusters, as shown in Figure 8 and 9, were used in the *ab initio* calculations of ^{27}Al electric field gradient tensors. The EFG tensor elements are calculated in atomic units (au) by the Gaussian98 program. Using a recently determined[22] value of 146.6 x 10^{-31} m^2 for the quadrupole moment (eQ) of ^{27}Al, the quadrupole coupling constant (e^2Qq/h) was calculated using the formula:

$$e^2Qq/h\ (MHz) = 0.234965Q(millibarn) \times q_{11}\ (au)$$

As for the chemical shift calculations, EFG tensor was also calculated with different basis sets. The results are tabulated in Table – 4. The electric field gradient tensor in the Cartesian and the principal axis frame calculated at the Hartree- Fock level with a 6-311++G(2d, 2p) basis set for tetrameric clusters of Bayerite and Gibbsite are as follows:

EFG tensor in Cartesian Frame **Principal Axis System**

Bayerite (Tetrameric Cluster)

Al 1

$$\begin{pmatrix} -0.028696 & 0.018521 & 0.020094 \\ 0.018521 & 0.037357 & 0.007381 \\ 0.020094 & 0.007381 & -0.008660 \end{pmatrix} \qquad \begin{pmatrix} -0.0430 & 0.0000 & 0.0000 \\ 0.0000 & -0.0022 & 0.0000 \\ 0.0000 & 0.0000 & 0.0452 \end{pmatrix}$$

Al 2

$$\begin{pmatrix} 0.042992 & 0.011256 & 0.068261 \\ 0.011256 & -0.011684 & 0.021634 \\ 0.068261 & 0.021634 & -0.031308 \end{pmatrix} \qquad \begin{pmatrix} -0.0746 & 0.0000 & 0.0000 \\ 0.0000 & -0.0133 & 0.0000 \\ 0.0000 & 0.0000 & 0.0879 \end{pmatrix}$$

Gibbsite (Tetrameric Cluster)

Al 1

$$\begin{pmatrix} 0.062779 & 0.018964 & -0.081599 \\ 0.018964 & -0.030349 & -0.016925 \\ -0.081599 & -0.016925 & -0.032430 \end{pmatrix} \qquad \begin{pmatrix} -0.0799 & 0.0000 & 0.0000 \\ 0.0000 & -0.0341 & 0.0000 \\ 0.0000 & 0.0000 & 0.1139 \end{pmatrix}$$

Al 2

$$\begin{pmatrix} 0.045596 & 0.027903 & 0.017842 \\ 0.027903 & -0.024321 & 0.065785 \\ 0.017842 & 0.065785 & -0.021276 \end{pmatrix} \qquad \begin{pmatrix} -0.0890 & 0.0000 & 0.0000 \\ 0.0000 & 0.0123 & 0.0000 \\ 0.0000 & 0.0000 & 0.0768 \end{pmatrix}$$

The trend in the quadrupolar coupling constant (QCC) values for Al1 and Al2 sites in Gibbsite and Bayerite are perfectly reproduced with different basis sets. Since the computational time required for calculating EFG is much less than required for chemical shielding calculation, it was possible to calculate EFG at many different basis sets. Also similar to basis set variation, it was also possible to calculate EFG for a larger

aluminum hydroxide cluster to check for the trends in the QCC value for Al1 and Al2 sites. A decamer cluster, which is a cluster containing seven AlO_6 units was built from the crystal structure for Gibbsite and Bayerite as shown in Figure 10. Normally for quantum chemical calculations the computational time requirement increases almost exponentially with a linear increase in the number of atoms. Hence a decamer cluster will require extremely long time compared to the time taken by a tetramer for a given basis set. This was overcome by using a locally dense basis set. For the decamer clusters a large basis set (6-311++G(3d, 3p)) was used for the atoms within the triangle (see Figure 10). For the remaining atoms a smaller basis set (3-21g) was used for the EFG calculations. The EFG calculations with different basis sets and different cluster sizes indeed show convergence of electric field gradient tensors and support that the signal assignments can be made with confidence.

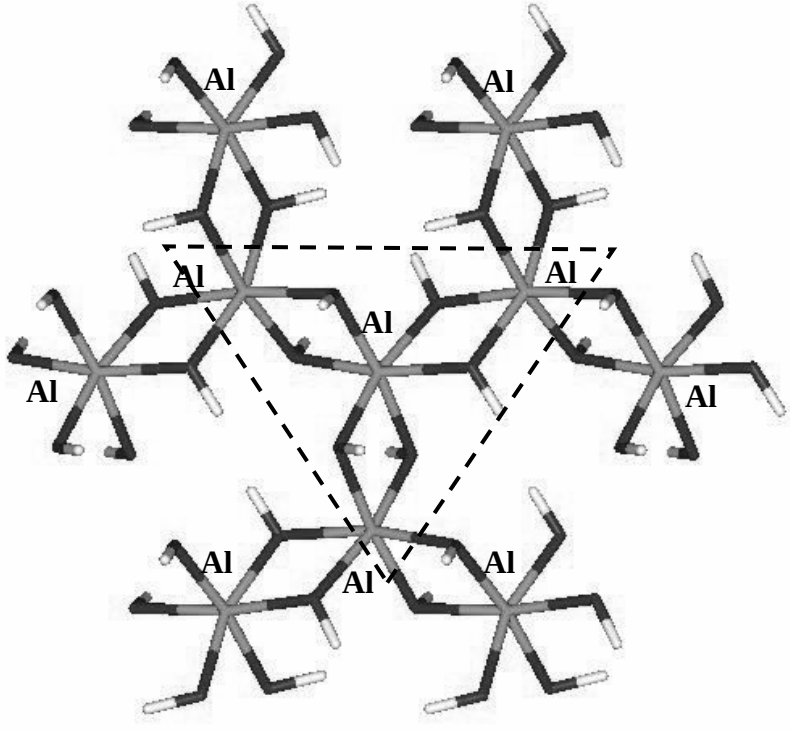

Figure – 10 : Decamer cluster of Bayerite centered on Al1 site used for EFG calculations

Table – 4: Basis set dependence of Quadrupolar Coupling Constant.

Basis Set	Bayerite QCC/ (MHz)		Gibbsite QCC/ (MHz)	
(Tetramer)	Al 1	Al 2	Al 1	Al 2
6-31g(d,p)	1.42	2.50	3.17	2.15
6-31g(2d,2p)	1.54	2.61	3.45	2.07
6-31g(3d,3p)	1.66	2.76	3.60	2.27
6-311++g(d,p)	1.45	2.99	3.85	2.63
6-311++g(2d,2p)	1.56	3.03	3.92	2.64
Larger cluster (Decamer)				
Central part 6-311++g(3d,3p) Outer part 3-21g	1.47	2.21	3.37	2.77

The *ab initio* calculations show that the theoretically calculated values of QCC are very close to that of the experimental results. However, the calculated values of η for the two sites in bayerite are 0.58 for site 1 and 0.25 for site 2. The relative values are in contrast with the experimental data, this discrepancy is due to the fact that, for η the three diagonal components of the EFG are involved in its definition [$\eta = (q_{xx} - q_{yy})/q_{zz}$]. Each of them is a very small difference between two large numbers, the electronic and the nuclear contribution. Therefore, a change of only a few percent in any of these large numbers will automatically generate a larger uncertainty in the calculated values of η. This problem is particularly severe when q_{yy} and q_{xx} are very close, because

a minute fractional shift in one of them automatically generates a large variation in η. As seen from the definition of η, variations in q_{zz} also contribute to its change but in a lesser degree than the two other components. Consequently, unless each of the q_{ii}'s is computed to an extremely high accuracy, η will possess much larger uncertainties than QCC which only contains the single tensor element ($QCC=e^2Qq_{zz}/h$). This requirement has been suggested to be the main reason in most papers dealing with EFG calculations only QCC is reported[23]. Numerical accuracy in the calculated values of q_{xx},q_{yy} and q_{zz} tensor elements can be further improved by (1) using a more extensive basis set (like triple zeta valence with two polarized set of diffuse functions) ; (2) including electron correlation (perturbation (MPn), CI (singles and doubles)and Coupled Cluster (singles and doubles) approaches) and (3) using geometry optimized or accurately determined (by neutron diffraction) hydrogen atom positions. However, such calculations aimed to estimate η with increased precision are computationally formidable for us to undertake at the present time. We feel that the calculations we have carried out represent an acceptable compromise between precision and speed and are tractable on larger systems such as Gibbsite and Bayerite.

We have therefore made the signal assignments based on the calculated values of e^2qQ/h which are more reliable than η_Q[24,25], after ensuring that the calculated values of e^2qQ/h show convergence and a trend analogous to that noticed in the experimentally determined values of e^2qQ/h (Table 1). This leads to the unambiguous assignment of the two nonequivalent octahedra in the structures of gibbsite and bayerite and is shown in Figure 1.

The oxyhydroxide polymorph boehmite (AlOOH) displays a single but broad (~5 ppm) isotropic resonance. In the structure of boehmite, equivalent aluminum octahedra are formed by coordination of Al to nonequivalent oxygens[26] and these octahedra are set out in straight double chains to build a sheet like structure (Fig. 1-A) linked through hydrogen bonds between hydroxyls in neighboring planes. The lack of high resolution may be traced to disorder in Al positions in the crystal[27,28], leading to small variation in the isotropic chemical shift and quadrupolar couplings. The larger line width for the isotropic signal of boehmite is entirely consistent with the somewhat poor

crystallinity observed in XRD pattern. The elongation of the 2D contour parallel to the QIS direction shows that the observed broadening is dictated by a distribution of quadrupole couplings and to a smaller degree by chemical shift dispersion. Boehmite is known to exhibit a distribution of water content and crystallite size.[29]

3.4 Conclusions

In conclusion, we have shown in this chapter that the determination of the ^{27}Al isotropic chemical shieldings and the electric field gradient parameters, both experimentally and theoretically, aids in the structural characterization in solid state NMR. A solid state MAS/3QMASNMR study, along with *ab initio* calculations of the chemical shielding and EFG tensors, is shown to provide the first opportunity to structurally characterize the basic aluminum hydroxide polymorphs which lie at the root of all the transition aluminas and ceramics. This has been demonstrated in the three aluminum hydroxide polymorphs, namely, gibbsite, bayerite and boehmite. The structural distinction of the aluminum hydroxide polymorphs has been made through identification, quantification and unambiguous assignment of the structure building octahedral aluminum environments, by a combination of ^{27}Al 3Q-MAS experiments, 1D MAS spectral simulations and *ab initio* quantum chemical calculations. The experimental and theoretical approaches presented are in general applicable for structural elucidation using solid state NMR.

3.5 References:

1. "Alumina as a ceramic material", Ed. W.H. Gitzen American Ceramic Society, Ohio, USA), **1970**.
2. (a) Wefers, K; Misra, C. *Alcoa Technical Paper No. 19*, **1987**, Alcoa Laboratories, Pittsburg, PA, USA.
   (b). *Alumina as a Ceramic Material*, edited by W. H. Gitzen (The American Ceramic Society, Ohio, U.S.A, 1970).
3. Freude D., Encyclopedia of Analytical Chemistry, R.A. Meyers (Ed.), **2000**, 12188-12224.
4. Frydman L.; Harwood J.S. *J. Am. Chem. Soc.* **1995**, *117*, 5367-5368.

5. Medek, A.; Harwood J.S.; Frydman L. *J. Am. Chem. Soc.* **1995**, *117*, 12779-12787.
6. Samoson, A.; Lippmaa, E. Phys. Rev. B, 1983, 28, 6567.
7. Amoureux,J. P.; Fernandez, C.; Steuernagel, S. *J. Magn. Reson. A,* **1996**, *123*, 116.
8. Bennet A. E.; Rienstra C. M.; Auger M.; Lakshmi K. V.; Griffin R. G. *J. Chem. Phys.* **1995**, *103*, 6951.
9. States, D.; Haberkorn, R.; Ruben, D. J. Magn. Resonance 1982, 48, 286-292.
10. Ashbrook S. E.; McManus J.; Mackenzie K. J. D.; Wimperis S. *J. Phys. Chem. B* **2000**, *104*, 6408.
11. McManus J.; Ashbrook S. E.; Mackenzie K. J. D.; Wimperis S. *J. Non-Cryst. Solids* **2001**, *282*, 278-290.
12. Amoureux, J. P.; Fernandez, C. Solid State NMR. 1998, 10, 211
13. Fernandez C.; Amoureux J. P.; Chezeau J. M.; Delmotte L.; Kessler H. *Microporous Materials,* **1996**, *6*, 331.
14. Saalfeld H.; Wedde M. *Z. Kristallogr.* **1974**, *139*, 129-135.
15. Zigan F.; Joswig W.; Burger N. *Z. Kristallogr.* **1978**, *148*, 255-273.
16. Amoureux J. P.; Fernandez C.; Dumazy Y. *J. Chim. Phys*. **1995**, *2*, 1939.
17. Bak, M; Rasmussen, T; Nielsen, N. Chr. *J. Magn. Reson.* **2000**, *147*, 296-330.
18. Delaye J. M.; Charpentier T.; Petit J. C.; Ghaleb D.; Faucon P. *Chem. Phys. Lett*. **2000**, *320*, 681.
19. Hunger H.; Horvath T. *J. Am. Chem. Soc*. **1996**, *118*, 12302.
20. Gaussian 98, Revision A.9, M. J. Frisch, G. W. Trucks, H. B. Schlegel, G. E. Scuseria, M. A. Robb, J. R. Cheeseman, V. G. Zakrzewski, J. A. Montgomery, Jr., R. E. Stratmann, J. C. Burant, S. Dapprich, J. M. Millam, A. D. Daniels, K. N. Kudin, M. C. Strain, O. Farkas, J. Tomasi, V. Barone, M. Cossi, R. Cammi, B. Mennucci, C. Pomelli, C. Adamo, S. Clifford, J. Ochterski, G. A. Petersson, P. Y. Ayala, Q. Cui, K. Morokuma, D. K. Malick, A. D. Rabuck, K. Raghavachari, J. B. Foresman, J. Cioslowski, J. V. Ortiz, A. G. Baboul, B. B. Stefanov, G. Liu, A. Liashenko, P. Piskorz, I. Komaromi, R. Gomperts, R. L. Martin, D. J. Fox, T. Keith, M. A. Al-Laham, C. Y. Peng, A. Nanayakkara, M. Challacombe, P. M. W. Gill, B. Johnson, W. Chen, M. W. Wong, J. L. Andres, C. Gonzalez, M. Head-Gordon, E. S. Replogle, and J. A. Pople, Gaussian, Inc., Pittsburgh PA, 1998.

21. "General Atomic and Molecular Electronic Structure System" M.W.Schmidt, K.K.Baldridge, J.A.Boatz, S.T.Elbert, M.S.Gordon, J.H.Jensen, S.Koseki, N.Matsunaga, K.A.Nguyen, S.J.Su, T.L.Windus, M.Dupuis, J.A.Montgomery. *J.Comput.Chem.* **1993**, *14*, 1347.
22. Vladimir Kellö, Andrzej J. Sadlej, Pekka Pyykkö, Dage Sundholm and Maria Tokman,; *Chem. Phys. Lett.,***1999**, *304*, 414.
23. Latonsinska, J. N.; Koput, J.; Phys.Chem.Chem.Phys., 2000, **2**, 145.
24. Torrent M. ; Musaev D.G.; Morokuma K. *J. Phys. Chem. B* **1999***, 103,* 8618-8627.
25. Murgich, J.; Aray, Y.; Soscum, H. J.; Marino, R. A. *J. Phys. Chem.* **1992**, *96,* 9198.
26. Walter T. H; Oldfield E. *J. Phys. Chem.* **1989**, *93*, 6744.
27. Hill R. J. *Clays and Clay Minerals,* **1981**, *29*, 435-445.
28. Tettenhorst R.; Hofmann D. A.*Clays and Clay Minerals* **1980**, *28*, 373-380.
29. Papee D.; Tertian R.; Biais, R. *Bull. Soc. Chim. Fr. Mem. Ser.* **1958**, *5*, 1301-1310.

CHAPTER IV

^{27}Al Electric Field Gradients and Chemical Shieldings and Structural Transformation of Aluminophosphate Molecular Sieves.

Part of this chapter has been published in,
Effects of hydration on $AlPO_4$-14 and $AlPO_4$-18 structures: ^{31}P MAS and ^{27}Al 3Q-MAS NMR study.
Studies in Surface Science and Catalysis (2001), 135(Zeolites and Mesoporous Materials at the Dawn of the 21st Century), 2098-2104

4.1. Introduction

This chapter deals with the determination of the ^{31}P and ^{27}Al isotropic chemical shielding and ^{27}Al electric field gradient parameters, both experimentally and theoretically, as aids in the complete solid state NMR characterization of the phosphorus and aluminum framework environments in aluminophosphate molecular sieves which undergo structural transformations when subjected to dehydration, calcinations and rehydration. Consistent with the main objective of determining spatially dependent interaction tensors using novel methods of solid state NMR, we have employed ^{31}P MAS and ^{27}Al MAS/3Q-MAS experiments, combined with *ab initio* calculations, to study the structural characteristics of the phosphorus and aluminum sites and the structural transformations occurring in two well-known aluminophosphates, $AlPO_4$-14 and $AlPO_4$-18. The change in aluminum coordination during the structural transformation is fully depicted by the ^{27}Al MAS/3Q MAS experiments and a complete structural characterization provided by the determination of chemical shift and electric field gradient parameters for the nonequivalent aluminum environments. The ^{27}Al isotropic chemical shifts and the electric field gradient parameters, namely, the quadrupole coupling constant ($C_Q = e^2Qq/h$) and the asymmetry parameter (η), were determined from experiments by graphical analysis of 2D 3Q-MAS spectra and computer simulations of the experimental 1D MAS spectra. The experimental determination of the ^{31}P and ^{27}Al chemical shifts and the ^{27}Al EFG parameters was carried out in the as-synthesized, calcined and rehydrated forms of $AlPO_4$-14 and $AlPO_4$-18. In each of these materials, the number of nonequivalent phosphorus T-sites could be determined and assigned. The assignment strategy followed the structure based correlation of the isotropic shift with mean T-O-T angle, which is a measure of the tetrahedral distortion at the given phosphorus site. In a similar way, the nonequivalent aluminum sites, existing in different coordinations (Al^{IV}, Al^{V} and Al^{VI}) in the as-synthesized and rehydrated $AlPO_4$-14 and $AlPO_4$-18 could be identified by ^{27}Al triple quantum experiments and structurally characterized by ^{27}Al 3Q-MAS data analysis and ^{27}Al 1D MAS spectral simulations. In the case of calcined $AlPO_4$-14, for which the dispersion in chemical shifts and quadrupole couplings is large, *ab initio* calculations

provide unambiguous assignments of the crystallographic nonequivalent aluminum sites by comparison with experimental results.

Small pore aluminophosphates with chabazite structures are excellent catalysts for the conversion of methanol to olefins[1, 2]. Recent reports suggest that Co and Mn substituted $AlPO_4$ – 18 structures are active for selective functionalization of linear alkanes[3]. Selective functionalization or for that matter partial oxidation of low molecular weight linear alkanes such as n-hexane was found to be difficult to achieve till recently. As a result of these developments, small pore structures, which were not considered as good catalyst materials, have started drawing much attention. $AlPO_4$ – 14, which was first reported by Wilson et al[4], has a three dimensional 8-ring channel system, and falls in small pore category. Since its structure is reported to be quite stable, it may be worth evaluating its performance, after incorporation of redox metals (Mn, Co etc) into its framework, in reactions similar to those mentioned above. Detailed structural information of $AlPO_4$ – 14 and – 18 will pave the way for a better understanding of their reactivity.

It is known that, unlike phosphorus, aluminum can be found in more than one coordination[5-8] in certain $AlPO_4$ structures, both in their as-synthesized as well as calcined and hydrated forms. Unlike in zeolites, which are built of AlO_4^- and SiO_4 tetrahedra, the $AlPO_4$-n frameworks are composed of alternating AlO_4 and PO_4 units and are thus electrically neutral. $AlPO_4$s interact with water to various degrees leading to structural distortion in some cases. This distortion, at times, can be noticed even by powder XRD. Though, powder Rietveld refinement methods are helpful in this regard, their results are not always consistent with those obtained through other characterization methods, in particular, high resolution solid state NMR. $AlPO_4$ frameworks are quite amenable for structural investigations through high-resolution ^{31}P and ^{27}Al solid state NMR spectroscopy. ^{31}P nucleus offers high detection sensitivity and a large enough chemical shift dispersion to identify structurally distinct phosphorus environments in a particular $AlPO_4$ structure. ^{27}Al NMR, despite the high sensitivity offered by a high concentration of the framework species, is beset with severe line broadening due to second-order quadrupolar effects which are not altogether eliminated in MAS

experiments. MQMAS[9] experiments would alleviate such problems and allow the detection and inspection of distinct aluminum environments in the $AlPO_4$ structures.

Heyong et al[10] has investigated $AlPO_4$–18 in detail using ^{27}Al and ^{31}P MAS NMR. They found three crystallographic sites for both phosphorus and aluminum in a 1:1:1 population ratio. A reversible structural change from space group $C_{2/C}$ in the calcined form to a lower symmetry space group in the calcined rehydrated form was observed by them. Calcined sample gave an asymmetric peak in the ^{27}Al MAS spectrum, which was interpreted to be due to three overlapping signals. We were interested in probing this later interpretation through MQMAS NMR. $AlPO_4$ – 14 was investigated by MAS and 2D multiple – quantum techniques, the later method is a suitable method to distinguish non-equivalent aluminum atoms in the structure of such materials[11]. However there are no reports in the literature on the aspects related to hydration-dehydration on this aluminophosphate molecular sieve. Therefore, we have sought to employ ^{31}P MAS, ^{27}Al MAS and ^{27}Al Multiple Quantum Magic Angle Spinning (MQMAS) to provide structural insights on dehydration-rehydration effects on $AlPO_4$ – 14 and $AlPO_4$ – 18. Figures 1 and 2 show the molecular graphics pictures of the framework connectivity established by phosphorus and aluminum in the as-synthesized and calcined $AlPO_4$-14 and $AlPO_4$-18

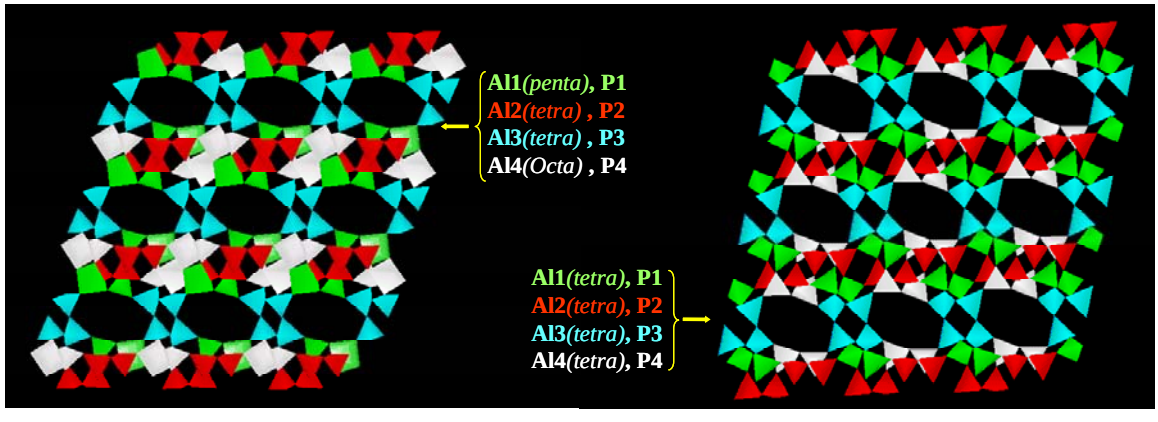

Figure – 1: Framework structure of as-synthesized (left) and calcined (right) $AlPO_4$ – 14. The four nonequivalent phosphorus sites and the aluminum sites existing in different coordinations (AlI^V, Al^V and Al^{VI}) (as-synthesized) and the nonequivalence among Al^{IV} sites in the as-synthesized and calcined forms are indicated.

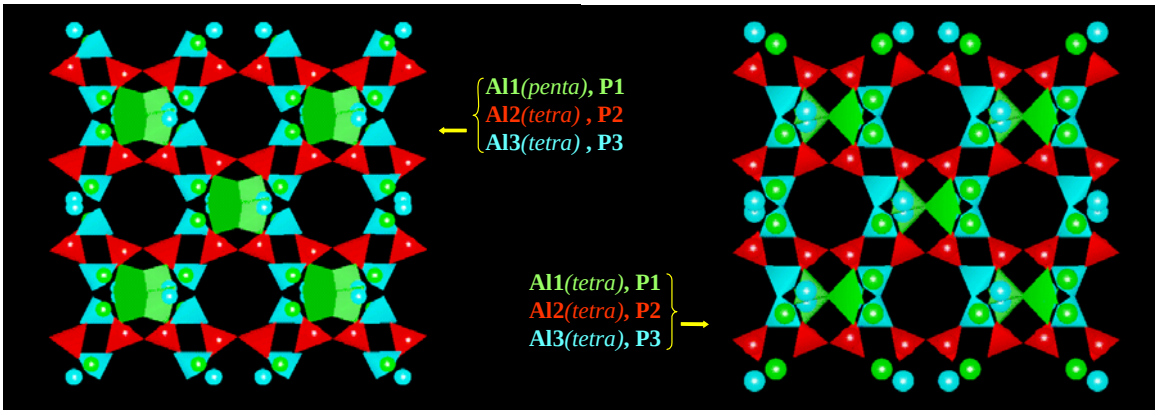

Figure – 2: Framework structure of as-synthesized (left) and calcined (right) $AlPO_4$ – 18. The four nonequivalent phosphorus sites and the aluminum sites existing in different coordinations (Al^{V} and Al^{V}) (as-synthesized) and the nonequivalence among Al^{IV} sites in the calcined forms are indicated.

4.2 Experimental Conditions and Calculations

4.2.1 Solid State NMR

All solid state NMR experiments were performed at the Larmor frequency of 500.13, 130.31 and 202.47 MHz, corresponding to ^{1}H, ^{27}Al and ^{31}P, respectively, on a 11.7 T Bruker Avance 500 NMR spectrometer at ambient probe temperature (295 K). A Bruker double resonance CPMAS probe, equipped to spin 4 mm zirconia rotors, was used. ^{27}Al r.f. pulse length was chosen to be very short, namely, 0.6 μ s, taking into account the nutation behavior[12] of the quadrupolar spins. The ^{27}Al MAS and 3QMAS spectra were collected at a spinning speed of 13 kHz. The 3QMAS spectra were obtained using the three-pulse MQMAS sequence incorporating the z-filter[13] with rotor synchronization during the evolution period (t_1) and ^{1}H decoupling during the evolution and acquisition (t_2) periods using TPPM[14]. The t_1 rotor synchronization ensured the absence of spinning side bands along the isotropic dimension and eased signal identification and quantification, besides improving the S/N. For the 2D experiment, 64 t_1 increments were used and 480 transients were accumulated with a 1 sec recycle delay. For the r.f. field used (υ_{rf} = 60 kHz), the first and second pulses were individually optimized to give maximum efficiencies for the 0Q → ±3Q coherence creation and the ±3Q → 0Q conversion steps, respectively. The last conversion step (0Q → -1Q) to the observed (-1/2 ↔ +1/2) central transition was achieved using a soft 'central transition selective' 90° pulse of duration 9 μs. The phase-sensitive 2D experiments were

conducted using the hypercomplex States[15] procedure, for which the phase of the first r.f. pulse was shifted by 30° between successive experiments. The advantage and description of the MQMAS sequences are explained in detail in chapter – 1. The 1024x1024 2D data matrix was apodized using an exponential (LB=10 Hz) (as-synthesized and calcined) or sine squared bell (SSB=8) (rehydrated samples) window functions along t_1 prior to Fourier-transformation and shearing. This gave pure absorption mode spectra in which the isotropic spectra were obtained by a sum projection of the 2D data onto the δ_{iso} axis. The ^{27}Al chemical shift values are referenced with respect to $[Al(OH)_6]^{3+}$. ^{31}P NMR experiments presented here were performed at the spinning speed of 10 kHz and proton decoupling using TPPM was employed during the acquisition. The ^{31}P chemical shift values are referenced with respect to 85% H_3PO_4. For the simulation and fitting of ^{27}Al MAS spectra and for determination of isotropic chemical shifts and Quadrupolar interaction parameters (e^2qQ/h, η), the software package DMFIT[16] was used.

4.2.2 *ab initio* calculations

All calculations were performed at the Hartree – Fock level using the Gaussian98[17] program. The chemical shielding and electric field gradient tensors were calculated with two basis sets; 6-311g+(2d) and 6-311g+(3d). The EFG tensor elements are calculated in atomic units (au) by the Gaussian98 program. Using a recently determined[18] value of 146.6 x 10^{-31} m^2 for the quadrupole moment (Q) of ^{27}Al, the quadrupole coupling constant (e^2Qq/h) was calculated using the formula:

$$e^2Qq/h\ (MHz) = 0.234965Q(millibarn) \times q_{11}\ (au)$$

q_{11} is the largest component of the electric field gradient tensor.

4.3 ^{31}P, ^{27}Al MAS and ^{27}Al MQMAS of $AlPO_4$ – 14

4.3.1 As-synthesized $AlPO_4$ – 14

The ^{31}P MAS spectrum of as-synthesized $AlPO_4$ – 14 is presented in Figure – 3a. Three resonances with isotropic chemical shifts of –5.1, -19.8 and –23.8 ppm (with respect to H_3PO_4) are identified. From the X-ray crystal structure[19] of $AlPO_4$ – 14, we

reckon that there are four non-equivalent phosphorous in the asymmetric unit. As against the four sites expected with the intensity ratio 1:1:1:1, the ^{31}P MAS spectrum displays the three line spectrum with the intensity ratio 1:2:1, clearly showing that two crystallographic nonequivalent ^{31}P sites have a near chemical shift degeneracy contributing a two-fold enhancement in signal intensity at around 20 ppm.

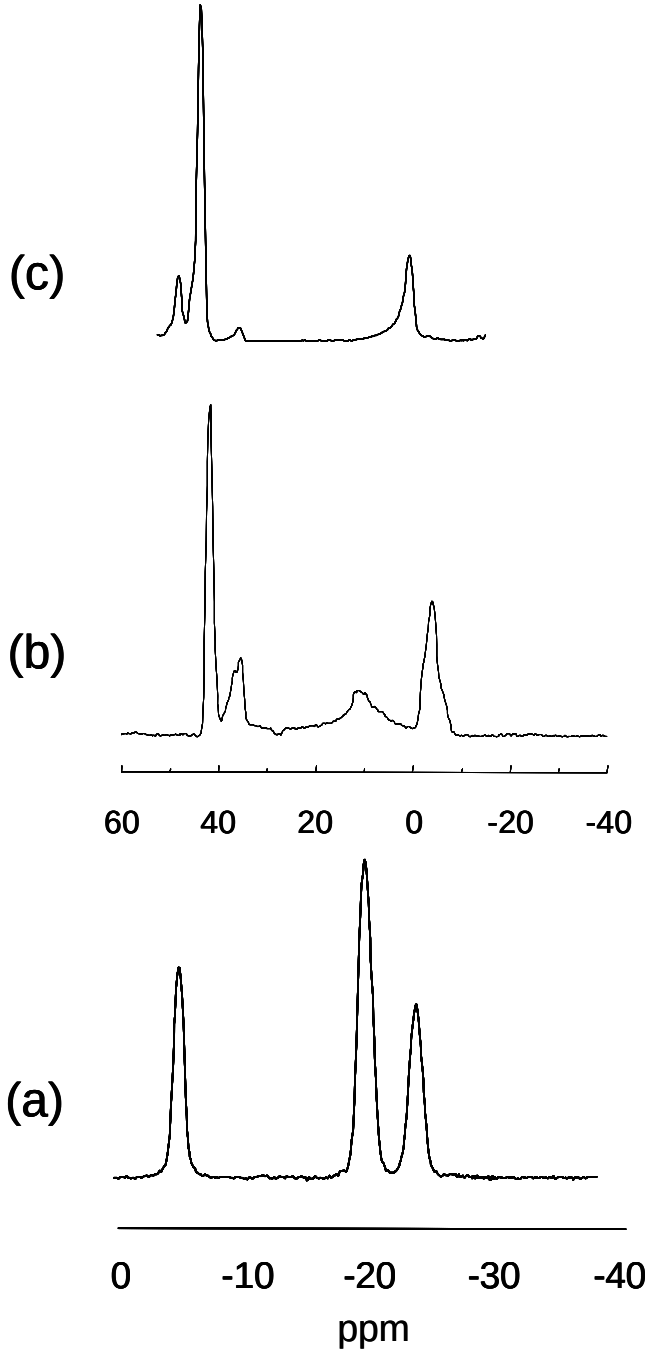

Figure – 3: ^{31}P MAS (**a**), ^{27}Al MAS (**b**) and the isotropic spectrum from ^{27}Al 3QMAS (**c**) of as-synthesized $AlPO_4$ – 14, displaying the crystallographic nonequivalent phosphorus and aluminum sites in different coordination.

The chemical shift dispersion among the observed signals is sufficiently large (*ca*. 19 ppm) and this allows ready assignment of the ^{31}P resonances based on the correlation of the isotropic chemical shifts with the tetrahedral P-O-Al angle[20] which is a measure of the distortion of the tetrahedral units. The assignments of the ^{31}P signals are indicated in Table 1. Since the tetrahedral distortion is nearly same (Table 1) for two of the four crystallographic nonequivalent sites (P1, P4), the ^{31}P spectrum displays a three line pattern with a 1:2:1 intensity.

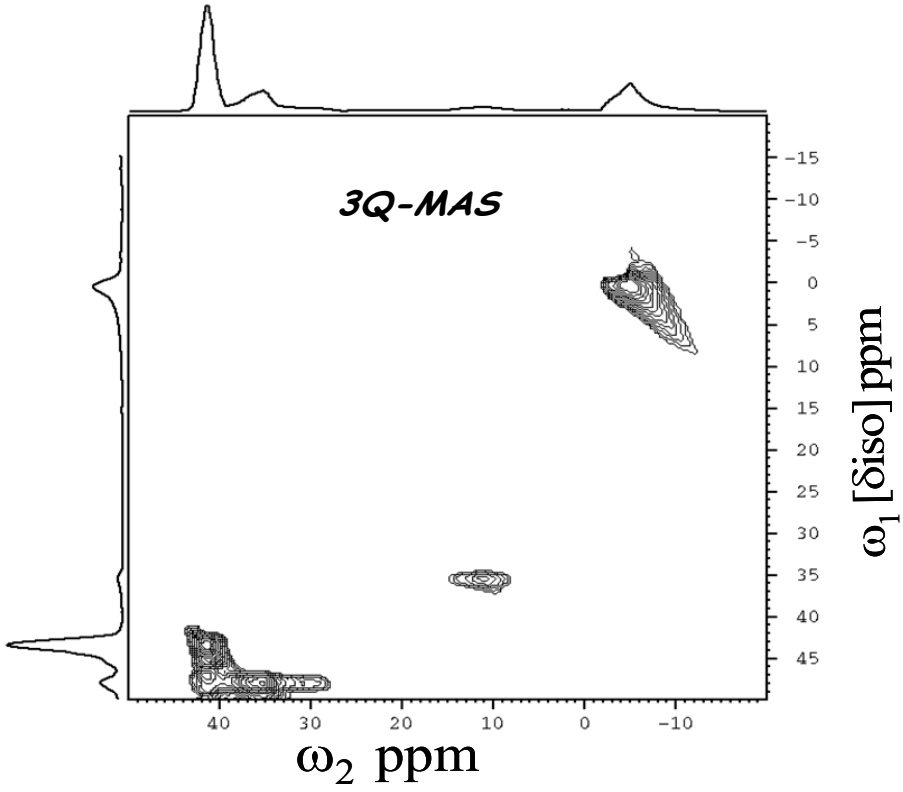

Figure – 4: 2D contour plot of ^{27}Al triple quantum MAS NMR experiment (^{1}H decoupled) of as-synthesized $AlPO_4$-14. The ω_2 projection depicts the CT MAS spectral line shapes for the four, five and six coordinate aluminum, while ω_1 projection yields isotropic spectra for the Al^{IV}, A^{IV} and Al^{VI} species and the identification of two crystallographic nonequivalent Al^{IV} sites.

Though aluminum existing in four, five and six coordinate environments can be identified as well as a two-fold multiplicity for the four coordinate aluminum revealed in the ^{27}Al MAS spectrum (Fig. 3b), the spectrum is complex. Since second-order quadrupolar broadening is not averaged to zero by MAS, the MAS spectrum exhibits central transition powder line shapes, clearly noticed for the Al^{V} (30 to 0 ppm) and Al^{VI} (-20 to 0 ppm) species, respectively. Isotropic spectrum devoid of the second-order

broadening is readily obtained by performing ^{27}Al triple quantum (3Q) MAS experiments. Figure 4 shows the ^{27}Al 3QMAS spectrum of as-synthesized $AlPO_4$-14 obtained after a shearing[21] transformation. ^{27}Al 3QMAS results clearly show four isotropic signals (Figures. 3c and 4), which are readily assigned from the low field end, to octahedral (-1.4 ppm), penta coordinated (-26.7 ppm) and tetrahedral (42.5 and 42.9 ppm) aluminum sites, in due conformity with earlier assignments[11] and the structure of $AlPO_4$ – 14.

Table – 1

Results of Analysis of ^{31}P MAS and ^{27}Al MAS/3QMAS Data of As-synthesized $AlPO_4$-14

^{31}P MAS					
δ_{iso} (ppm)		**Assignment**		**Mean P-O-Al angles**	
-5.1		P2		130.4 ^{o}	
-19.8		P4		138.2 ^{o}	
-19.8		P1		139.7 ^{o}	
-23.8		P3		144.1^o	
^{27}Al MAS/3QMAS					
δ_{iso} (ppm)[1]	**P_Q (MHz)[1]**	**δ_{iso}(MAS)[2]**	**C_Q(MAS)[2]**	**η(MAS)[2]**	**Assignment**
43.3	4.7	42.92	3.93	0.83	Al3
42.9	1.9	42.47	1.73	0.58	Al2
26.4	6.5	26.74	5.64	0.93	Al1
-1.4	2.9	-1.46	2.58	0.65	Al4

[1]From 3QMAS spectrum [2]Obtained by simulation and fitting of the ^{27}Al MAS spectrum

From the graphical analysis of 3QMAS spectrum, the chemical shift (CS) and quadrupole interaction (P_Q) parameters could be readily estimated. These, in turn, were used in DIMFIT simulations of ^{27}Al MAS spectra for the accurate determination of δ_{iso} , C_Q and η_Q. These are included in Table-1. The 'best-fit' computer simulated ^{27}Al MAS spectrum is compared with the experimental spectrum in Figure 5.

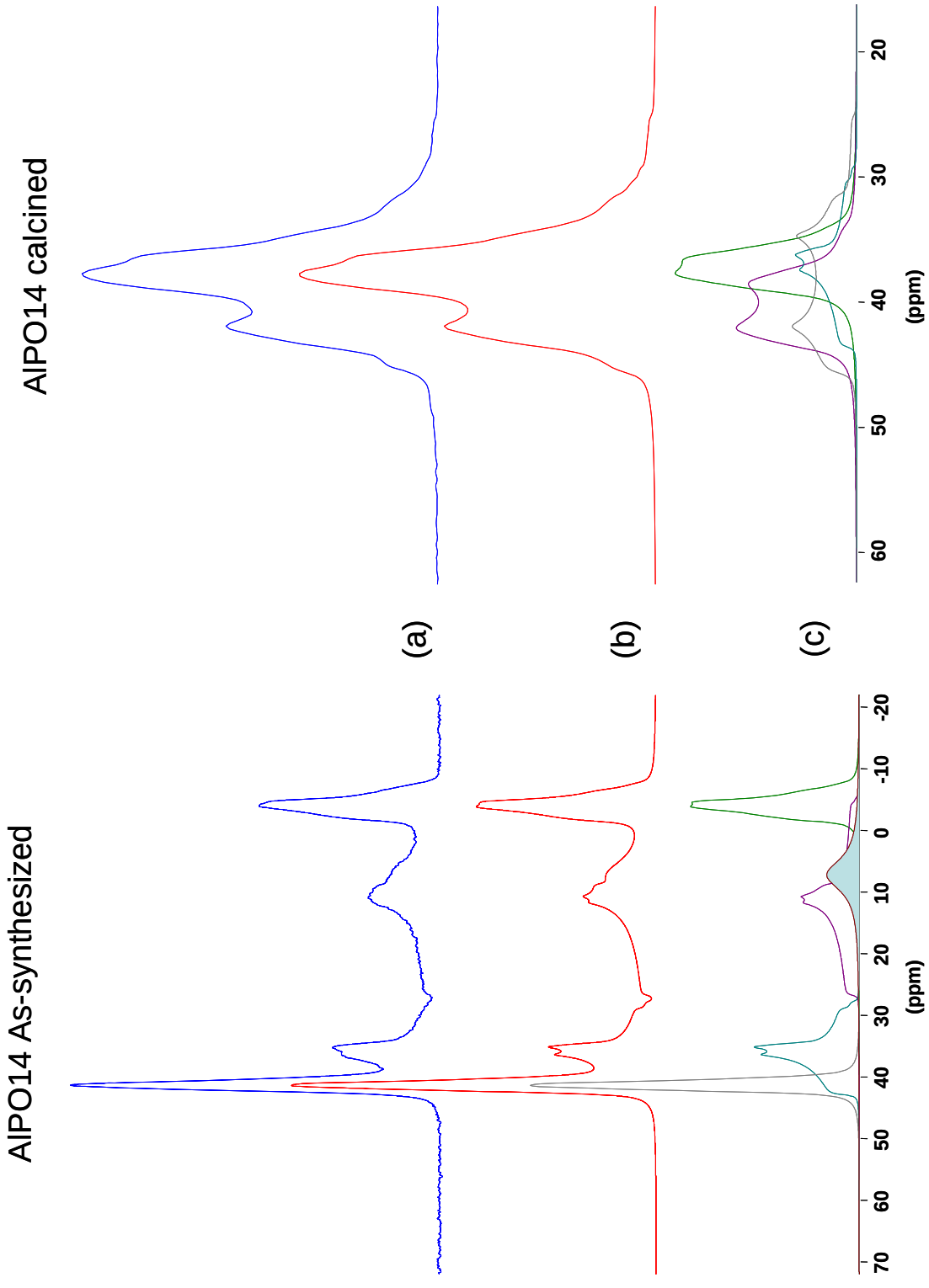

Figure – 5: Comparison of experimental ^{27}Al MAS spectra (**a**) of as-synthesized (left) and calcined (right) $AlPO_4$-14 with the corresponding computer simulated spectra (**b**) using the 'best fit' parameters given in Table 1. The simulations of the CT MAS spectra of the individual Al^{IV}, Al^{V} and Al^{VI} sites, constituting the composite line shapes of (**b**) are shown in (**c**).

4.3.2 Calcined and Dehydrated $AlPO_4$ – 14

In the as-synthesized $AlPO_4$-14, aluminum exists in 4, 5 and 6 co-ordinations, and the Al^V and Al^{VI} environments arise due to the presence of structured water and the pore-directing template. Thus, dehydration, which removes the water, and calcinations, which removes the template, would affect the aluminum co-ordination. The structural changes that ensue due to changes in aluminum co-ordination, can be monitored by both ^{31}P MAS and ^{27}Al MAS/MQ-MAS NMR. The rewards are mainly due to a large chemical shift dispersion in the case of ^{31}P, while in the case of ^{27}Al the electric field gradients will be affected to a great extent by the removal of water and template in the close vicinity of the aluminum sites.

The ^{31}P MAS spectrum of calcined and dehydrated $AlPO_4$ – 14 is presented in Figure – 6a. Three resonances with isotropic chemical shifts of –21.4, -26.6 and –31.4ppm (with respect to H_3PO_4) are identified. For the calcined and dehydrated $AlPO_4$-14, the ^{31}P MAS spectra depict three resolved signals in the intensity ratio 1:2:1 (Figure – 6a). Since the removal of water and the template changes only the coordination of aluminum, and not the phosphorus, the phosphorus sites must occupy tetrahedral locations in the calcined and dehydrated material. Inspection of X-ray data of calcined dehydrated $AlPO_4$ – 14[19] shows that there are four inequivalent phosphorous T-sites in the asymmetric unit. As against the four sites expected with the intensity ratio 1:1:1:1, the ^{31}P MAS spectrum displays the three line spectrum with the intensity ratio 1:2:1, clearly showing that two crystallographic nonequivalent ^{31}P sites have a near chemical shift degeneracy. This contributes to a two-fold enhancement in signal intensity at –26.4 ppm It is interesting to note that a similar three line pattern is also observed in the as-synthesized material, where the chemical shift dispersion is larger (18.7 ppm). The ^{31}P MAS observation shows that two of the sites are not resolved due to small difference in the isotropic chemical shifts associated with these sites. Based on correlation of isotropic chemical shifts with average T-O-T angle[20] we may assign the ^{31}P resonances to the crystallographically nonequivalent atoms in the crystal structure as shown in Table – 2. The calcined and dehydrated form of $AlPO_4$-14 has never been assigned before.

Despite the decrease in chemical shift dispersion among the ^{31}P resonance positions in the calcined and dehydrated $AlPO_4$-14 (10 ppm), the correlation of the isotropic chemical shifts with the tetrahedral P-O-Al angle[20], which is a measure of the distortion of the tetrahedral units, allows us to make an assignment.

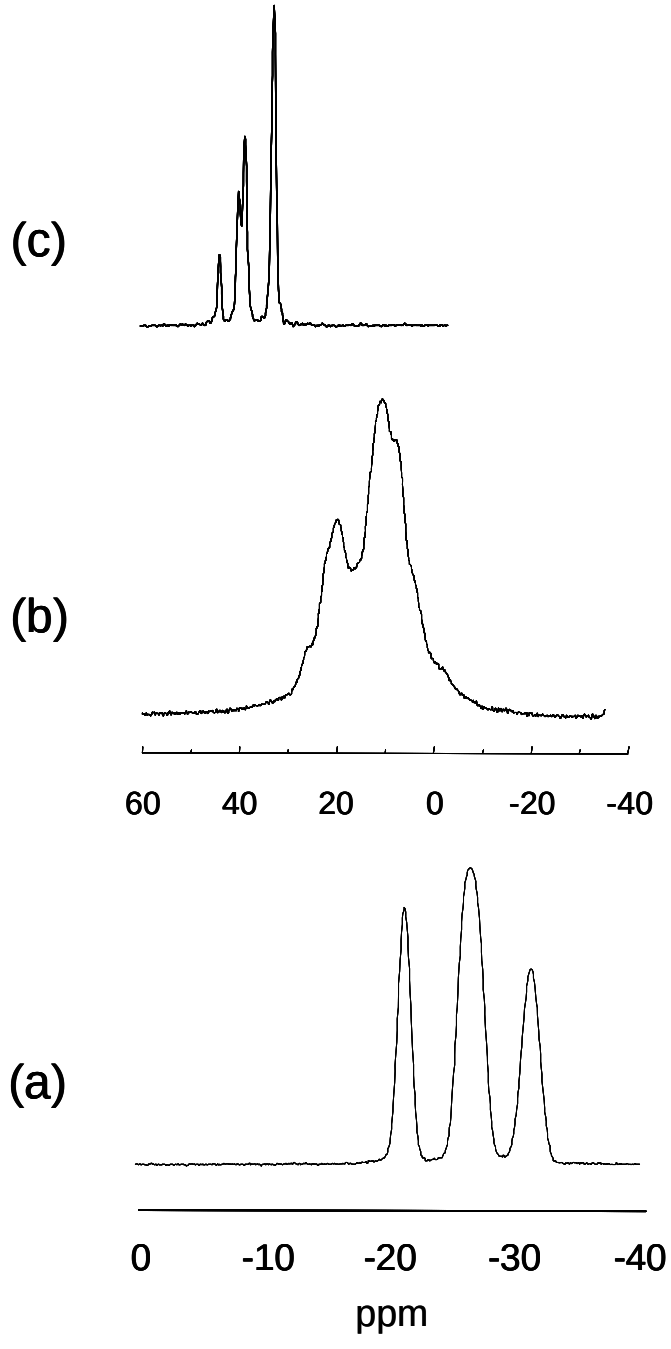

Figure – 6: ^{31}P MAS (**a**), ^{27}Al MAS (**b**) and the isotropic spectrum from ^{27}Al 3QMAS (**c**) of calcined and dehydrated $AlPO_4$ – 14, displaying the crystallographic nonequivalent tetrahedral phosphorus and aluminum sites.

The assignments of the ^{31}P signals are indicated in Table 2. Since the tetrahedral distortion is nearly same (Table 2) for two of the four crystallographic nonequivalent sites (P2, P4), the ^{31}P spectrum displays a three line pattern with a 1:2:1 intensity.

The change in aluminum co-ordination causes the observed change in ^{27}Al spectral features. Clearly, all the aluminum must exist in four-fold co-ordination in the calcined and dehydrated material. Thus, the spectral features observed in the ^{27}Al CT MAS spectrum must be associated with the multiplicity of the tetrahedral environments, with the line features and broadening emanating from the residual second-order broadening which is not completely eliminated by MAS (Figure 6b). An isotropic spectrum devoid of the second-order broadening is readily obtained by performing ^{27}Al triple quantum (3Q) MAS experiments. Figure 7 shows the ^{27}Al 3QMAS spectrum of calcined and dehydrated $AlPO_4$-14 obtained after a shearing[21] transformation. ^{27}Al 3QMAS results clearly show four isotropic signals (Figures. 6c and 7), which are attributable to the presence of four crystallographic nonequivalent Al^{IV} sites in the structure. From the graphical analysis of 3QMAS spectrum, the chemical shift (CS) and quadrupole interaction (P_Q) parameters could be readily estimated. These, in turn, were used in DIMFIT simulations of ^{27}Al MAS spectra for the accurate determination of δ_{iso} , C_Q and η_Q. The final results of the MAS and 3Q-MAS analysis are given in Table-2. The 'best-fit' computer simulated ^{27}Al MAS spectrum is compared with the experimental spectrum in Figure 5.

For the assignments of the four isotropic ^{27}Al resonances resolved from 3Q-MAS experiments, we do not rely on a T-O-T angle based correlation since the chemical shift dispersion is not large enough, especially for two of the resonances at 43.6 and 44.5 ppm. Hence, *ab initio* quantum chemical calculation of ^{27}Al isotropic chemical shifts and quadrupolar couplings were carried out using cluster models and the Gaussian program. The pentameric clusters were generated from the parent structure determined by X-ray diffraction[19]. The *ab initio* calculations were performed at high level basis sets 6-311g+(2d) and 6-311g+(3d). As noticed in Chapter 2, where we have discussed the ^{27}Al *ab initio* calculations of aluminum hydroxides in detail, the theoretically determined values for the NMR parameters can not be matched with experimental determinations in absolute numbers. However, based on the observed

trend among the experimental and calculated values and a good correlation they establish, we are in a position to assign the ^{27}Al isotropic signals entirely based on *ab initio* calculations.

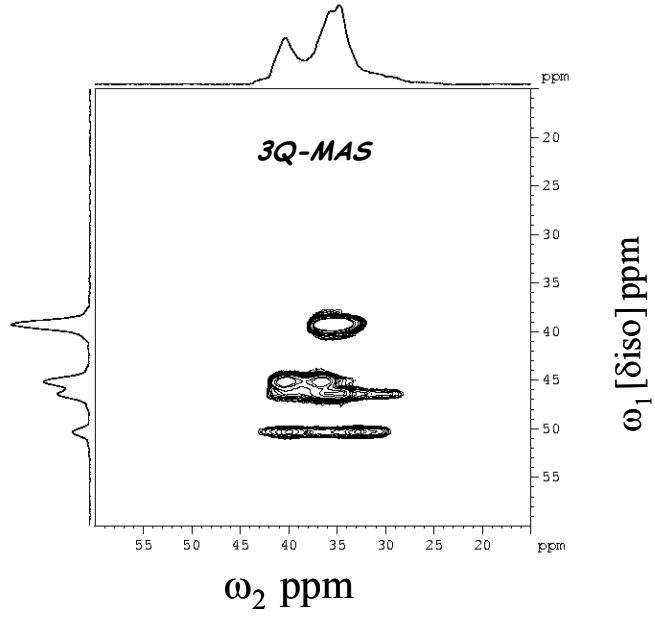

Figure –7: 2D contour plot of ^{27}Al triple quantum MAS NMR experiment (^{1}H decoupled) of calcined and dehydrated $AlPO_4$-14. The ω_2 projection depicts the CT MAS spectral line shapes for the four coordinate aluminum, while ω_1 projection yields isotropic spectra depicting the identification of four crystallographic nonequivalent Al^{IV} sites.

Table – 2

Results of Analysis of ^{31}P MAS and ^{27}Al MAS/3QMAS Data and Assignments of Crystallographic non-equivalent Sites in the Calcined and Dehydrated $AlPO_4$-14

^{31}P NMR results					
δ_{iso}	Assignment	Intensity			
-21.4	P1	1			
-26.6	P2, P4	2			
-31.4	P3	1			
^{27}Al NMR results					
δ_{iso}[1]	δ_{CS}[1]	P_Q[1]	δ_{iso}(*MAS*)[2]	C_Q(*MAS*)[2]	η(*MAS*)[2]
37.9	39.3	2.3	39.48	2.50	0.43
42.4	46.4	4.0	44.49	3.46	0.25
42.8	45.2	3.1	43.63	3.83	0.82
45.5	50.4	4.4	47.18	4.96	0.30
δ_{CS}(*cal1*)[3]	δ_{CS}(*cal2*)[3]	P_Q(*cal1*)[3]	P_Q(*cal2*)[3]	Assignment	
41.3	40.6	3.8	3.7	Al1	
54.0	53.8	5.2	5.1	Al2	
44.5	44.7	4.5	4.4	Al3	
60.3	60.4	5.3	5.3	Al4	

[1]From 3QMAS spectrum [2]Obtained by simulation and fitting of the ^{27}Al MAS spectrum
[3]Cal1 and cal2 in parenthesis correspond to values from ab initio quantum chemical calculations using basis sets 6-311g+(2d) and 6-311g+(3d), respectively.

The results of the *ab initio* calculations of isotropic chemical shifts using two different basis sets and the assignments of the aluminum resonances based on the calculations are tabulated in Table – 2. For sites Al2 and Al3 even though the chemical shift differences are very small, there is a considerable difference in the values for the quadrupolar coupling constant. A plot of the experimental versus the calculated chemical shift and quadrupolar coupling values are shown in Figure – 8. The experimentally observed trend for the chemical shift and quadrupolar coupling constant (QCC) values for all the four aluminum sites in calcined $AlPO_4$-14 is in perfect accord with the theoretical determinations carried out at two different basis sets. Also an improvement in the R^2 value can be seen with the larger basis set. Thus by combining

the chemical shift and EFG calculations, unambiguous assignments of the crystallographically inequivalent sites could be made possible.

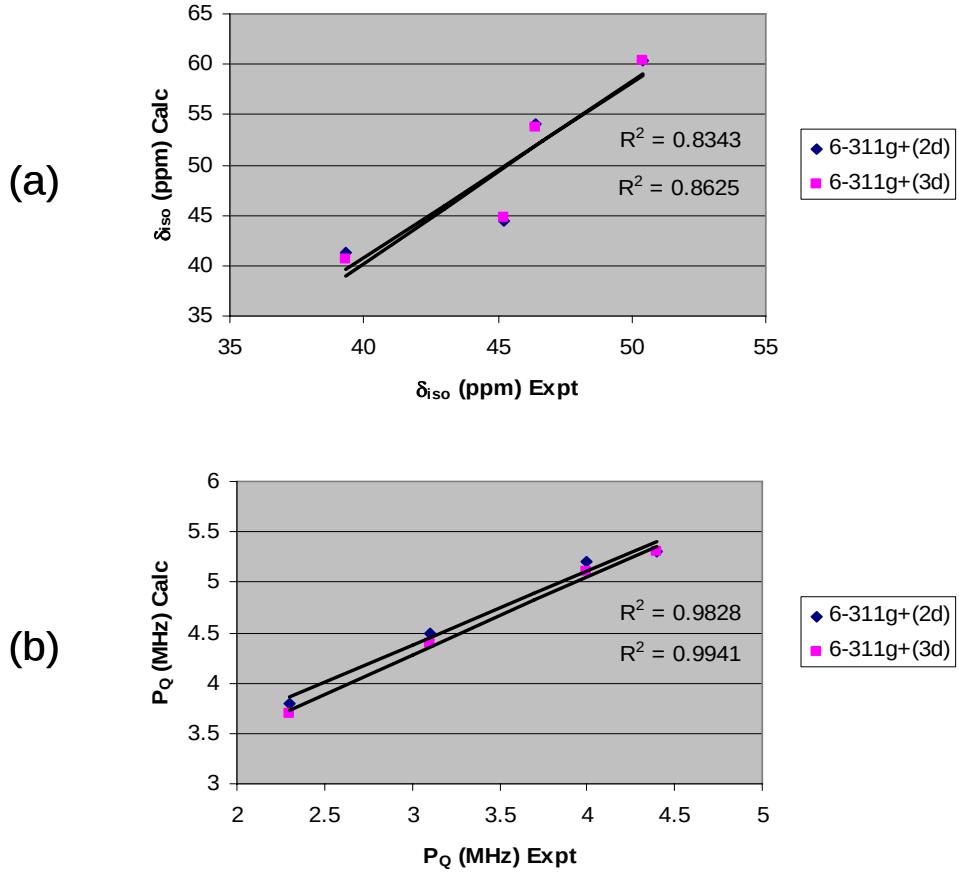

Figure – 8: Plot of experimental versus calculated values of (a) ^{27}Al chemical shift and (b) quadrupolar coupling constant for the four tetrahedral Al sites in calcined and dehydrated $AlPO_4$-14 at two different basis sets.

4.3.3 Calcined and Rehydrated $AlPO_4$ – 14

The structural changes brought about by rehydration of the calcined and dehydrate $AlPO_4$-14 has also been studied by ^{31}P MAS and ^{27}Al MAS and 3Q-MAS. The ^{31}P result, shown in Figure-9a, show an enhanced signal multiplicity for the ^{31}P resonances in tetrahedral environments than that seen in the case of as-synthesized and calcined and dehydrated sample. Similarly, the ^{27}Al 3Q-MAS spectra, presented in Figure-10 also shows a near two-fold multiplicity for aluminum resonances within each of the 4, 5 and 6-fold coordinated environments. This can be readily inferred from the isotropic spectrum (Figure – 9c), obtained after a shearing of the 3Q-MAS 2D data.

Such a feature cannot be gathered from the ^{27}Al MAS spectrum (Figure – 9b), where second-order quadrupolar broadening leads to a complex line shape with no information regarding the number of inequivalent aluminum sites.

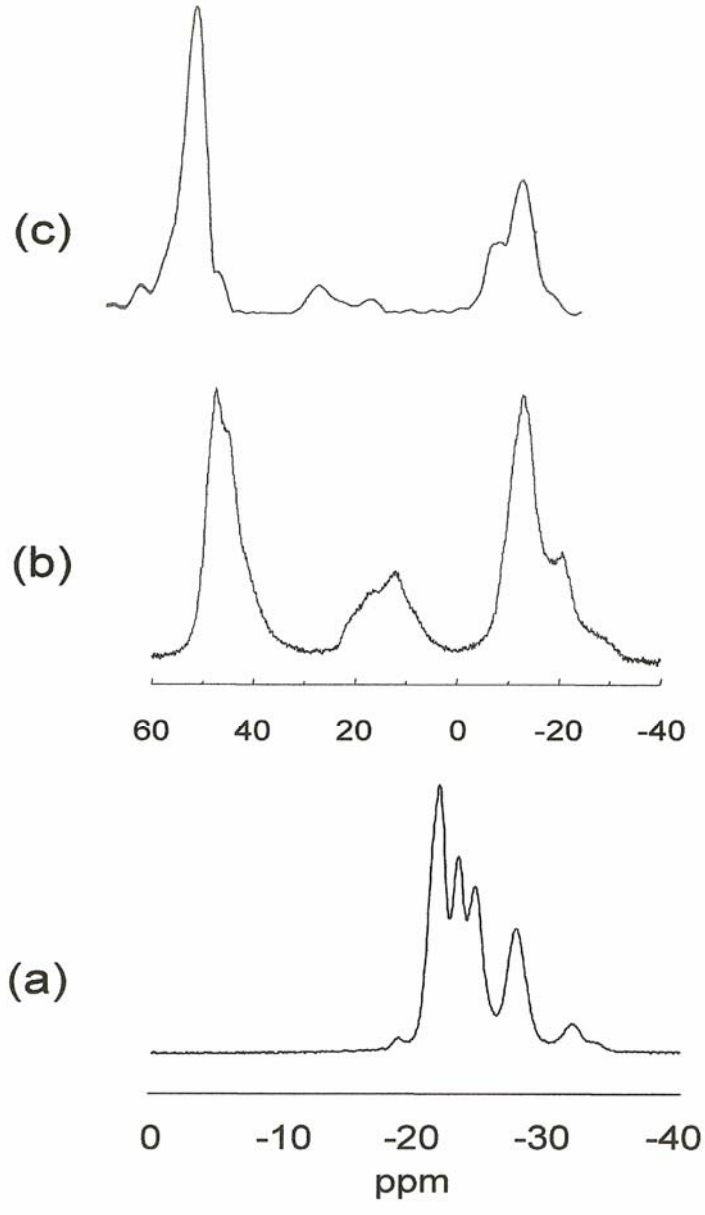

Figure – 9: ^{31}P MAS (**a**), ^{27}Al MAS (**b**) and the isotropic spectrum from ^{27}Al 3QMAS (**c**) of calcined and rehydrated $AlPO_4$ – 14, displaying the crystallographic nonequivalent tetrahedral phosphorus sites aluminum sites in 4,5 and 6 coordinations.

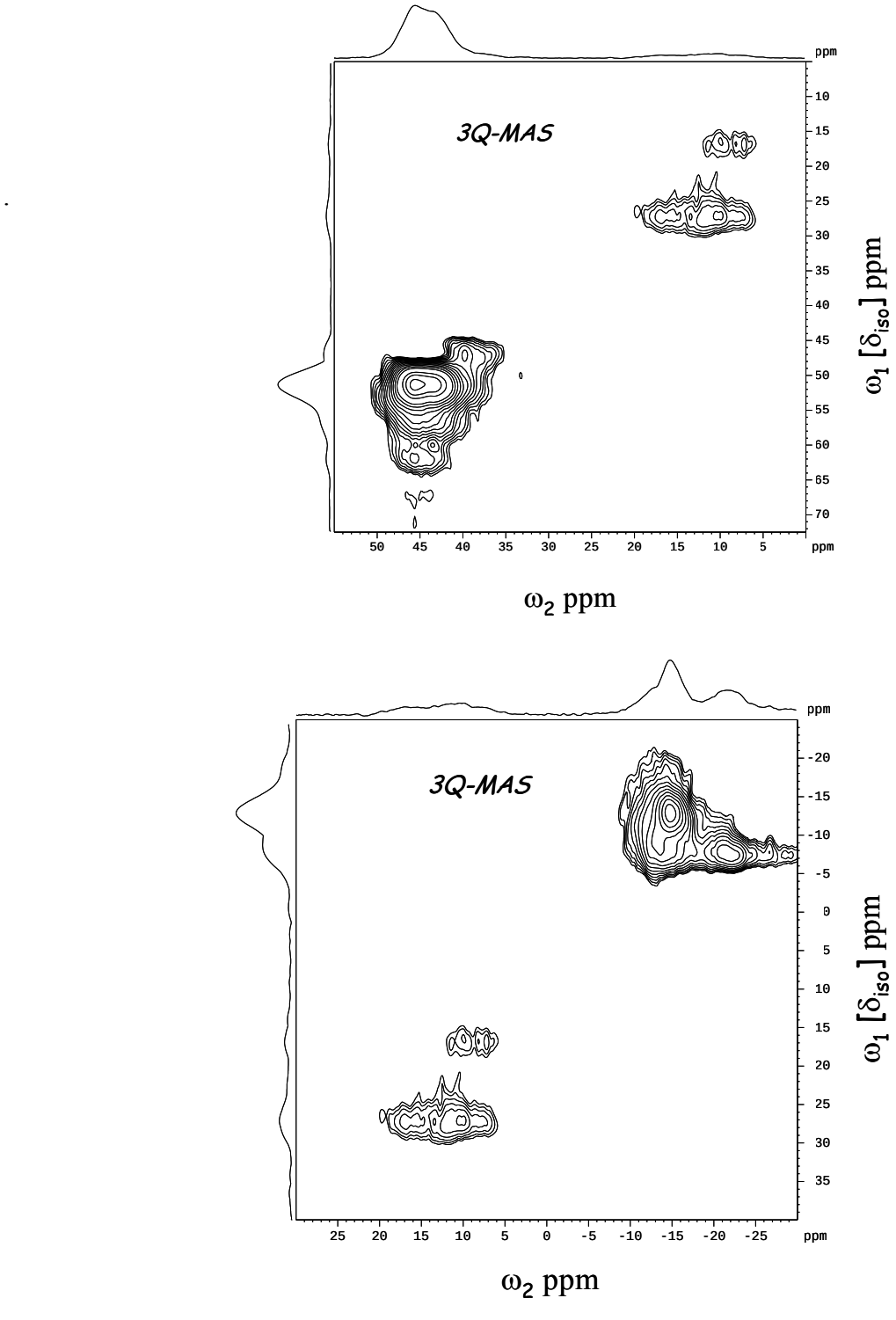

Figure – 10: 2D contour plot of ^{27}Al triple quantum MAS NMR experiment (^{1}H decoupled) of calcined and rehydrated $AlPO_4$-14. The ω_2 projection depicts the CT MAS spectral line shapes, while ω_1 projection yields the corresponding isotropic spectra. The low (upper) and high (lower) field regions are shown separately to depict the signal multiplicity for the Al^{IV}, A^{IV} and Al^{VI} species.

From the ^{27}Al 3Q-MAS results, it is clear that hydration transforms local symmetry from tetrahedral environment into others (penta and hexa). The increase in the coordination is due to the formation of coordinate bonds by water with aluminum. The ^{31}P and ^{27}Al 3QMAS results, taken together, bring out the fact that calcined rehydrated $AlPO_4$ – 14 corresponds to a new structure, possibly one with lower space group symmetry than the known structure of the as-synthesized and calcined materials. Although the structural transformation occurring due to rehydration is evident from the experimental results, the lack of X-ray structure data precludes unique assignments of the ^{31}P and ^{27}Al isotropic resonances to be made.

Table – 3

Results of Analysis of ^{31}P MAS and ^{27}Al MAS/3QMAS Data for the non-equivalent Phosphorus and Aluminum sites in Calcined and Rehydrated $AlPO_4$-14

^{31}P MAS	^{27}Al 3Q-MAS	
δ_{iso} (ppm)	δ_{iso} (ppm)	P_Q (MHz)
-33.5	55.83	5.37
-31.8	49.10	3.28
-27.6	44.39	3.63
-24.5	21.19	5.34
-23.2	13.98	3.85
-21.8	-12.71	5.07
-18.7	-13.56	2.29

4.4 ^{31}P, ^{27}Al MAS and ^{27}Al MQMAS of $AlPO_4$ – 18

4.4.1 As-synthesized $AlPO_4$ – 18

The ^{31}P MAS spectrum of as-synthesized $AlPO_4$–18 is presented in Figure – 11a. Three resonances with isotropic chemical shifts of -12, -28 and -30 ppm (with respect to H_3PO_4), with the intensity ratio of 1:1:1, are identified. This is consistent with the structure[8] of $AlPO_4$–18 which contains three crystallographically inequivalent P and Al sites with the occupancy of 1:1:1. It may be noticed that the chemical shift dispersion among the observed signals is sufficiently large (*ca*. 18 ppm) and this allows ready assignment of the ^{31}P resonances based on the correlation of the isotropic chemical shifts with the tetrahedral P-O-Al angle[20, 22] which is a measure of the distortion of the tetrahedral units. From the crystal structure data of as-synthesized $AlPO_4$ – 18 we gather

for the P-O-Al angle: 144.3^0 (P1), 148.5^0 (P2) and 131.4^0 (P3). Thus the three-line spectrum for the as-synthesized sample is readily assigned to the three crystallographic non-equivalent sites in the structure of $AlPO_4$ – 18, in conformity with the earlier MAS NMR study[10]. The assignments of the various P sites are shown in Table – 4.

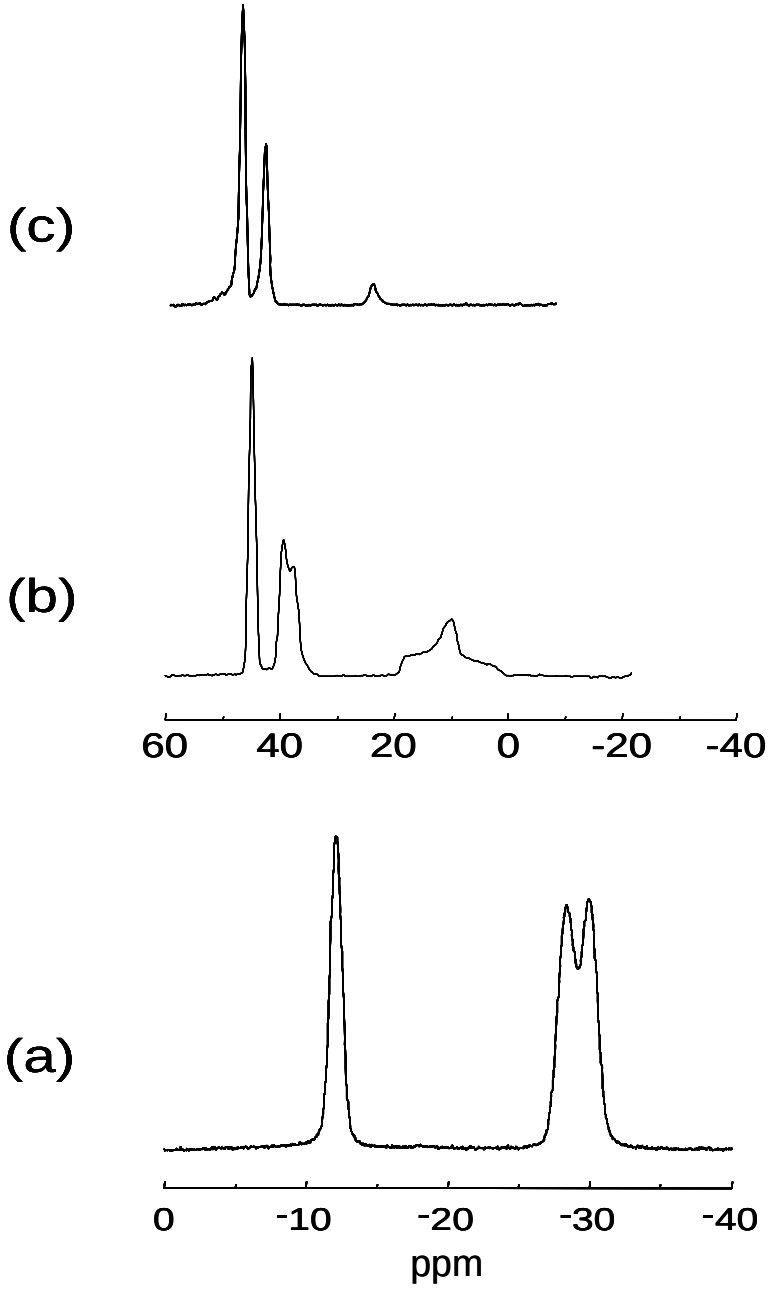

Figure – 11: ^{31}P MAS (**a**), ^{27}Al MAS (**b**) and the isotropic spectrum from ^{27}Al 3QMAS (**c**) of as-synthesized $AlPO_4$–18, displaying the crystallographic nonequivalent phosphorus and aluminum sites and aluminum sites in different coordination.

Table – 4

Results of Analysis of ^{31}P MAS and ^{27}Al MAS/3QMAS Data and Assignments of Crystallographic non-equivalent Sites in the As-synthesized $AlPO_4$-18

^{31}P NMR					
δ_{iso} (ppm)	**Assignment**		**Mean P-O-Al angles**		
-12	P3		131.4 ^{o}		
-28	P1		144.3 ^{o}		
-30	P2		148.5 ^{o}		
^{27}Al NMR					
δ_{iso}(ppm)[1]	**P_Q (MHz)[1]**	**δ_{iso}(*MAS*)[2]**	**C_Q(*MAS*)[2]**	**η(*MAS*)[2]**	**Assignment**
18.42	4.98	18.79	4.24	1.00	Al1
40.79	2.69	40.67	2.54	0.00	Al3
45.68	1.71	45.61	1.47	0.55	Al2

[1]From 3QMAS spectrum
[2]Obtained by simulation and fitting of the ^{27}Al MAS spectrum

^{27}Al MAS spectrum is shown in Figure 11b. Only tetrahedral and penta-coordinated aluminum environments can be identified and the octahedral aluminum is clearly absent. A two-fold multiplicity for the four coordinate aluminum is also evident from the ^{27}Al spectrum, despite the second-order quadrupolar broadening. Figure 12 shows the ^{27}Al 3QMAS spectrum of as-synthesized $AlPO_4$-18 obtained after a shearing[21] transformation. ^{27}Al 3QMAS results clearly show three isotropic signals (Figures. 11c and 12), readily assigned to the two non-equivalent tetrahedral and one penta coordinated aluminum sites present in the structure, in agreement with the X-ray data[8]. From the graphical analysis of 3QMAS spectrum, the chemical shift (CS) and quadrupole interaction (P_Q) parameters could be readily estimated. These, in turn, were used in DIMFIT simulations of ^{27}Al MAS spectra for the accurate determination of δ_{iso} , C_Q and η_Q. These are included in Table-4. The 'best-fit' computer simulated ^{27}Al MAS spectrum is compared with the experimental spectrum in Figure 13.

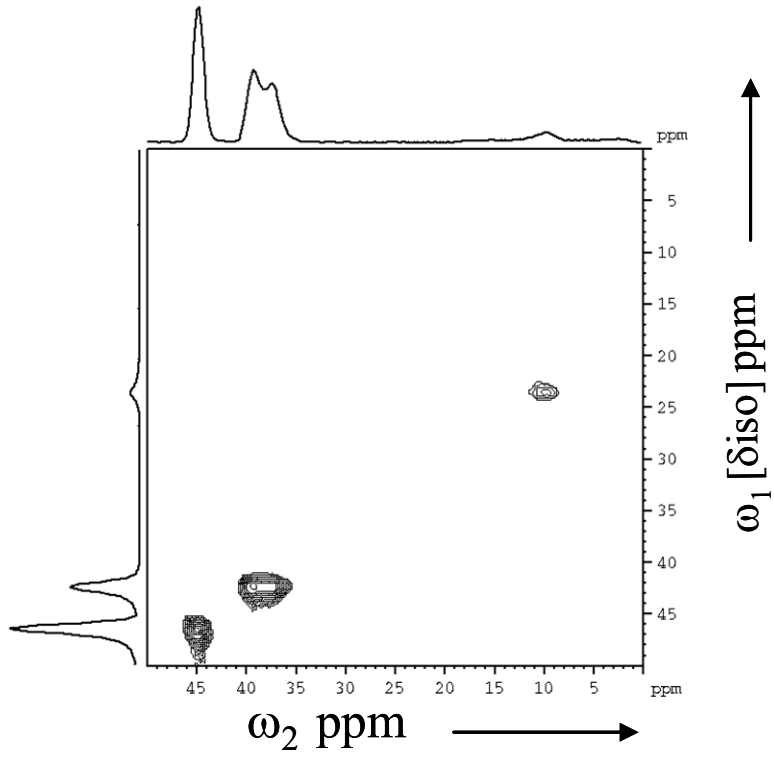

Figure – 12: 2D contour plot of ^{27}Al triple quantum MAS NMR experiment (^{1}H decoupled) of as-synthesized $AlPO_4$-18. The ω_2 projection depicts the CT MAS spectral line shapes for the four and five coordinate aluminum, while ω_1 projection yields isotropic spectra for the Al^{IV} and A^{V} species and the identification of two crystallographic nonequivalent Al^{IV} sites.

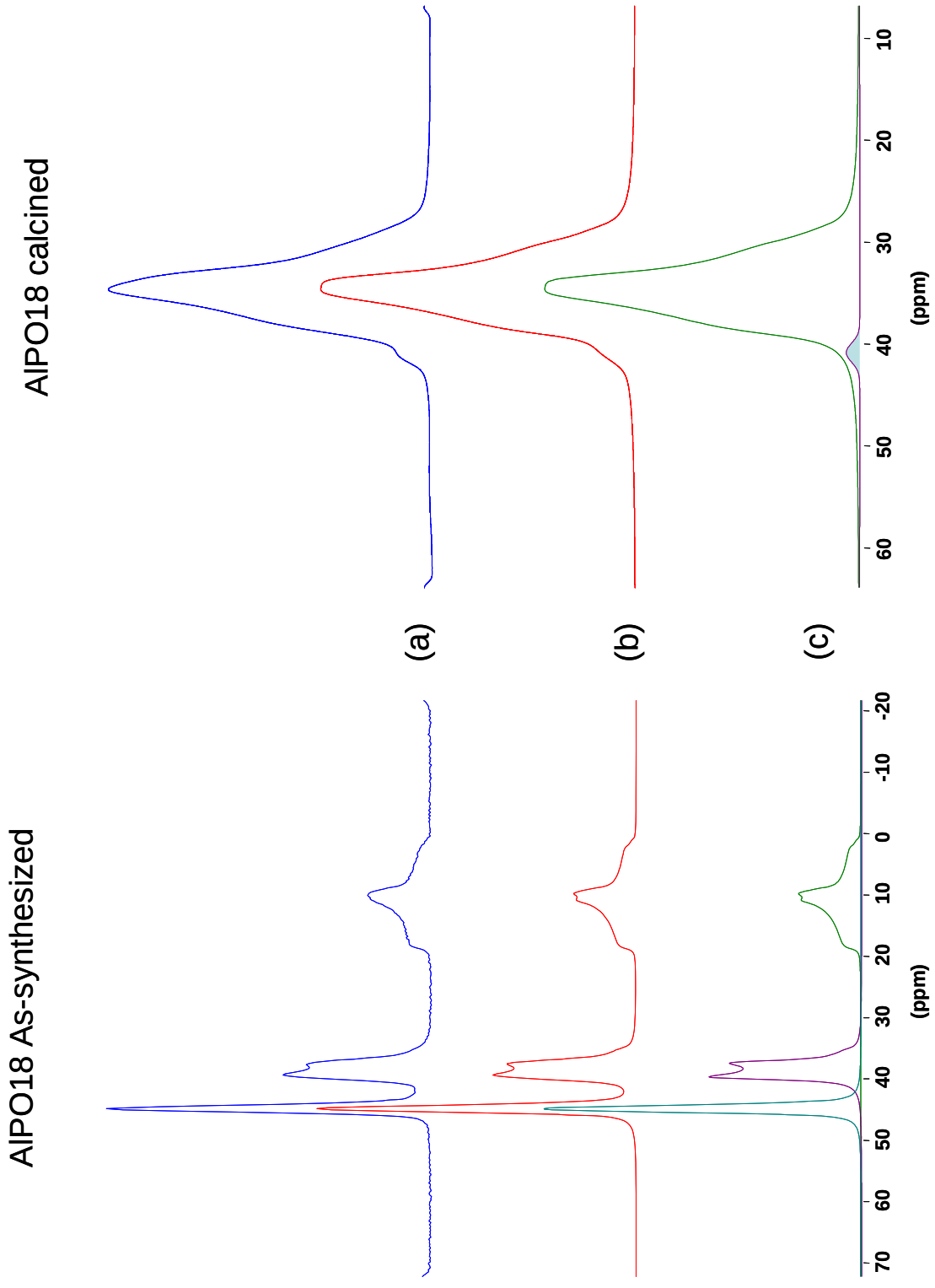

Figure – 13: Comparison of experimental ^{27}Al MAS spectra (**a**) of as-synthesized (left) and calcined (right) $AlPO_4$-18 with the corresponding computer simulated spectra (**b**) using the 'best fit' parameters given in Table 1. The simulations of the CT MAS spectra of the individual Al^{IV} and Al^{V} sites, constituting the composite line shapes of (**b**) are shown in (**c**).

Since there are three crystallographically inequivalent Al sites having occupancy 1:1:1 and the ^{27}Al 3Q-MAS projections also show three resonances, we reckon that each resonance must belong to a distinct Al site. It is easy to assign the resonance at 18 ppm to the penta coordinated Al1 site by considering the chemical shift and the quadrupolar coupling values. The assignment of the remaining two resonances at 40 and 45 ppm to the two inequivalent T_d sites in the structure is not straight forward since their chemical shift values are very close to each other. However, the 3QMAS analysis shows that there is a large difference in the quadrupolar coupling constants for the two sites. The resonance at 40 ppm has a larger QCC than the resonance at 45 ppm. Since QCC has a strong dependence on the symmetry of the Al environment, we have estimated the asymmetry at the Al site based on the $AlPO_4$-18 geometry using the crystal structure, thus making it possible to assign the Al sites based on the estimates of QCC. The assignments of the various Al sites are shown in Table – 4. This is found to be in accord with that reported in the literature[10].

4.4.2 Calcined and Dehydrated $AlPO_4$ – 18

The structural changes that ensue due to calcinations and dehydration, which remove the template and water, have also been studied in $AlPO_4$-18 by ^{31}P MAS and ^{27}Al MAS/MQ-MAS. The ^{31}P spectrum of calcined and dehydrated sample displays a single resonance at -30.7 ppm even at 11.7 T magnetic field and fails to reveal any signal multiplicity (Fig. 14a). ^{27}Al MAS spectrum is shown in Figure 14b. The penta-coordinate aluminum is absent, as the extra coordination to template and water has been removed by calcinations and dehydration. The ^{27}Al CT spectrum depicts a single asymmetric line in the tetrahedral region and provides no clues about the number of inequivalent tetrahedral aluminum sites. Earlier, Heyong[10] *et al* had observed such an asymmetric line shape and attributed this to three overlapping resonances. The ^{27}Al 3QMAS spectrum of calcined and dehydrated $AlPO_4$-18 is shown in Figure-15. Although the second-order quadrupolar broadening seen in ^{27}Al MAS spectrum has been removed, 3QMAS results show that there is only a single ^{27}Al isotropic signal at 38.6 ppm.

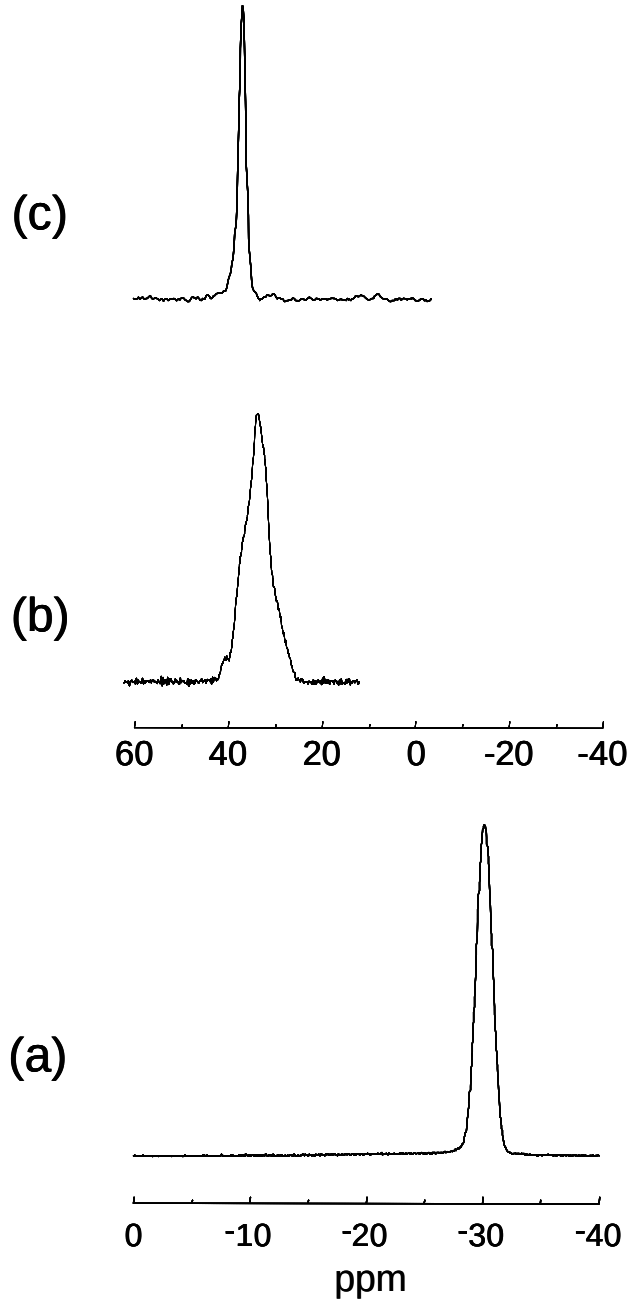

Figure – 14: ^{31}P MAS (**a**), ^{27}Al MAS (**b**) and the isotropic spectrum from ^{27}Al 3QMAS (**c**) of calcined and dehydrated $AlPO_4$–18, displaying a single resonance for the tetrahedral phosphorus sites and a single isotropic resonance for the tetrahedral aluminum.

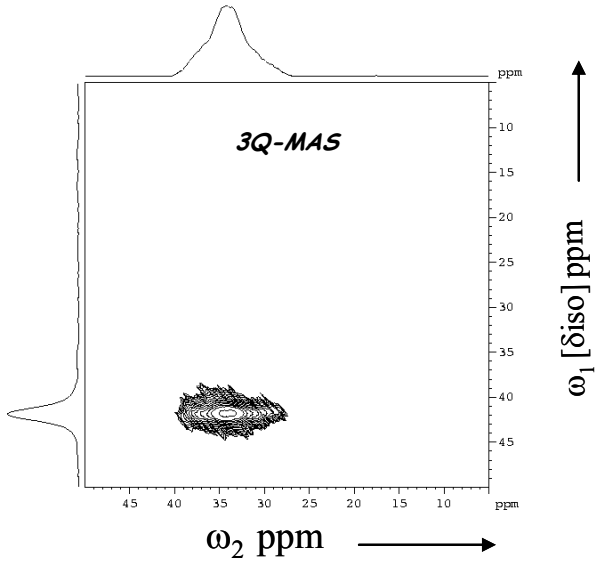

Figure – 15: 2D contour plot of ^{27}Al triple quantum MAS NMR experiment (^{1}H decoupled) of calcined and dehydrated $AlPO_4$-18. The ω_2 projection depicts the CT MAS spectral line shapes for the four coordinate aluminum, while ω_1 projection yields isotropic spectra for the Al^{IV}.

The structure of calcined and dehydrated $AlPO_4$ – 18 contains three phosphorus and aluminum crystallographic sites with an occupancy of 1:1:1 with all the phosphorus and aluminum atoms in tetrahedral coordination. Upon removal of the template, the environment of the framework P and Al in calcined $AlPO_4$-18 is affected and there is a geometrical alteration of the tetrahedral units. Since the structural influence from template and water has been eliminated, the variations in tetrahedral site geometry are not as large in the calcined and dehydrated $AlPO_4$-18 compared to the as-synthesized sample. More significantly, ^{31}P and ^{27}Al NMR observations in calcined and dehydrated $AlPO_4$-18 emphasize the fact that the distortion of PO_4 and AlO_4 units must be much smaller in comparison to the structural modification of $AlPO_4$ – 14. This is in excellent accord with a small value of 1.7^0 noticed for the deviation of T-O-T angle (147.9^0 to 149.6^0) for phosphorus and (147.3^0 to 150.6^0) for aluminum[8]. We ought to expect that this would lead to a very small dispersion in the ^{31}P isotropic chemical shifts and ^{27}Al QCCs and thus mask the resolution in the ^{31}P MAS and ^{27}Al isotropic spectra.

Table – 5

Results of Analysis of ^{31}P MAS and ^{27}Al MAS/3QMAS Data for the non-equivalent Phosphorus and Aluminum sites in Calcined and Dehydrated $AlPO_4$-18

^{31}P NMR results					
δ_{iso} (ppm)		**Assignment**		**Mean P-O-Al angles**	
30.1		P1, P2, P3		147.9 ^{o} to 149.6 ^{o}	
^{27}Al NMR results					
δ_{iso}(ppm)[1]	P_Q (MHz)[1]	$\delta_{iso}(MAS)^2$	$C_Q(MAS)^2$	$\eta(MAS)^2$	Assignment
39.1	3.6	39.17	3.35	0.7	Al1,2,3
		40.83			Impurity

[1]From 3QMAS spectrum
[2]Obtained by simulation and fitting of the ^{27}Al MAS spectrum

4.4.3 Calcined and Rehydrated $AlPO_4$ – 18

The change in ^{31}P MAS and ^{27}Al MAS spectra brought about by rehydration of the calcined and dehydrated $AlPO_4$-18 is shown in Figure-16. On rehydration of the calcined sample, signal multiplicity in ^{31}P MAS (Figure 16a) and isotropic ^{27}Al spectra (Figure 16c) is considerably enhanced as noticed in the case of rehydrated $AlPO_4$ – 14. The ^{31}P MAS spectrum could be deconvoluted using a minimum of six isotropic resonances of nearly equal intensity in the spectral region -18 and -31 ppm. The ^{27}Al MAS spectrum shows three resonances, two in the tetrahedral region and an intense signal flanked by a quadrupolar line shape near the octahedral region. The ^{27}Al 3Q-MAS spectrum is shown in Figure-17 and the ^{27}Al isotropic spectrum, obtained after a shearing of the 3Q-MAS data, is compared with the MAS spectrum in Figure-16. The 3Q-MAS projection shows at least three resonances in the tetrahedral region and two overlapping resonances in the octahedral region. A closer look at the 3QMAS contours in the octahedral region shows another weak resonance, giving a total of three octahedral resonances. A significant observation is the absence of penta-coordinated aluminum and the emergence of octahedral aluminum environment exhibiting a two-fold signal multiplicity. The low signal intensity for some of the aluminum isotropic signals is attributable to the poor 3Q excitation efficiency due to larger quadrupolar interactions.

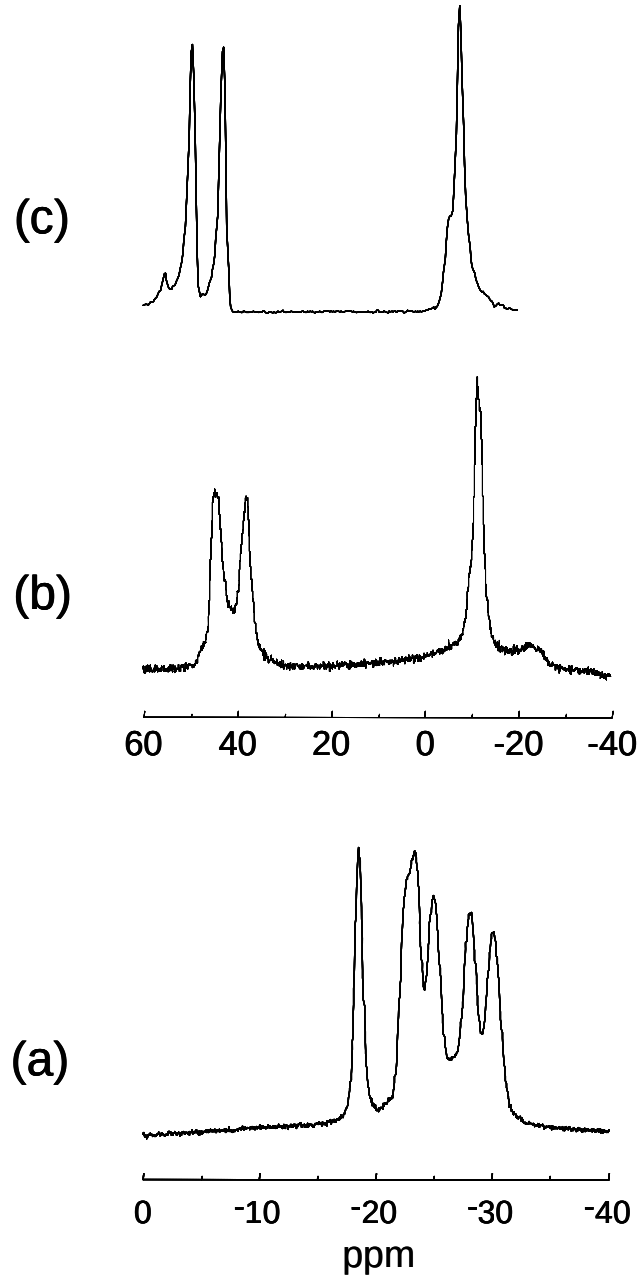

Figure – 16: ^{31}P MAS (**a**), ^{27}Al MAS (**b**) and the isotropic spectrum from ^{27}Al 3QMAS (**c**) of calcined and rehydrated $AlPO_4$ – 18, displaying the crystallographic nonequivalent tetrahedral phosphorus sites aluminum sites in 4 and 6 coordinations.

The structure of the calcined and rehydrated $AlPO_4$ – 18 is unknown. Similar to other aluminophosphate molecular sieves such as VPI-5, the distinct changes that we have observed in NMR spectra are due to the structural distortions brought upon by the adsorption of water molecules leading to formation of octahedral or 6-coordinated aluminum in the framework. As in the case of rehydrated $AlPO_4$ – 14, the ^{31}P and ^{27}Al results suggest that the structural transformation presumably lowers the space group symmetry and the crystal structure would require at least six independent phosphorus

and six aluminum sites with crystallographically inequivalence. A full characterization of the phosphorus and aluminum sites is provide by the ^{31}P isotropic chemical shifts and the ^{27}Al quadrupole interaction parameters and these are given in Table 6.

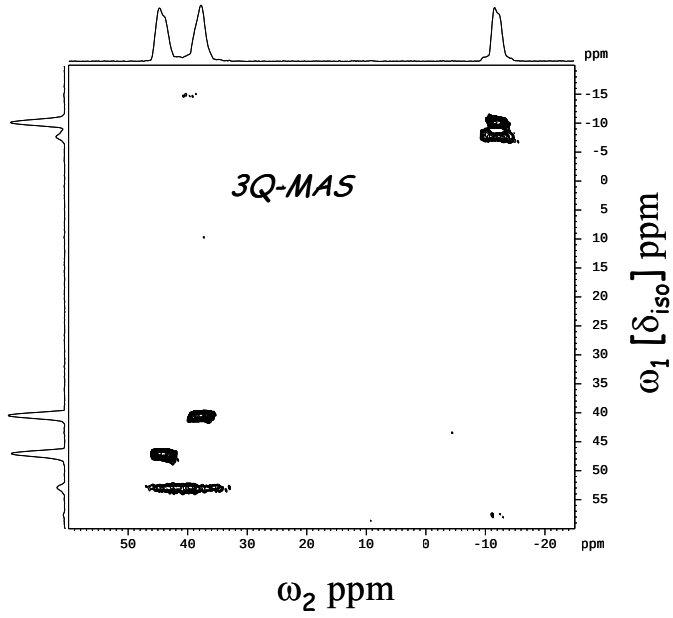

Figure – 17: 2D contour plot of ^{27}Al triple quantum MAS NMR experiment (^{1}H decoupled) of calcined and rehydrated $AlPO_4$-18. The ω_2 projection depicts the CT MAS spectral line shapes, while ω_1 projection yields the corresponding isotropic spectra, depicting the resolution of the crystallographic non-equivalent Al^{IV} and Al^{VI} sites

Table – 6

^{31}P MAS, ^{27}Al MAS and 3QMAS NMR parameters of in-equivalent sites for Calcined and Rehydrated $AlPO_4$-18.

^{31}P MAS	**^{27}Al MAS/3QMAS**				
δ_{iso}	δ_{iso}[1]	P_Q[1]	$\delta_{iso}(MAS)$[2]	$C_Q(MAS)$[2]	$\eta(MAS)$[2]
-30.2	45.2	2.3	45.84	2.07	0.41
-28.1	38.4	2.1	39.29	1.95	0.60
-25.2	48.1	4.6	48.19	4.20	1.00
-23.8	-10.0	2.0	-10.74	1.85	0.37
-22.5	-9.3	3.5	-9.29	3.22	0.66
-18.9	-	-	-9.37	5.57	0.79

[1]From 3QMAS spectrum
[2]Obtained by simulation and fitting of the ^{27}Al MAS spectrum

4.5 Conclusions

In conclusion, we have shown in this chapter that the experimental determination of the ^{31}P and ^{27}Al isotropic chemical shielding and the ^{27}Al electric field gradient parameters, and theoretical calculations of the ^{27}Al quadrupolar interaction parameters, serve as structural aids in solid state NMR. A solid state MAS/3QMAS NMR study, along with *ab initio* calculations of the chemical shielding and EFG tensors, is shown to provide the first opportunity to structurally characterize the aluminophosphate molecular sieves which are catalytically important materials exhibiting structural transformation upon calcinations and rehydration. The structural characterization of two well-known aluminophosphate molecular sieves, $AlPO_4$-14 and $AlPO_4$-18, and the structural transformations occurring in them, have been made through identification, quantification and unambiguous assignment of the structure building phosphorus and aluminum environments, the former existing in tetrahedral and the latter in four, five and six-fold coordination, by a combination of ^{31}P MAS and ^{27}Al 3Q-MAS experiments, 1D MAS spectral simulations and *ab initio* quantum chemical calculations. The experimental and theoretical approaches presented are general and applicable for the elucidation of structural transformations occurring in a wide variety of other class of materials.

6. References:

1. T. Inui, S. Phatanasri and H. Matsuda, J. Chem. Soc., Chem. Commun., 1990, 205.
2. J. Chen and J.M. Thomas, J. Chem. Soc., Chem. Commun., 1994, 603.
3. J.M. Thomas, R. Raja, G. Sankar and R.G. Bell, Nature 398 (1999) 227.
4. T. Wilson, B.M. Lok and E.M. Flanigen, US Patent No. 4310440 (1982).
5. McCusker, L. B.; Birlocher, Ch.; Jahn, E.; Bulow, M. Zeolites 1991, 11, 308
6. Parise, J. B. Inorg. Chem. 1985,24, 4312.
7. Pluth, J. J.; Smith, J. V. Acta Crystallogr. 1986, CIZ, 283.
8. Simmen, A.; McCusker, L. B.; Barlocher, C.; Meier, W. M. Zeolites, 1991, 11, 654.
9. L. Frydman and J. S. Harwood, J. Am. Chem. Soc. 117, 5367 (1995).

10. Heyong, He and J. Klinowski J. Phys. Chem. 97 (1993) 10385.
11. C. Fernandez, J. P. Amoureux, J. M. Chezeau, L. Delmotte and H. Kessler Microporus Materials 6 (1996) 331.
12. Samoson, A.; Lippmaa, E. Phys. Rev. B, 1983, 28, 6567.
13. Amoureux,J. P.; Fernandez, C.; Steuernagel, S. *J. Magn. Reson. A,* 1996, *123*, 116.
14. Bennet A. E.; Rienstra C. M.; Auger M.; Lakshmi K. V.; Griffin R. G. *J. Chem. Phys.* 1995, *103*, 6951.
15. States, D.; Haberkorn, R.; Ruben, D. J. Magn. Resonance 1982, 48, 286-292.
16. D. Massiot, F. Fayon, M. Capron, I. King, S. Le Calvé, B. Alonso, J-O. Durand, B. Bujoli, Z. Gan, G. Hoatson. Magnetic Resonance in Chemistry 40 *70-76* (2002)
17. Gaussian 98, Revision A.9, M. J. Frisch, G. W. Trucks, H. B. Schlegel, G. E. Scuseria, M. A. Robb, J. R. Cheeseman, V. G. Zakrzewski, J. A. Montgomery, Jr., R. E. Stratmann, J. C. Burant, S. Dapprich, J. M. Millam, A. D. Daniels, K. N. Kudin, M. C. Strain, O. Farkas, J. Tomasi, V. Barone, M. Cossi, R. Cammi, B. Mennucci, C. Pomelli, C. Adamo, S. Clifford, J. Ochterski, G. A. Petersson, P. Y. Ayala, Q. Cui, K. Morokuma, D. K. Malick, A. D. Rabuck, K. Raghavachari, J. B. Foresman, J. Cioslowski, J. V. Ortiz, A. G. Baboul, B. B. Stefanov, G. Liu, A. Liashenko, P. Piskorz, I. Komaromi, R. Gomperts, R. L. Martin, D. J. Fox, T. Keith, M. A. Al-Laham, C. Y. Peng, A. Nanayakkara, M. Challacombe, P. M. W. Gill, B. Johnson, W. Chen, M. W. Wong, J. L. Andres, C. Gonzalez, M. Head-Gordon, E. S. Replogle, and J. A. Pople, Gaussian, Inc., Pittsburgh PA, 1998.
18. Vladimir Kellö, Andrzej J. Sadlej, Pekka Pyykkö, Dage Sundholm and Maria Tokman,; *Chem. Phys. Lett.,*1999, *304*, 414.
19. Broach, R.W., Wilson, S.T. and Kirchner, R.M. Proc. 12th Int. Zeolite Conf., III, pp. 1715-1722 (1999)
20. G. Engelhardt and D. Michel, "High resolution solid state NMR of silicates and Zeolites", John Willey & Sons, 1987.
21. Medek, A.; Harwood J.S.; Frydman L. J. Am. Chem. Soc. 1995, 117, 12779-12787.

22. Muller, D; Jahn, E; Ladwig, G; Haubenreisser, U; Chem. Phys. Lett., 1984, 109, 332.